


2017

Precise control over morphology and density of metal and transition metal nanostructures for sensing and energy related applications

Minh Hoang Tran
Iowa State University

Follow this and additional works at: <https://lib.dr.iastate.edu/etd>

 Part of the [Materials Science and Engineering Commons](#), [Mechanics of Materials Commons](#), and the [Nanoscience and Nanotechnology Commons](#)

Recommended Citation

Tran, Minh Hoang, "Precise control over morphology and density of metal and transition metal nanostructures for sensing and energy related applications" (2017). *Graduate Theses and Dissertations*. 16229.
<https://lib.dr.iastate.edu/etd/16229>

This Dissertation is brought to you for free and open access by the Iowa State University Capstones, Theses and Dissertations at Iowa State University Digital Repository. It has been accepted for inclusion in Graduate Theses and Dissertations by an authorized administrator of Iowa State University Digital Repository. For more information, please contact digirep@iastate.edu.

Precise control over morphology and density of metal and transition metal nanostructures for sensing and energy related applications

by

Minh Tran

A dissertation submitted to the graduate faculty

in partial fulfillment of the requirements for the degree of

DOCTOR OF PHILOSOPHY

Major: Mechanical Engineering

Program of Study Committee:
Sonal Padalkar, Major Professor
Baskar Ganapathysubramanian
Nicole Hashemi
Meng Lu
Martin Thuo

The student author, whose presentation of the scholarship herein was approved by the program of study committee, is solely responsible for the content of this dissertation. The Graduate College will ensure this dissertation is globally accessible and will not permit alterations after a degree is conferred.

Iowa State University

Ames, Iowa

2017

Copyright © Minh Tran, 2017. All rights reserved.

TABLE OF CONTENTS

	Page
ACKNOWLEDGMENTS	iv
LIST OF FIGURES	v
LIST OF TABLES	xi
ABSTRACT	xii
CHAPTER 1. INTRODUCTION.....	1
CHAPTER 2. EFFECT OF CITRATE RATIO AND TEMPERATURE ON GOLD NANOPARTICLE SIZE AND MORPHOLOGY	3
Abstract.....	3
Introduction.....	3
Experimental Details	6
Results and Discussions.....	7
Conclusion	19
References.....	20
Appendix.....	27
CHAPTER 3. FORMATION OF SIZE AND DENSITY CONTROLLED NANOSTRUCTURES BY GALVANIC DISPLACEMENT.....	29
Abstract.....	29
Introduction.....	30
Experimental Details	32
Results and Discussion	35
Conclusion	54
References.....	55
Appendix.....	66
CHAPTER 4. EXPLORING THE EFFICACY OF PLATINUM AND PALLADIUM NANOSTRUCTURES FOR ORGANIC MOLECULE DETECTION VIA RAMAN SPECTROSCOPY	69
Abstract.....	69
Introduction.....	70
Experimental Details	73
Results and Discussions.....	76
Conclusion	85
References.....	85
Appendix.....	95

CHAPTER 5. PREPARATION AND CHARACTERIZATION OF COBALT AND NICKEL NANOSTRUCTURES ON SILICON SUBSTRATES FOR HYDROGEN GENERATION	97
Abstract	97
Introduction	97
Experimental Details	99
Results and Discussion	101
Conclusion	103
References	103
CHAPTER 6. ELECTRODEPOSITION OF GOLD NANOSTRUCTURES HAVING CONTROL MORPHOLOGY	108
Abstract	108
Introduction	108
Experimental Details	111
Results and Discussions	112
Influence of the applied potential on Au nanostructure morphology	113
Influence of pH variation on the Au nanostructure morphology	115
Influence of L-cysteine on the Au nanostructure morphology	117
Conclusion	122
CHAPTER 7. UTILIZATION OF INEXPENSIVE CARBON-BASED SUBSTRATES AS A PLATFORM FOR SENSING	127
Abstract	127
Introduction	128
Experimental Details	130
Results and Discussions	132
Conclusion	140
References	141
CHAPTER 8. CONCLUSION	148
References	149

ACKNOWLEDGMENTS

I would like to thank my committee chair, Dr. Sonal Padalkar, and my committee members, Dr. Baskar Ganapathysubramanian, Dr. Nicole Hashemi, Dr. Meng Lu, and Dr. Martin Thuo, for their guidance, support, feedback, and generosity throughout the course of my study.

In addition, I would also like to thank my friends, colleagues, the department faculty and staff for making my time at Iowa State University a wonderful experience. I want to also offer my great gratitude to my parents back in Vietnam and my sister who were always my source of encouragement, advice, and comfort, without whom, I would not be able to pursue a degree in the US.

LIST OF FIGURES

	Page
Figure 2.1 Absorption wavelength as a function of the Na ₃ Ct/HAuCl ₄ ratios.....	8
Figure 2.2 Images of the reaction mixture changing color, due to the addition of citrate solution, from (a) colorless, (b) gray, (c) purple to (d) red.....	9
Figure 2.3 Absorption peak as a function of temperature for four Na ₃ Ct / HAuCl ₄ ratios.....	10
Figure 2.4 Full width at half maximum (FWHM) as a function of temperature for four Na ₃ Ct / HAuCl ₄ ratios.....	11
Figure 2.5 TEM images of Au NPs synthesized using Na ₃ Ct/HAuCl ₄ ratio of 1.50:1 (a-c) and 4.33:1 (d-f) at temperatures of 60 °C (a, d), 80 °C (b, e) and 100 °C (c, f). The highlighted NPs are faceted. The scale bar for all TEM images is 50 nm.	12
Figure 2.6 Indexed SAED pattern, of Au NPs synthesized at 80°C and a Na ₃ Ct/HAuCl ₄ ratio of 4.33, indicates face-centered cubic structure of Au.....	13
Figure 2.7 Evolution of UV-Vis absorption maxima as a function of reaction time (a) for Na ₃ Ct/HAuCl ₄ ratio of 1.5 and (b) 4.33.	14
Figure 2.8 A logarithmic plot of reaction time as a function of synthesis temperature for low and high concentration regimes	17
Figure 3.1 Experimental steps of the synthesis process. (a) Cleaved and cleaned Si substrate. (b) Immersion in 10% HF for 2 min, to dissolve the surface oxide. (c) Immersion in 0.3 mM metal precursor solution for 5 min. (d) Rinse sample with deionized water.	34
Figure 3.2 SEM images of Au nanostructures deposited on Si substrate after (a) first, (b) second, (c) third, (d) fourth and (e) fifth, (f) sixth, (g) eighth, and (h) tenth deposition cycle. The scale bar is 500 nm.	36
Figure 3.3 SEM images of Cu-based nanostructures deposited on Si substrate after (a) first, (b) second, (c) third, (d) fourth and (e) fifth deposition cycle. The scale bar is 500 nm.....	37

Figure 3.4	SEM images of Au nanostructures deposited on Si substrate after (a) first, (b) second, (c) third, (d) fourth and (e) fifth, (f) sixth, (g) eighth, and (h) tenth deposition cycle with L-Cys added as surfactant. The scale bar is 500 nm.....	39
Figure 3.5	SEM images of Au nanostructures deposited on Si substrate after (a) first, (b) second, (c) third, (d) fourth and (e) fifth, (f) sixth, (g) eighth, and (h) tenth deposition cycle with CTAB added as surfactant. The scale bar is 500 nm.....	40
Figure 3.6	SEM images of Cu-based nanostructures deposited on Si substrate after (a) first, (b) second, (c) third, (d) fourth and (e) fifth deposition cycle with L-Cys added as surfactant. The scale bar is 500 nm.....	40
Figure 3.7	SEM images of Cu-based nanostructures deposited on Si substrate after (a) first, (b) second, (c) third, (d) fourth and (e) fifth deposition cycle with CTAB added as surfactant. The scale bar is 500 nm	41
Figure 3.8	SEM images of Au nanostructures deposited on Si substrate after sequential exposure to (a) L-Cys then H _{AuCl} ₄ , (b) L-Cys then mixture of H _{AuCl} ₄ and L-Cys, (c) CTAB then H _{AuCl} ₄ , and (d) CTAB then mixture of H _{AuCl} ₄ and CTAB. The scale bar is 500 nm.....	43
Figure 3.9	Representative AFM topography maps of the Au samples after one (1X), three (3X), and five (5X) deposition cycles. Scan size of 2 μm x 2 μm. Height scale is in nm.	45
Figure 3.10	Absorption spectra of Au nanoparticles are the first deposition cycle in the absence and presence of surfactants.....	46
Figure 3.11	RMS roughness of Au samples after one (1X), three (3X), and five (5X) deposition cycles. Mean values from five different locations on each sample are shown. Error bars represent 95% confidence intervals.	46
Figure 3.12	XPS spectra showing (a) Cu 2p peaks corresponding to different oxidation states of Cu, (b) O 1s peaks corresponding to different oxide species, and (c) C 1s peaks corresponding to various carbon bonds (d) AES spectrum showing Cu LMM peak resembling that of Cu(OH) ₂ and Cu ₂ O. The dashed curves in (a) and (b) represent fitted Gaussian curves	48
Figure 3.13	Raman spectra of R6G adsorbed on bare Si, and Si deposited with Au nanostructures after five, eight, and ten deposition cycles. The R6G concentration was 10 ⁻⁵ M.	51

Figure 3.14	Raman spectra of R6G adsorbed on bare Si, and Si deposited with Au and Cu nanostructures after ten deposition cycles. The R6G concentrations were 10^{-4} M for bare Si and Cu/Si, and 10^{-5} M for Au/Si.	52
Figure 3.15	Raman spectra of R6G at two different concentrations drop cast onto Si deposited with Au nanostructures after five deposition cycles.	52
Figure 3.16	Raman spectrum of 10^{-2} M paraoxon adsorbed on Au nanostructures deposited on Si substrate after ten deposition cycles. Raman spectrum of paraoxon adsorbed on bare Si substrate is shown for comparison.	53
Figure 4.1	(a) Cleaved Si substrate. (b) Clean Si substrate with acetone, ethanol, and DI water in an ultrasonic bath. (c) Immersion in 10% (w/w) HF solution. (d) Immersion of Si substrate in 0.3 mM metallic precursor solution. (e) Rinse sample with DI water (f) Store dry sample.	75
Figure 4.2	SEM images of Pd nanostructures deposited on Si substrate after (a) first, (b) third, (c) fifth, (d) eighth, and (e) tenth deposition cycle. The scale bar is 500 nm.	76
Figure 4.3	SEM images of Pt nanostructures deposited on Si substrate after (a) first, (b) third, (c) fifth, (d) eighth, and (e) tenth deposition cycle. The scale bar is 500 nm.	77
Figure 4.4	SEM images of Pd nanostructures deposited on Si substrate after (a) first, (b) tenth deposition cycle with SDS surfactant added, and (c) first, (d) tenth deposition cycle with CTAB surfactant added. The scale bar is 500 nm.	78
Figure 4.5	SEM images of Pt nanostructures deposited on Si substrate after (a) first, (b) tenth deposition cycle with SDS surfactant added, and (c) first, (d) tenth deposition cycle with CTAB surfactant added. The scale bar is 500 nm.	80
Figure 4.6	EDX patterns of (a) Pd and (b) Pt nanostructures deposited on Si substrates after five deposition cycles showing the presence of Pd and Pt, respectively. EDX patterns recorded from individual nanostructures are presented as spots 1, 2, and 3.	80
Figure 4.7	Normalized UV-Vis spectra of Pt and Pd nanostructures deposited on Si substrates after five deposition cycles, showing characteristic peaks and increasing absorption toward shorter wavelengths. The spectrum of Pt nanostructures was shifted downward for clarity.	81

Figure 4.8	Raman spectra of (a) 10 ⁻⁵ M R6G and (b) 10 ⁻² M paraoxon adsorbed on Pd and Pt nanostructures deposited on Si substrates after ten deposition cycles. Raman spectra of R6G and paraoxon adsorbed on bare Si substrates are shown for comparison. The (*) indicates Raman mode of Si	83
Figure 5.1	SEM images showing the morphology and density of Ni nanostructures deposited on Si substrate by galvanic displacement after multiple deposition cycles (1x - 10x), after being annealed at 100oC for 30 minutes, and after the use of additives. The EDX spectrum showing the elemental composition of the sample surface.	101
Figure 5.2	SEM images showing the morphology and density of Co nanostructures deposited on Si substrate by galvanic displacement after multiple deposition cycles (1x - 10x), after being annealed at 100oC for 30 minutes, and after the use of additives. The EDX spectrum showing the elemental composition of the sample surface.	102
Figure 5.3	Normalized UV-Vis spectra of Ni and Co showing characteristic peaks and increasing absorption toward shorter wavelengths	103
Figure 6.1	Photographs of an (a) electrodeposition setup, consisting of a (b) working, (c) reference, and (d) counter electrode.....	112
Figure 6.2	SEM images of Au nanostructures electrodeposited, with a pH of 3, at -0.4 V (a), -0.6 V (b) and -0.8 V (c). The scale bar is 1 μm.....	114
Figure 6.3	SEM images of Au nanostructures electrodeposited, with a pH of 8, at -0.4 V (a), -0.6 V (b) and -0.8 V (c). The scale bar is 1 μm.....	115
Figure 6.4	SEM images of Au nanostructures electrodeposited using 0.1 mM L-cysteine at varying potentials of -0.4 V, -0.6 V and -0.8 V at pH 3 (a-c) and at pH 8 (d-f). The scale bar is 1 μm.....	118
Figure 6.5	SEM images of Au nanostructures electrodeposited using 0.3 mM L-cysteine at varying potentials of -0.4 V, -0.6 V and -0.8 V at pH 3 (a-c) and at pH 8 (d-f). The scale bar is 1 μm.....	119
Figure 6.6	XRD plots of Au nanostructures fabricated at an applied potential of -0.8 V, with varying pH and L-cysteine concentrations.....	121
Figure 7.1	Photographs of the experimental setup (a), and individual electrodes, including reference (b), counter (c), and working (d) electrodes.	131

Figure 7.2	Photographs showing carbon cloth (a) and carbon paper (b) after electrodeposition with Au nanostructures.	132
Figure 7.3	SEM images of carbon cloth (a) before and (b) after electrodeposition of Au nanostructures. The inset shows Au-electrodeposited carbon cloth at higher magnification.	133
Figure 7.4	SEM images of carbon paper (a) before and (b) after electrodeposition of Au nanostructures. The inset shows Au-electrodeposited carbon paper at higher magnification.	133
Figure 7.5	EDX patterns and mapping analysis of Au nanostructures electrodeposited on (a,b) carbon cloth, and (c,d) carbon paper, respectively. The insets show the different spots where EDX patterns were taken. The scale bars on the insets and the EDX mapping are 550 μm and 100 μm , respectively.	134
Figure 7.6	Normalized UV-Vis spectra of Au electrodeposited carbon cloth and carbon paper	136
Figure 7.7	Raman spectra of (a) 10^{-5} M and 10^{-6} M R6G, and (b) 10^{-2} M paraoxon adsorbed on Au nanostructures electrodeposited on carbon cloth and carbon paper, respectively. Raman spectra of R6G and paraoxon adsorbed on blank carbon cloth and paper without Au coating are shown for comparison. The inset shows a close-up view for carbon cloth.	137
Figure 7.8	Wiping the contaminated area on an apple's skin by carbon cloth electrodeposited with Au for SERS detection of paraoxon.	139
Figure 7.9	SERS detection of paraoxon on apple using carbon cloth and paper electrodeposited with Au as substrates. The results show that the substrates were sensitive to the presence of paraoxon.	140
Figure A 2.1	Absorption peak as a function of temperature for three $\text{Na}_3\text{Ct}/\text{HAuCl}_4$ ratios, showing a small decrease in absorption maxima with increasing temperature	27
Figure A 2.2	Full width at half maxima (FWHM) as a function of temperature for three $\text{Na}_3\text{Ct}/\text{HAuCl}_4$ ratios, show a slight decrease in FWHM with increasing temperature	28

Figure A 2.3 Mechanism of NP shape evolution in high and low concentration regime.....	28
Figure A 3.1 The number densities of Au and Cu-based nanoparticles with and without surfactant after one deposition cycle.	66
Figure A 3.2 Size distribution with Gaussian curve fitting of Au nanoparticles (a) without surfactant, (b) with L-cysteine, and (c) with CTAB, and Cu-based nanoparticles (d) without surfactant, (e) with L-cysteine, and (f) with CTAB after one deposition cycle. The distribution was constructed based on (a) 2941, (b) 2174, (c) 1968, (d) 742, (e) 1823, and (f) 563 particles.	66
Figure A 3.3 UV-Vis spectra of Au samples without surfactants (a), with L-Cys (b) and with CTAB (c). The first deposition cycle is 1X and the fifth deposition cycle is 5X.	67
Figure A 3.4 XRD pattern of Au (a) and Cu (b) nanostructures on Si substrate. The patterns suggest an FCC structure of Au and Cu.....	68
Figure A 4.1 SEM images of Pd nanostructures deposited on Si substrate after (a) first, (b) third, (c) fifth, (d) eighth, and (e) tenth deposition cycle. The scale bar is 2 μm . (f-j) Size distributions of the corresponding Pd nanostructures.	95
Figure A 4.2 SEM images of Pt nanostructures deposited on Si substrate after (a) first, (b) third, (c) fifth, (d) eighth, and (e) tenth deposition cycle. The scale bar is 2 μm . (f-j) Size distributions of the corresponding Pt nanostructures.	96
Figure A 4.3 Number densities of (a) Pd and (b) Pt nanostructures after multiple deposition cycles. 1x-10x denote one to ten deposition cycles, respectively.....	96

LIST OF TABLES

	Page
Table 3.1 Average nanoparticle size for Au and Cu-based nanoparticles after first deposition cycle	41
Table 3.2 Raman peak assignments for R6G dye and paraoxon.....	53
Table 4.1 Raman mode assignments for R6G and paraoxon, corresponding to Figure 4.8	83
Table 6.1 The process parameters varied in the present study for the electrodeposition Au nanostructures.....	113
Table 7.1 Mass fraction analysis of chemical elements obtained by EDX	135
Table 7.2 Raman peak assignments for R6G dye and paraoxon pesticide corresponding to Figure 7.7.....	138
Table A 2.1 The pH value of the reaction mixture with varying $\text{Na}_3\text{Cit}/\text{HAuCl}_4$ ratios.....	27
Table A 3.1 SPR peak positions of Au samples in the absence and presence of surfactants, recorded corresponding to each deposition cycle.	67
Table A 4.1 Average sizes of Pd and Pt nanostructures after multiple deposition cycles.....	95

ABSTRACT

Metallic nanostructures are of great interest due to their applicability in various modern technologies, such as catalysis, sensing, and optoelectronics. In this work, we employed three solution-based methods, including colloidal suspension synthesis, modified galvanic displacement, and electrodeposition, to synthesize nanostructured metals and transition metals, including gold (Au), copper (Cu), platinum (Pt), palladium (Pd), nickel (Ni), and cobalt (Co). Our focus was to establish process-structure-property relationship and explore their applicability in the field of sensing and clean energy generation. More precisely we established relationships between experimental parameters, such as temperature, applied potential, electrolyte pH, reactant concentration, additive, and the number of deposition cycles, and the characteristics of the nanostructures, such as morphology, density, size, and size distribution. Our results indicated that the nanostructures were tunable by adjusting the process parameters. This provided insight into the growth mechanisms of the metallic nanostructures. Since properties of the nanostructures are tunable by controlling the structure, our results provided researchers with additional tools to obtain nanomaterials with desired properties for specific applications. The materials synthesized by our methods were utilized to as substrates for surface enhanced Raman spectroscopy (SERS) and as photocathodes for photoelectrochemical production of hydrogen. The results showed that the performances of our materials were either promising or compatible with those reported in the literature, thus bringing new opportunities to the development of low-cost, high-performance, and flexible nanomaterials for the current and future technologies.

CHAPTER 1. INTRODUCTION

Metallic nanostructures have been the subjects of intense scientific research due to their novel optical, chemical, catalytic, and electronic properties, which can be utilized for numerous applications. This work relied on the fundamental understanding that there is a strong correlation between the process and structure of the synthesized materials. Additionally, a strong correlation exists between the structure and property of the materials. In this work, various metals, including gold (Au), copper (Cu), platinum (Pt), palladium (Pd), nickel (Ni), and cobalt (Co) nanostructures, were investigated. These metallic nanostructures were synthesized by three different routes, including (1) colloidal suspension synthesis by citrate reduction, (2) electroless deposition by galvanic displacement on silicon (Si) substrate with limited hydrofluoric acid exposure, and (3) electrodeposition on rigid and flexible substrates. In each of these methods, our focus was to systematically draw the relationship between key experimental parameters, including temperature, applied potential, electrolyte pH, reactant concentration, additives, and the number of deposition cycles, and the morphology, density, size, and size distribution of the resulting metallic nanostructures. Thus, this work not only furthers our understanding of metallic nanostructural growth but also contributes to our capability to obtain nanomaterials with desired structural characteristics and properties by simply adjusting the process parameters. Since the outcome is tunable and reproducible, the synthesized materials with controlled nanostructures can be used for certain target applications.

After the important material synthesis stage, the resulting metallic nanostructures were investigated for their applications in surface-enhanced Raman spectroscopy (SERS) and clean energy generation. With the advent of portable Raman technique, the demand of SERS

substrates has increased. This portable technique has made sensing accessible to remote locations, large populations, and sensing a variety of trace analytes. The conventional SERS substrates are prepared by lithographic techniques, which are costly and complicated. In the present work, SERS substrates were fabricated by modified galvanic displacement and electrodeposition methods. These methods required inexpensive or no instrumentation. In addition, the experimental procedures were simple, thus saving training cost. Furthermore, nanostructures of the SERS substrates fabricated by these methods can be tuned and are uniform and reproducible. In addition to Au and Cu nanostructures whose SERS applications have been widely used, this work also described our experiments on non-SERS materials, including Pd and Pt. Since these noble metals have excellent catalytic properties, one potential application of SERS from Pt and Pd is the probing of catalytic mechanisms occurring on the surface of Pt and Pd catalysts. The present work also demonstrates the effort toward fabricating flexible substrates for SERS. These substrates were carbon cloth and carbon paper whose surfaces were electrodeposited with Au. Another application in which these materials showed promises was the production of clean energy. Thus, the present work demonstrates the ability to fabricate inexpensive, reproducible, effective, and tunable nanomaterials by simple and easy routes, which advances the realization of the large-scale use of nanostructured materials for current and future technologies.

CHAPTER 2. EFFECT OF CITRATE RATIO AND TEMPERATURE ON GOLD NANOPARTICLE SIZE AND MORPHOLOGY

Minh Tran¹, Rebekah DePenning², Madeline Turner¹ and Sonal Padalkar^{1,3} *

1. Department of Mechanical Engineering, Iowa State University, Ames, IA 50011, USA

2. Department of Engineering, Dordt College, Sioux Center, IA 51250, USA

3. Microelectronics Research Center, Iowa State University, Ames, IA 50011, USA

* Email: padalkar@iastate.edu

Abstract

Gold nanoparticles (Au NPs) were synthesized by the citrate reduction method. The evolution of NP size and morphology was closely studied by varying temperature and citrate to gold precursor ($\text{Na}_3\text{Ct}/\text{HAuCl}_4$) ratios. The reaction temperatures below 100 °C were mainly studied. A $\text{Na}_3\text{Ct}/\text{HAuCl}_4$ ratio range of 1.25:1 to 4.33:1 was the focus of our investigation. The NP size and morphology was strongly influenced by the $\text{Na}_3\text{Ct}/\text{HAuCl}_4$ ratio, while the temperature played a subtle role. The reaction times were also monitored. The higher concentration samples required almost an order of magnitude longer reaction time compared to the low concentration samples.

Introduction

In recent decade significant progress has been made in the field of nanoscience and nanotechnology. The area of metallic nanostructure fabrication has explored many synthesis and deposition routes leading to the formation of a range of nanostructure morphologies and sizes. Gold nanoparticle (Au NP) synthesis has gained much attention due to their unique optoelectronic properties. These Au NPs can be used in a variety of potential applications like solar cells [1], catalysts [2], biosensors [3] and biomarkers in early disease detection [4].

Due to the high demand of Au NPs, many synthesis approaches have been studied. Au NPs have been prepared by using gas phase precursors [5, 6] and also by sintering of Au thin films [7]. The use of proteins and biopolymer templates for the synthesis of Au NPs has yielded promising results [8, 9]. Further, the utilization of plant extracts has demonstrated the successful synthesis of Au NPs [10]. There are a large number of solution based routes used primarily due to the ability to control NP size and morphology. These routes offer advantages like simplicity, scalability and low-cost production [11, 12]. Among the solution based synthesis sodium citrate (Na_3Ct) reduction method pioneered by Turkevich, in which the gold precursor (HAuCl_4) is reduced by Na_3Ct , is widely used due to advantages mentioned above [12-15]. Further, the citrate method can obtain a wide range of Au NP sizes and shapes that can be used for a variety of potential applications [16]. Since the first report on the citrate reduction there have been many publications focusing on several different aspects of this synthesis method [16-19]. Frens demonstrated a variation in Au NP size by changing the $\text{Na}_3\text{Ct}/\text{HAuCl}_4$ ratio from 0.4:1 to 2.6:1 [16]. It was noticed that the least citrate concentration led to the largest Au NP size [16, 20]. Modeling studies on the formation of Au NPs by the citrate reduction method was performed by Kumar and co-workers, which described the formation mechanism of the Au NPs with varying $\text{Na}_3\text{Ct}/\text{HAuCl}_4$ ratios. From their model, the Au NP size decreases exponentially from 130 nm to 30 nm for a $\text{Na}_3\text{Ct}/\text{HAuCl}_4$ ratio of 0.4: 1 to 2.0:1. The model established a relationship between the Au NP size and $\text{Na}_3\text{Ct}/\text{HAuCl}_4$ ratios, which agreed with the findings of Frens and Turkevich [12, 13, 16, 21]. Peng and co-workers studied a range of the $\text{Na}_3\text{Ct}/\text{HAuCl}_4$ ratio from 0.7:1 to 30:1. The report demonstrated that with increasing $\text{Na}_3\text{Ct}/\text{HAuCl}_4$ ratios from 0.7:1 to 3.5:1, the number of nuclei increased and the final Au NP size decreased. Beyond the

$\text{Na}_3\text{Ct}/\text{HAuCl}_4$ ratio of 3.5:1 there was an increase in the Au NP size, attaining a constant size of ~30 nm [21].

To provide explanation for the dependence of Au NP size and reaction kinetics on citrate concentration several theoretical and complimentary experimental work has been done. For example, Zukoski and co-workers described the Au NP synthesis, in the $\text{Na}_3\text{Ct}/\text{HAuCl}_4$ ratio range of 1:1 to 7:1, as an initial formation of unstable large aggregates. These large aggregates have a fluffy morphology and are composed of several spherical Au clusters that later form monodispersed stable Au NPs [21, 22]. In contrast, Peng's work described the aggregates as having a wire like morphology composed of Au crystals for $\text{Na}_3\text{Ct}/\text{HAuCl}_4$ ratio below 3.5:1. For $\text{Na}_3\text{Ct}/\text{HAuCl}_4$ ratio greater than 3.5:1, Peng et al demonstrated that the traditional nucleation-growth model was applicable [21]. Peng et al also emphasized that the pH value of citrate solution played an important role in influencing the structure and reactivity of reactants. This led to variations in NP size, size distribution, shape, and nucleation rate. Other reports on pH variation indicated a strong influence on NP size and size distribution [23, 24].

Another experimental parameter, the temperature was also explored. Rohiman et al. explored the effects of increasing temperatures above 100 °C and observed decreasing NP size with increasing temperatures [15]. Recently, a report on the effects of latent heat in boiling water on the synthesis of Au NPs was studied. It was shown that there is a small but noticeable decrease in the NP size due to the latent heat of boiling water. It was concluded that this latent heat could be responsible for the variation of Au NP sizes synthesized by various researchers in this field [25]. Other parameters like stirring speeds and sonication

effects on Au NP synthesis were also studied and demonstrated little or no effect on the Au NP size and shape [26, 27].

From several reports in the literature, it is clear that the $\text{Na}_3\text{Ct}/\text{HAuCl}_4$ ratio and temperature are defining parameters in the synthesis of Au NPs. Further there is also a general consensus in the scientific community regarding the influence of $\text{Na}_3\text{Ct}/\text{HAuCl}_4$ ratio and temperature on the Au NP size, size distribution and morphology. However, a systematic study on the variation of the two parameters has not been explored. Moreover, among the two parameters which one is more influential on the evolution of Au NP size, size distribution and morphology has also not been studied.

Hence, the primary objective of this work was to systematically study the influence of $\text{Na}_3\text{Ct}/\text{HAuCl}_4$ ratio and temperature variations on the Au NP size, size distribution, morphology, and reaction kinetics. We performed Au NP synthesis at $\text{Na}_3\text{Ct}/\text{HAuCl}_4$ ratios ranging from 0.25:1 to 15:1, thus covering a large range of ratios. The NP synthesis was conducted in the temperature range of 50°C to 100°C, since this temperature range will help elucidate the influence of temperature on the Au NP synthesis.

Experimental Details

The chemicals used for the Au NP synthesis were gold (III) chloride trihydrate ($\text{HAuCl}_4 \cdot 3\text{H}_2\text{O}$, $\geq 99.9\%$), and sodium citrate dihydrate ($\text{Na}_3\text{C}_6\text{H}_5\text{O}_7 \cdot 2\text{H}_2\text{O}$, $\geq 99.0\%$). These chemicals were purchased from Sigma-Aldrich (Milwaukee, WI, USA) and used as received. All solutions were prepared using deionized water. The Au NPs were synthesized using the citrate reduction method [16]. Briefly, to a 50 mL Erlenmeyer flask, 2.5 mg $\text{HAuCl}_4 \cdot 3\text{H}_2\text{O}$ powder was dissolved in 25 mL deionized water to obtain 10^{-2} % (w/w) HAuCl_4 solution. The $\text{Na}_3\text{C}_6\text{H}_5\text{O}_7 \cdot 2\text{H}_2\text{O}$ was dissolved in deionized water to obtain a citrate solution of concentrations ranging from 0.44% - 1.53% (w/w).

The Au NP synthesis was performed by heating HAuCl_4 solution to the desired temperature on a hot plate with continuous stirring, followed by the addition of the citrate solution. The stirring speed was kept at 500 rpm, which was optimal for producing monodispersed Au NPs [28]. Upon the addition of citrate solution, the final solution mixture undergoes a color change from colorless, gray, purple and then red. To ensure the reaction has reached completion, the solution mixture was maintained on the hot plate at the desired temperature for 30 minutes after the solution had turned red. The reaction flask was then removed from the hot plate and the final solution mixture was air cooled to room temperature. Some amount of the final solution mixture was used for characterization while the remaining was stored at 4°C .

A pH value of the reaction mixtures was measured after the addition of citrate solution to the HAuCl_4 solution by utilizing a pH 700 benchtop meter. UV-Vis absorption spectroscopy of Au NPs was recorded by a Perkin Elmer Lambda 25 spectrophotometer. During the Au NP synthesis, the UV-Vis absorption as a function of time was recorded by extracting aliquots from the reaction mixture. The morphology and crystal structure of Au NPs were studied by transmission electron microscopy (TEM) and selected area electron diffraction (SAED), respectively. A JEOL 2100 electron microscope with 200 kV accelerating voltage was used for this purpose. The TEM samples were prepared by drop casting 3 μL of the as-prepared Au NP suspension on a carbon-coated copper grid. The TEM grid was air dried before characterization.

Results and Discussions

The Au NPs were synthesized using $\text{Na}_3\text{Cit}/\text{HAuCl}_4$ ratios ranging from 0.25:1 to 15:1 as mentioned above. UV-Vis measurements of the Au NPs showed a wavelength trend similar to that observed by Turkevick, Kumar and Ferns [12, 13, 16]. An exponential curve

was fitted to the experimental data as shown in Figure 2.1. It was evident from our experimental data that the wavelength or NP size begin to stabilize at the $\text{Na}_3\text{Ct}/\text{HAuCl}_4$ ratio of 2.25:1. This ratio was taken into consideration during our investigation. Thus the remainder of our experiments were focused on a range of $\text{Na}_3\text{Ct}/\text{HAuCl}_4$ ratios between 1.25:1 and 4.33:1 including the above ratio, which indicates the onset of NP size stabilization. Further, the ratios were separated into low and high citrate concentration regimes. The low regime consisted of 1.25:1, 1.5:1 and 1.75:1 $\text{Na}_3\text{Ct}/\text{HAuCl}_4$ ratios. The high regime included 2.25:1, 2.66:1, 3.50:1 and 4.33:1 $\text{Na}_3\text{Ct}/\text{HAuCl}_4$ ratios. The distinction between low and high regimes was made on the basis of noticeable difference in the size and morphology of the synthesized Au NPs. Additionally, literature reports indicate a narrow size distribution for Au NPs with size between 10 and 40 nm, for the $\text{Na}_3\text{Ct}/\text{HAuCl}_4$ ratios between 1.25:1 and 4.33:1 respectively [12, 13, 16, 20-22, 29].

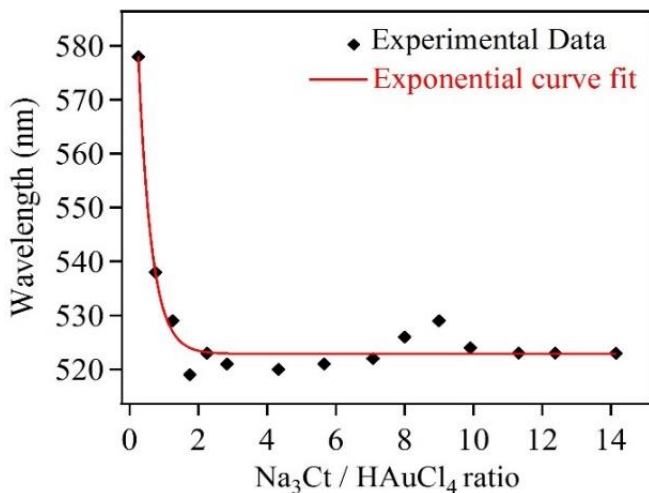


Figure 2.1 *Absorption wavelength as a function of the $\text{Na}_3\text{Ct}/\text{HAuCl}_4$ ratios.*

Along with the study of $\text{Na}_3\text{Ct}/\text{HAuCl}_4$ ratio variation, the temperature for the synthesis was also varied. Since temperature is an important parameter in the citrate reduction method and is generally kept at 100 °C, our study focused on studying the

influence of temperature variations on NP size, morphology and reaction kinetics. The temperature range of interest was between 50 °C and 100 °C. It was noted that Au NP synthesized below 50 °C had a very high degree of polydispersity. Further, the long reaction times at low temperature made the synthesis method unrealistic. Thus the lowest temperature reported in this investigation is 50 °C.

As mentioned above, the reaction mixture undergoes a series of color changes following citrate solution addition (Figure 2.2). The duration of these color changes were recorded, which were related to the reaction kinetics of the Au NP synthesis. These durations were labeled as time t_1 and t_2 , corresponding to nucleation and growth times respectively. During time t_1 the reaction mixture changes from colorless to gray and exhibits no absorption peak. In time t_2 the reaction mixture undergoes color change from gray to red and an absorption peak is observed, which was attributed to the formation of Au NPs [22, 30, 31].

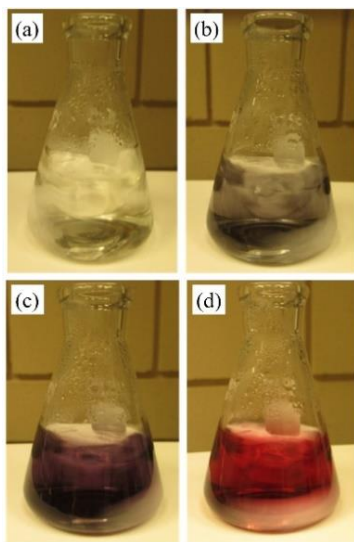


Figure 2.2 *Images of the reaction mixture changing color, due to the addition of citrate solution, from (a) colorless, (b) gray, (c) purple to (d) red.*

For $\text{Na}_3\text{Ct}/\text{HAuCl}_4$ ratios under consideration, the pH of the reaction mixture was also recorded. The pH varied from 4.15 to 5.81, with increasing $\text{Na}_3\text{Ct}/\text{HAuCl}_4$ ratio (See

supporting information, Table A 2.1). It is demonstrated in literature that citrate is alkaline in nature, thus increase in solution pH with increasing $\text{Na}_3\text{Ct}/\text{HAuCl}_4$ ratio was expected [22].

The UV-Vis absorption measurements were performed as a function of synthesis temperature for the $\text{Na}_3\text{Ct}/\text{HAuCl}_4$ ratios under consideration. Figure 2.3 shows the absorption peak as a function of synthesis temperature for $\text{Na}_3\text{Ct}/\text{HAuCl}_4$ ratios belonging to the low and high concentration regimes. The remaining data is presented in the supporting

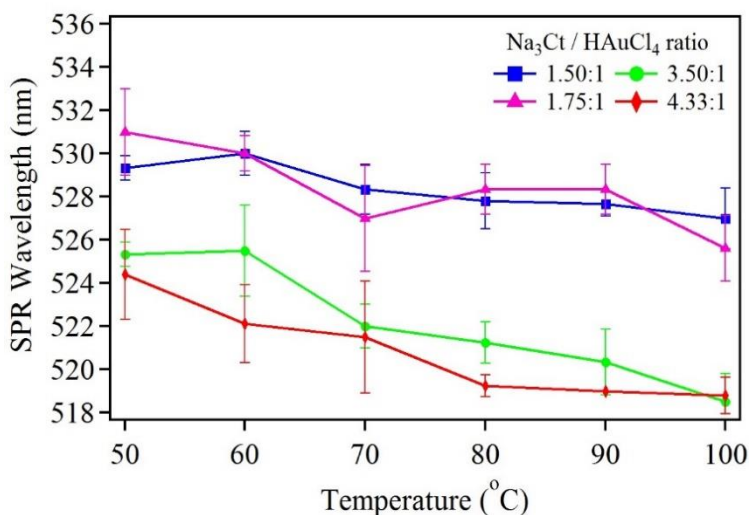


Figure 2.3 Absorption peak as a function of temperature for four $\text{Na}_3\text{Ct} / \text{HAuCl}_4$ ratios (see supporting information Figure A 2.1). From the UV-Vis data, there is a very small decrease in the absorption peak with increase in the synthesis temperature for all $\text{Na}_3\text{Ct}/\text{HAuCl}_4$ ratios. This small decrease in absorption maxima indicates a limited change in the NP size, for a particular $\text{Na}_3\text{Ct}/\text{HAuCl}_4$ ratio. However, there is significant difference in the absorption maxima, at a particular temperature, between the low and high concentration regime samples, which suggests NP size variation occurred for different citrate concentrations. The NP size was calculated by using the absorption maxima and an approximate size of 40 nm and 20 nm was obtained for the low and high regime samples respectively [3, 13, 21, 22, 24, 28, 32-35].

Further, the size distribution was studied by measuring the full width at half maximum (FWHM) of the UV-Vis spectra. From the measurements it was clear that there is a very small decrease in the FWHM with increasing synthesis temperature for each $\text{Na}_3\text{Ct}/\text{HAuCl}_4$ ratio. However, there was a substantial decrease in the FWHM between $\text{Na}_3\text{Ct}/\text{HAuCl}_4$ ratios of low and high regimes. Thus it was inferred that the polydispersity of the Au NPs is not strongly affected by the temperature, but the $\text{Na}_3\text{Ct}/\text{HAuCl}_4$ ratios greatly influenced the polydispersity. The remaining data on FWHM is presented in the supporting information (Figure A 2.2). These results highlight the strong influence of $\text{Na}_3\text{Ct}/\text{HAuCl}_4$ ratios on the NP size and size distribution, while indicating that the synthesis temperature has a subtle influence.

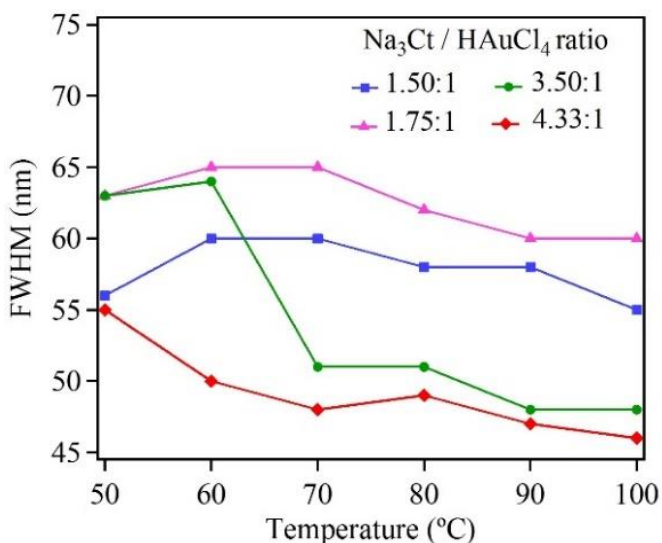


Figure 2.4 Full width at half maximum (FWHM) as a function of temperature for four $\text{Na}_3\text{Ct}/\text{HAuCl}_4$ ratios

In order to support the UV-Vis data, TEM imaging was performed on the Au NPs to study the size, shape and size distribution variation with temperature and $\text{Na}_3\text{Ct}/\text{HAuCl}_4$ ratios. For this study $\text{Na}_3\text{Ct}/\text{HAuCl}_4$ ratios of 1.50:1 and 4.33:1 were chosen as they represented the low and high concentration regimes respectively. The temperatures of 60 °C,

80 °C and 100 °C were selected. The 100 °C sample was used as a reference and all comparisons were made to this sample. For the $\text{Na}_3\text{Ct}/\text{HAuCl}_4$ ratio of 1.50:1, there is a slight decrease in particle size with increase in temperature. The particle size varies approximately from 40 nm to 34 nm with increase in temperature. The NPs were primarily elliptical in shape with some irregular shaped NPs. Some NPs appear to be aggregating as highlighted in blue arrows. The size distribution does not vary greatly for the 60 °C and 80 °C samples when compared to the 100 °C sample. Similarly, for $\text{Na}_3\text{Ct}/\text{HAuCl}_4$ ratio of 4.33:1 there was a slight decrease in the NP size with increase in temperature. The NP size varied approximately from 16 nm to 13 nm with increase in temperature. The NPs were either faceted or quasi-spherical in shape. The faceted NPs are highlighted with red arrows in the TEM images (Figure 2.5). The size distribution does not show any apparent change.

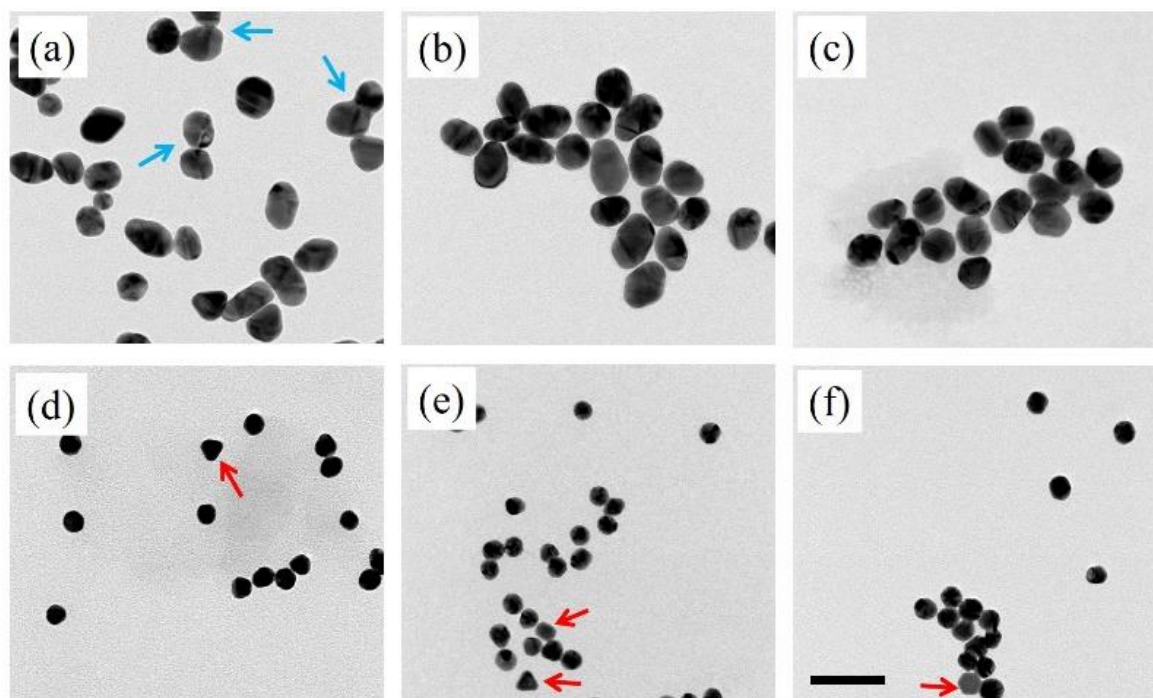


Figure 2.5 TEM images of Au NPs synthesized using $\text{Na}_3\text{Ct}/\text{HAuCl}_4$ ratio of 1.50:1 (a-c) and 4.33:1 (d-f) at temperatures of 60 °C (a, d), 80 °C (b, e) and 100 °C (c, f). The highlighted NPs are faceted. The scale bar for all TEM images is 50 nm.

When the Au NP size in the low and high concentration regimes were compared, it was very clear that the NP size of the low regime (~ 40 nm) was greater than the high regime (~ 16 nm). The shape of the NPs in the low regime was elliptical while those in the high regime were more spherical. Further, the Au NPs were polycrystalline in nature, which was evident from the presence of twinning planes seen in the TEM images. The selected area electron diffraction (SAED) patterns also suggests polycrystalline nature of the Au NPs. The indexed SAED pattern indicates the formation of a face-centered cubic structure of Au (Figure 2.6). It was also observed that the degree of polycrystallinity increased with decreasing temperatures. Thus, from the TEM studies and the UV-Vis data, it was confirmed that temperature plays a subtle role while the $\text{Na}_3\text{Ct}/\text{HAuCl}_4$ ratios play a dominant role in determining the size and morphology of the Au NPs.

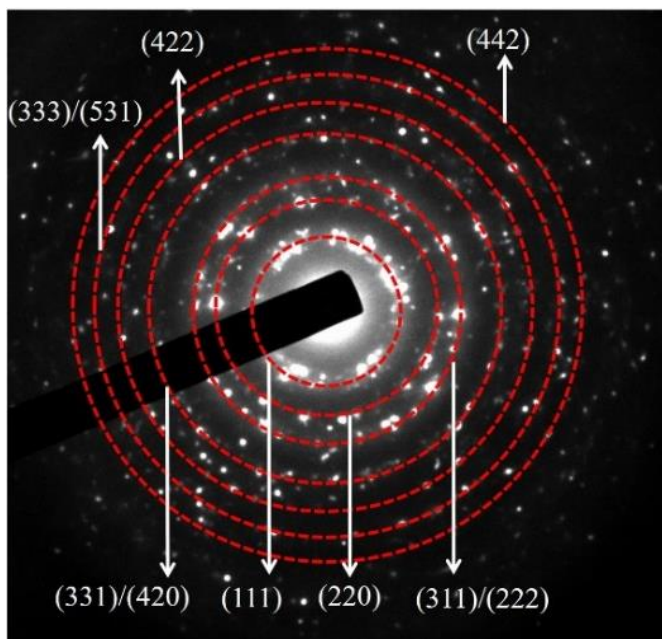


Figure 2.6 Indexed SAED pattern, of Au NPs synthesized at 80°C and a $\text{Na}_3\text{Ct}/\text{HAuCl}_4$ ratio of 4.33, indicates face-centered cubic structure of Au.

Thus in the next phase of our work, the investigation focused on monitoring the size and morphological evolution of the Au NPs during synthesis at different $\text{Na}_3\text{Ct}/\text{HAuCl}_4$

ratios in the low and high regime. A series of UV-Vis absorption measurements were performed during the synthesis at precise time intervals. The color changes of the reaction mixture were closely monitored and were related to nucleation (t_1) and growth (t_2) times. Figure 2.7 shows two absorption spectra for low and high regime samples with the $\text{Na}_3\text{Ct}/\text{HAuCl}_4$ ratios of 1.5:1 and 4.33:1 at 80 °C respectively. The synthesis temperature of 80 °C was selected so that a precise recording of color change can be done. For the low regime measurement (Figure 2.7a), the absorption spectra were recorded at 1 min, 1.5 min, 3 min and 40 min. The time of color change was recorded as $t_1 = 1$ min, $t_2 = 3$ min, which corresponded to nucleation and growth times respectively. The UV-Vis spectra show an evolution of absorption maxima with reaction time.

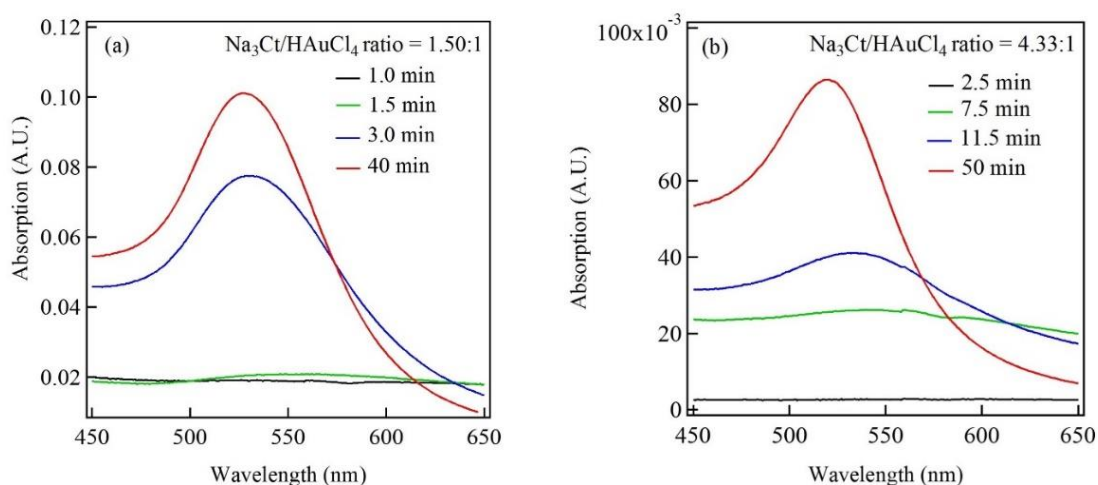


Figure 2.7 Evolution of UV-Vis absorption maxima as a function of reaction time (a) for $\text{Na}_3\text{Ct}/\text{HAuCl}_4$ ratio of 1.5 and (b) 4.33.

For the time $t_1 = 1$ min, there was no absorption maxima in the UV-Vis spectrum. As the reaction proceeded, a broad peak centered at 550 nm appeared in the UV-Vis spectrum. This broad peak was recorded at reaction time of 1.5 min. At time $t_2 = 3.0$ min the absorption maxima was recorded at 530 nm. After completion of the reaction, at time 40 min, the absorption maxima was at 526 nm. From the UV-Vis data it is evident that there is a blue

shift in the absorption maxima from 550 nm to 526 nm along with a decrease in the spectral width as the reaction proceeded. The UV-Vis spectra for the high regime sample (Figure 2.7b), shows similar trend. For the time $t_1 = 2.5$ min, a large hump was observed between 500 nm and 650 nm, centered approximately at 580 nm (Figure 2.7b). As the reaction progressed the absorption maxima underwent a blue shift from 540 nm to 519 nm. The final absorption maxima for the high regime sample was smaller than the low regime sample by 7 nm. Moreover, the FWHM of the high regime sample was smaller than the low regime sample. This reduction in absorption maxima and smaller FWHM for high regime sample indicates that the final NP size is smaller and has a narrow size distribution than the low regime sample. Further, the evolution of the absorption spectrum suggests that during the initial stages of synthesis the Au particles could be present in an aggregated form, which transform to stable Au NPs as the reaction progresses [12, 21].

With the help of our absorption data (Figure 2.7) and from the reports in literature it is clear that in the initial stage of synthesis the very small Au clusters have a tendency to aggregate. This occurs due to the high surface area to volume ratio making the small Au clusters thermodynamically unstable thus leading to aggregation. The broad absorption maxima obtained, in the UV-Vis data, during the initial stages of the reaction is attributed to the cumulative effect of the surface plasmon resonances, due to the presence of small Au particles of varying sizes within this aggregated form [21, 22]. Other factors contributing to aggregation are van der Waals attraction and the tendency of Au (III) complexes to attract metallic Au surfaces [12, 21, 23]. The small Au particles within the aggregates do not fuse but are kept in close proximity to each other via steric repulsion of the adsorbed citrate. As the reaction proceeds the absorption maxima undergoes a blue shift to 526 nm. During this

reaction the small Au particles disengage from the aggregate to form stable Au NPs, as these particles continue to get coated with citrate ions and the adsorbed Au (III) complexes reduce to metallic Au. The completion of the reaction is indicated by a red color of the final reaction mixture, as shown in Figure 2.2d.

Further, in the low concentration regime the unstable small Au clusters have a high tendency to aggregate as mentioned above. In this regime there are less citrate ions available to coat the Au nanoparticles and thus the aggregation is favored. Further, since the density of these small nanoparticles is large the probability of aggregation is high, which occurs via the van der Waals attraction [36]. The aggregation of Au clusters ceases when a critical size is achieved. The electrostatic repulsion due to the citrate ions stabilizes the Au clusters by coating the surface of the Au clusters. Further NP growth and surface energy minimization occurs via diffusion and Ostwald ripening respectively. This leads to the formation of large and elliptical Au nanoparticles in the low concentration regime (Figure 2.5a-c, Figure 2.5a highlighted with blue arrows). The elliptical shape of Au NPs is due to a combination of nanoparticle fusion [37], surface energy minimization, aggregative growth [38] and possibly Ostwald ripening [24, 39] of NPs (Figure A 2.3). The NPs seen in Figure 2.5a indicate that the formation of elliptical NPs could be mainly due to fusion and aggregative growth. Wang et al have provided a very clear distinction between aggregative growth and Ostwald ripening [38]. In Figure 2.5a, the occurrence of Ostwald ripening cannot be completely eliminated but may play a subtle role [39]. For the high concentration regime, the presence of large amount of citrate ions inhibits aggregation and random attachment of Au clusters, as these citrate ions create a coating on all available Au nanoparticle surfaces. A traditional nucleation and growth model is used to explain the faceted or quasi-spherical nanoparticle formation for

high citrate concentrations (Figure 2.5d-f) (See supporting information, Figure A 2.3) [37, 38].

Along with the study of size and morphological evolution, reaction time for various $\text{Na}_3\text{Ct}/\text{HAuCl}_4$ ratios was also investigated. As mentioned above, the time at which color changes occurred were meticulously recorded. Figure 2.8 below shows the reaction time, on a logarithmic scale, as a function of synthesis temperature for low and high concentration regimes.

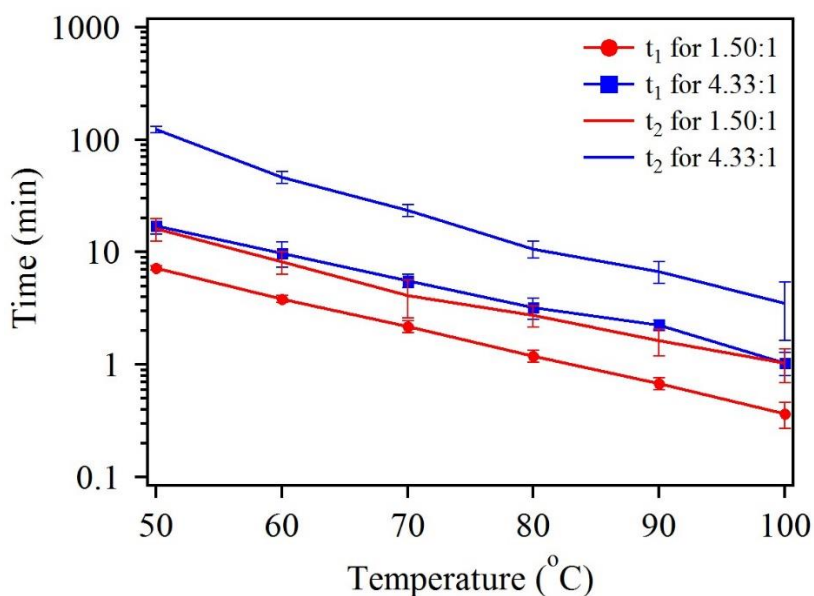


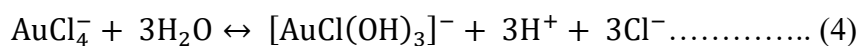
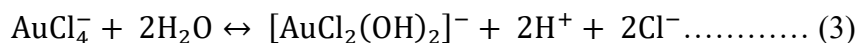
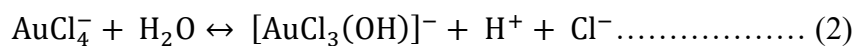
Figure 2.8 A logarithmic plot of reaction time as a function of synthesis temperature for low and high concentration regimes

There is a similar trend for both nucleation (t_1) and growth (t_2) times in the low and high regimes. An exponential decrease in the nucleation and growth time is recorded with increasing synthesis temperature for both regimes. This trend of increased reaction kinetics with temperature can be explained with the help of chemical reactions occurring during the Au NP formation.

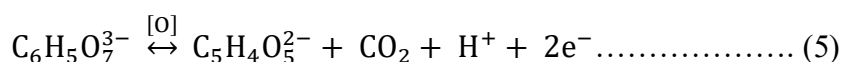
Dissolution of HAuCl_4 in water:



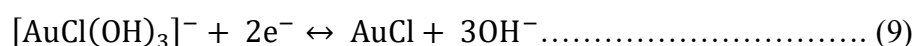
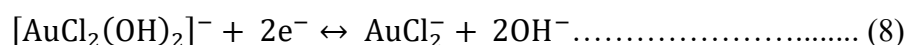
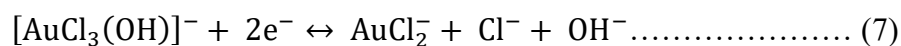
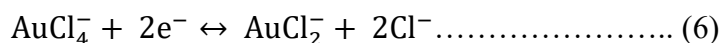
Hydrolysis of AuCl_4^- :



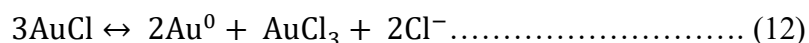
Oxidation of citrate to dicarboxy acetone:



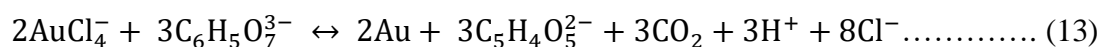
Reduction of Au (III) to Au (I):



Disproportionation of Au (I) to metallic Au:



Overall reaction:



HAuCl_4 undergoes hydrolysis to form a yellowish solution (Equations 1-4). After completion of hydrolysis, a redox reaction occurs, where citrate and Au (III) complex form dicarboxy acetone and Au (I) complex respectively (Equations 5-10). The dicarboxy acetone facilitates the grouping Au (I) complexes to form metallic Au nuclei through the disproportionation reaction (Equations 11 and 12). Gammons et al [30] have demonstrated

that Au (I) complex is more stable at higher temperatures. Thus as the reaction is carried out at higher temperatures the formation of Au (I) complex is favored. Consequently, there will be a higher concentration of Au (I) complex, which will also lead to the increase in the rate of disproportionation reaction. This relationship between the concentration of Au (I) complex and the rate of disproportionation reaction has been experimentally supported by Gammons et al [30]. Thus with increase in temperature, the rate of Au NP formation increases.

From the data, it is also evident that in the low concentration regime the nucleation (t_1) and growth (t_2) times for the Au NPs was less compared to the high regime samples. This is a clear indication that the Au NP formation rate is much slower at the high regime than at the low regime. At the high concentration regime, the pH of the reaction mixture is higher than the low concentration regime. This pH change affects the reactivity of the Au (III) complexes. Based on Huang's work [23] on the speciation of aqueous HAuCl_4 at various pH values, the AuCl_4^- complexes can include combinations of AuCl_4^- , $[\text{AuCl}_3(\text{OH})]^-$, and $[\text{AuCl}_2(\text{OH})_2]^-$. As the pH values increase, the Au (III) complexes become more stable and thus the citrate ions find it difficult to reduce the Au (III) complexes. Thus the time of reaction is lengthened when the pH of the reaction mixture is increased, which occurs in samples in the high concentration regime.

Conclusion

In summary, Au NPs were synthesized by the citrate reduction method. The variations in temperature, $\text{Na}_3\text{Ct}/\text{HAuCl}_4$ ratios and reaction times were closely studied. From this study it was evident that the Au NP size and morphology was strongly dependent on the $\text{Na}_3\text{Ct}/\text{HAuCl}_4$ ratios and the temperature played a subtle role. At low concentration

regime, the Au NPs were more elongated. The elongation occurred due to Oswald ripening. At high concentration regime, the Au NPs were more spherical or faceted. The reaction times varied approximately by an order of magnitude between the low and high concentration regime samples. The high regime samples required longer reaction times to reach completion, due to the presence of more stable Au (III) complexes in the solution.

References

- [1] Atwater H A and Polman A 2010 Plasmonics for improved photovoltaic devices *Nature Materials* **9** 8
- [2] Haruta M, Tsubota S, Kobayashi T, Kageyama H, Genet M J and Delmon B 1993 Low-Temperature Oxidation of CO over Gold Supported on TiO₂, α -Fe₂O₃, and Co₃O₄ *Journal of Catalysis* **144** 175-192
- [3] Jain P K, Lee K S, El-Sayed I H and El-Sayed M A 2006 Calculated Absorption and Scattering Properties of Gold Nanoparticles of Different Size, Shape, and Composition: Applications in Biological Imaging and Biomedicine *The Journal of Physical Chemistry B* **110** 7238-7248
- [4] Peng G, Tisch U, Adams O, Hakim M, Shehada N, Broza Y Y, Billan S, Abdah-Bortnyak R, Kuten A and Haick H 2009 Diagnosing lung cancer in exhaled breath using gold nanoparticles *Nat Nano* **4** 669-673

[5] Nakaso K, Shimada M, Okuyama K and Deppert K 2002 Evaluation of the change in the morphology of gold nanoparticles during sintering *Journal of Aerosol Science* **33** 1061-1074

[6] Lo Y-S, Liu K-C, Wu J-Y, Hou C-H and Wu T-B 2008 Bandgap engineering of tunnel oxide with multistacked layers of Al₂O₃/HfO₂/SiO₂ for Au-nanocrystal memory application *Applied Physics Letters* **93** 132907

[7] Zhao P, Li N and Astruc D 2013 State of the art in gold nanoparticle synthesis *Coordination Chemistry Reviews* **257** 638-665

[8] Padalkar S, Hulleman J, Deb P, Cunzeman K, Rochet J C, Stach E A and Stanciu L 2007 Alpha-synuclein as a template for the synthesis of metallic nanowires *Nanotechnology* **18** 055609

[9] Padalkar S, Capadona J R, Rowan S J, Weder C, Won Y-H, Stanciu L A and Moon R J 2010 Natural Biopolymers: Novel Templates for the Synthesis of Nanostructures *Langmuir* **26** 8497-8502

[10] Chandran S P, Chaudhary M, Pasricha R, Ahmad A and Sastry M 2006 Synthesis of Gold Nanotriangles and Silver Nanoparticles Using Aloe Vera Plant Extract *Biotechnol. Prog.* **22** 6

[11] Mathias Brust, Merryl Walker, Donald Bethell, Schiffrin D J and Whyman R 1994 Synthesis of thiol-derivatised gold nanoparticles in a two-phase Liquid-Liquid system *J. Chem. Soc., Chem. Commun.* **2**

[12] Turkevich J, Stevenson P C and Hillier J 1951 A study of the nucleation and growth process in the synthesis of colloidal gold *Discuss. Faraday Soc.* **11** 20

[13] Kumar S, Gandhi K S and Kumar R 2007 Modeling of Formation of Gold Nanoparticles by Citrate Method *Industrial & Engineering Chemistry Research* **46** 3128-3136

[14] Brust M, Walker M, Bethell D, Schiffrin D J and Whyman R 1994 Synthesis of thiol-derivatised gold nanoparticles in a two-phase Liquid-Liquid system *Journal of the Chemical Society, Chemical Communications* 801-802

[15] Rohiman A, Anshori I, Surawijaya A and Idris I 2011 Study of Colloidal Gold Synthesis Using Turkevich Method *AIP Conference Proceedings* **1415** 39-42

[16] Frens G 1973 Controlled Nucleation for the Regulation of the Particle Size in Monodisperse Gold Suspensions *Nature Physical Science.* **241** 2

[17] Wuithschick M, Birnbaum A, Witte S, Sztucki M, Vainio U, Pinna N, Rademann K, Emmerling F, Kraehnert R and Polte J 2015 Turkevich in New Robes: Key

Questions Answered for the Most Common Gold Nanoparticle Synthesis *ACS Nano* **9** 7052-7071

[18] Schulz F, Homolka T, Bastús N G, Puentes V, Weller H and Vossmeier T 2014 Little Adjustments Significantly Improve the Turkevich Synthesis of Gold Nanoparticles *Langmuir* **30** 10779-10784

[19] Bastús N G, Comenge J and Puentes V 2011 Kinetically Controlled Seeded Growth Synthesis of Citrate-Stabilized Gold Nanoparticles of up to 200 nm: Size Focusing versus Ostwald Ripening *Langmuir* **27** 11098-11105

[20] Kimling J, Maier M, Okenve B, Kotaidis V, Ballot H and Plech A 2006 Turkevich Method for Gold Nanoparticle Synthesis Revisited *The Journal of Physical Chemistry B* **110** 15700-15707

[21] Ji X, Song X, Li J, Bai Y, Yang W and Peng X 2007 Size Control of Gold Nanocrystals in Citrate Reduction: The Third Role of Citrate *Journal of the American Chemical Society* **129** 13939-13948

[22] Chow M K and Zukoski C F 1994 Gold Sol Formation Mechanisms: Role of Colloidal Stability *Journal of Colloid and Interface Science* **165** 97-109

[23] Wang S, Qian K, Bi X and Huang W 2009 Influence of Speciation of Aqueous HAuCl₄ on the Synthesis, Structure, and Property of Au Colloids *The Journal of Physical Chemistry C* **113** 6505-6510

[24] Patungwasa W and Hodak J H 2008 pH tunable morphology of the gold nanoparticles produced by citrate reduction *Materials Chemistry and Physics* **108** 45-54

[25] Wenchao Ding, Peina Zhang, Yijing Li, Haibing Xia, Dayang Wang and Tao X 2015 Effect of Latent Heat in Boiling Water on the Synthesis of Gold Nanoparticles of Different Sizes by using the Turkevich Method *ChemPhysChem* **16** 7

[26] Cubillana-Aguilera L M, Franco-Romano M, Gil M L A, Naranjo-Rodríguez I, Hidalgo-Hidalgo de Cisneros J L and Palacios-Santander J M 2011 New, fast and green procedure for the synthesis of gold nanoparticles based on sonocatalysis *Ultrasonics Sonochemistry* **18** 789-794

[27] Su C-H, Wu P-L and Yeh C-S 2003 Sonochemical Synthesis of Well-Dispersed Gold Nanoparticles at the Ice Temperature *The Journal of Physical Chemistry B* **107** 14240-14243

[28] Young J, Lewinski N, Langsner R, Kennedy L, Satyanarayan A, Nammalvar V, Lin A and Drezek R 2011 Size-controlled synthesis of monodispersed gold nanoparticles via carbon monoxide gas reduction *Nanoscale Research Letters* **6** 1-11

- [29] Jana N R, Gearheart L and Murphy C J 2001 Wet Chemical Synthesis of High Aspect Ratio Cylindrical Gold Nanorods *The Journal of Physical Chemistry B* **105** 4065-4067
- [30] Gammons C H, Yu Y and Williams-Jones A E 1997 The disproportionation of gold(I) chloride complexes at 25 to 200°C *Geochimica et Cosmochimica Acta* **61** 1971-1983
- [31] Pei L, Mori K and Adachi M 2004 Formation Process of Two-Dimensional Networked Gold Nanowires by Citrate Reduction of AuCl₄⁻ and the Shape Stabilization *Langmuir* **20** 7837-7843
- [32] Pong B-K, Elim H I, Chong J-X, Ji W, Trout B L and Lee J-Y 2007 New Insights on the Nanoparticle Growth Mechanism in the Citrate Reduction of Gold(III) Salt: Formation of the Au Nanowire Intermediate and Its Nonlinear Optical Properties *The Journal of Physical Chemistry C* **111** 6281-6287
- [33] Haiss W, Thanh N T K, Aveyard J and Fernig D G 2007 Determination of Size and Concentration of Gold Nanoparticles from UV–Vis Spectra *Analytical Chemistry* **79** 4215-4221

[34] Jain P K, Lee K S, El-Sayed I H and El-Sayed M A 2006 Calculated Absorption and Scattering Properties of Gold Nanoparticles of Different Size, Shape, and Composition: Applications in Biological Imaging and Biomedicine *The Journal of Physical Chemistry B* **110** 10

[35] Link S and El-Sayed M A 1999 Size and Temperature Dependence of the Plasmon Absorption of Colloidal Gold Nanoparticles *The Journal of Physical Chemistry B* **103** 4212-4217

[36] Biggs S, Mulvaney P, Zukoski C F and Grieser F 1994 Study of Anion Adsorption at the Gold-Aqueous Solution Interface by Atomic Force Microscopy *Journal of the American Chemical Society* **116** 9150-9157

[37] Gubicza J, Lábár J L, Quynh L M, Nam N H and Luong N H 2013 Evolution of size and shape of gold nanoparticles during long-time aging *Materials Chemistry and Physics* **138** 449-453

[38] Wang F, Richards V N, Shields S P and Buhro W E 2014 Kinetics and Mechanisms of Aggregative Nanocrystal Growth *Chemistry of Materials* **26** 5-21

[39] Shields S P, Richards V N and Buhro W E 2010 Nucleation Control of Size and Dispersity in Aggregative Nanoparticle Growth. A Study of the Coarsening Kinetics of Thiolate-Capped Gold Nanocrystals *Chemistry of Materials* **22** 3212-3225

Appendix

Table A 2.1 *The pH value of the reaction mixture with varying $\text{Na}_3\text{Ct}/\text{HAuCl}_4$ ratios.*

Sr. No.	$\text{Na}_3\text{Ct}/\text{HAuCl}_4$	pH of reaction mixture
1	0.00	3.28
2	1.25	4.15
3	1.50	4.28
4	1.75	4.53
5	2.25	4.90
6	2.66	5.08
7	3.50	5.66
8	4.33	5.81

It was observed that the pH value increased with increasing $\text{Na}_3\text{Ct}/\text{HAuCl}_4$ ratios.

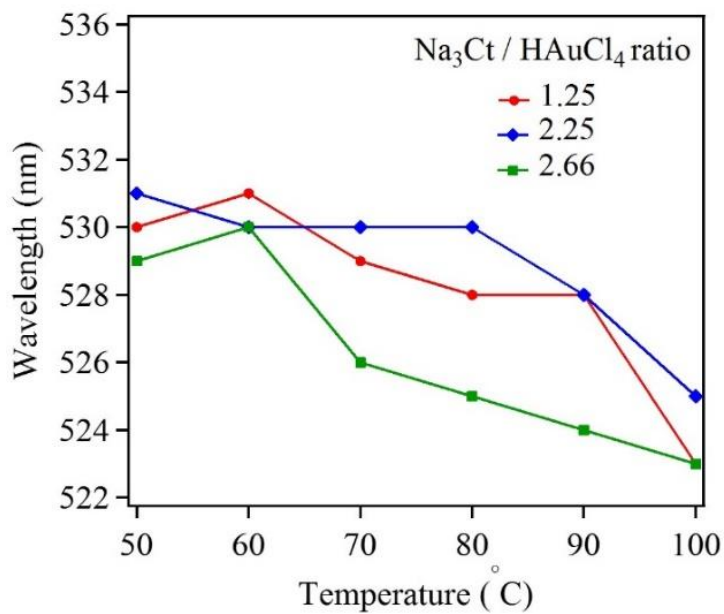


Figure A 2.1 *Absorption peak as a function of temperature for three $\text{Na}_3\text{Ct}/\text{HAuCl}_4$ ratios, showing a small decrease in absorption maxima with increasing temperature*

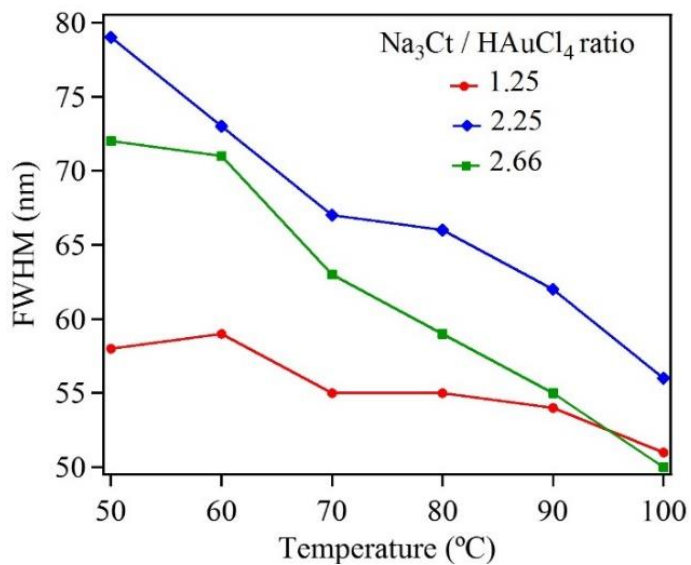


Figure A.2.2 Full width at half maxima (FWHM) as a function of temperature for three $\text{Na}_3\text{Ct}/\text{HAuCl}_4$ ratios, show a slight decrease in FWHM with increasing temperature

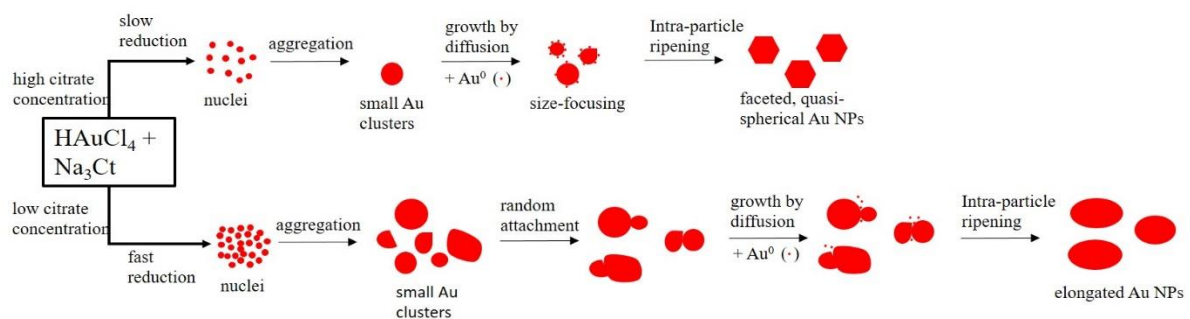


Figure A.2.3 Mechanism of NP shape evolution in high and low concentration regime

CHAPTER 3. FORMATION OF SIZE AND DENSITY CONTROLLED NANOSTRUCTURES BY GALVANIC DISPLACEMENT

M. Tran¹, S. Roy¹, A. Whale², S. Martin², S. Sundararajan¹, and S. Padalkar^{1,3} *

¹ Department of Mechanical Engineering, Iowa State University, Ames, IA 50011, USA

² Department of Materials Science and Engineering, Iowa State University, Ames, IA 50011, USA

³ Microelectronics Research Center, Iowa State University, Ames, IA 50011, USA

* Email: padalkar@iastate.edu

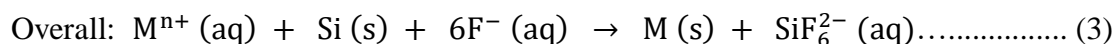
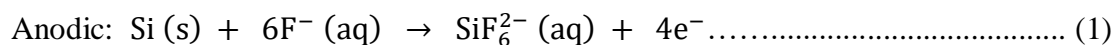
Abstract

Gold (Au) and copper (Cu)-based nanostructures are of great interest due to their applicability in various areas including catalysis, sensing and optoelectronics. Nanostructures synthesized by the galvanic displacement method often lead to non-uniform density and poor size distribution. Here, density and size controlled synthesis of Au and Cu-based nanostructures was made possible by galvanic displacement with limited exposure to hydrofluoric (HF) acid and the use of surfactants like L-cysteine (L-Cys) and cetyltrimethylammonium bromide (CTAB). An approach involving cyclic exposure to HF acid regulated the nanostructure density. Further, the use of surfactants generated monodispersed quantum sized nanoparticles in the initial stage of the deposition with increased density. The characterization of Au and Cu-based nanostructures was performed by scanning electron microscopy, UV-Visible spectroscopy, X-ray photoelectron spectroscopy, Raman spectroscopy and X-ray diffraction. SERS measurements indicated that Si substrates deposited with Au nanostructures enhanced Raman signals of Rhodamine 6G dye up to three orders of magnitude

Introduction

Galvanic displacement is an electroless deposition technique utilized for the deposition of metals on semiconducting substrates¹⁻². This synthesis method has gained much attention in the past decade since it is a simple and inexpensive way of preparing zero and two dimensional metal nanostructures. Moreover, it does not require complicated chemical apparatus, electrical source, electrodes and can be performed under ambient conditions in a short duration of time. The synthesis is also applicable for substrates with complex geometries including patterned planar substrates and nanowires. Due to these advantages of galvanic displacement method there has been a surge in scientific reporting that explore the deposition of metallic nanostructures on semiconductor surfaces¹⁻⁵. These deposited metallic nanostructures are either randomly distributed or specifically patterned on the substrate. There are also other literature reports that utilize this synthesis method to study fundamental aspects like growth behavior of metals on the underlying substrates and the characteristic of their interface^{4, 6-8}. The galvanic displacement technique has been utilized for the deposition of several metals and base metals including Au^{6-7, 9-10}, silver (Ag)^{6, 8, 11}, platinum (Pt)^{6, 12-13}, palladium (Pd)⁶, nickel (Ni)¹⁴, and Cu^{5, 14-17} on Si, germanium (Ge)^{6, 18} and III-V semiconductor substrates¹.

In this deposition method, the semiconducting substrate provides electrons via surface oxidation. These available electrons are used to reduce the metal cations in solution to their metallic state, resulting in deposition of the metal on the substrate. The following chemical equations describe the galvanic displacement reactions on silicon (Si) substrate, where M denotes any metal with a standard redox potential more positive than that of the substrate. Here HF acid is used to maintain the supply of electrons by the dissolution of surface oxides on the substrate^{1, 9}.



Many studies on galvanic displacement have been carried out with the objective of synthesizing Au nanoparticles or films. These Au nanostructures serve as a good model system for other metals. Also the redox potential of Au is greater than other desirable metals. Thus the Au precursor can be readily reduced to metallic Au, making easy synthesis of Au nanostructures^{6,9}. Moreover, there are several potential applications for Au nanostructures in a variety of areas. Further, the plasmonic properties of Au nanostructures can be tuned by varying the size and shape of the nanostructures. These plasmonic properties can be exploited for surface enhanced Raman spectroscopy¹⁹⁻²⁰, solar cells²¹, detection of bioanalytes²², optoelectronics and also for photocatalysis^{12,23}. Additionally, the knowledge acquired by thoroughly studying the galvanic displacement method for the deposition of Au nanostructures is valuable and can be applied to other metallic systems like Ag, Pt, Cu etc. Lately, Cu nanostructures have been gaining importance since there are potential applications that can benefit from the plasmonic properties of Cu nanostructures. Also, Cu is a favorable material of choice due to its inherent advantages like high electrical and thermal conductivity, high electromigration resistance and easy functionality^{15, 24-25}. Moreover, Cu is an inexpensive and abundantly available metal. Thus due to these benefits, Cu nanostructures have been synthesized by various routes including the above mentioned galvanic displacement method.

The metallic nanostructures synthesized by galvanic displacement are often found to be of random size and distribution²⁶⁻²⁷. It has been difficult to precisely control the

nanostructure size and density and thus has been the limiting factor for this synthesis technique. In this work we successfully demonstrate a modification of the galvanic displacement method, in which surfactants like L-Cys and CTAB have been incorporated, to obtain controlled density, size and distribution of the deposited nanostructures. Additionally, the nanostructures can be easily removed from the substrate, making the substrate available for the deposition of nanostructures. Thus the substrate becomes reusable and the removed nanostructures do not agglomerate due to the presence of the surfactants. Further, morphological evolution of the nanostructures was controlled as the synthesis process proceeded. We have synthesized Au and Cu-based nanostructures on Si substrate. The nanoparticle size as small as 7 nm has been deposited in both material systems. Our findings indicate that the surfactants, like L-cysteine and CTAB, play an important role in obtaining very dense, monodispersed nanoparticles. Scanning electron microscopy was used to study the size, size distribution and morphological evolution. The compositional analysis was carried out by X-ray diffractometer, X-ray photoelectron spectroscopy and Auger electron spectroscopy. The absorption properties were studied using UV-Visible spectroscopy. The scattering property of Au nanostructures was evaluated by Raman spectroscopy for application in surface-enhanced Raman spectroscopy (SERS)

Experimental Details

The chemicals used for metal deposition included gold (III) chloride trihydrate ($\text{HAuCl}_4 \cdot 3\text{H}_2\text{O}$, $\geq 99.9\%$) and cetyltrimethylammonium bromide (CTAB) ($\text{C}_{19}\text{H}_{42}\text{BrN}$, $\geq 99.9\%$) purchased from Sigma Aldrich (Milwaukee, WI, USA), cupric sulfate pentahydrate ($\text{CuSO}_4 \cdot 5\text{H}_2\text{O}$, $\geq 98\%$) from Fisher Scientific (Hanover Park, IL, USA), and L-cysteine ($\text{C}_3\text{H}_7\text{NO}_2\text{S}$, $\geq 98\%$) from EMD Millipore (Billerica, MA, USA). These chemicals were used as received. The HF acid (48%) was purchased from Macron Fine Chemicals (Center Valley,

PA, USA). All solutions were prepared using deionized water. The HF acid was always contained in a polypropylene beaker for experimental purposes. The Si (100) substrate (4" wafer, single-crystalline, n-type, $\rho = 3-9 \Omega \text{ cm}$) was purchased from El-Cat Inc. (Ridgefield Park, NJ, USA). For SERS measurements, Rhodamine 6G dye (R6G, 99%) and paraoxon-ethyl ($\text{C}_{10}\text{H}_{14}\text{NO}_6\text{P}$, $\geq 90\%$) were purchased from Sigma Aldrich (Milwaukee, WI, USA)

Prior to the deposition, the Si wafer was cleaved into $1.5 \times 1.5 \text{ cm}^2$ pieces and thoroughly cleaned using acetone followed by ethanol (100%, 200 proof) and deionized water. Each cleaning step was carried out for 10 minutes, in an ultrasonic bath, in order to degrease and decontaminate the Si substrate. The clean Si substrate was dried on a kimwipe. In the next step of the synthesis the clean Si substrate was immersed in to 10% (w/w) aqueous HF solution for 2 minutes. The HF acid dissolves the surface oxide on the substrate and forms hydrogen terminated surface. Following HF immersion step, the Si substrate was immediately immersed in 0.3 mM HAuCl_4 or CuSO_4 for 5 minutes to obtain Au or Cu-based nanostructures respectively on the Si substrate. Finally, the Si substrate was thoroughly rinsed by deionized water and dried on a kimwipe. To increase the density of the deposited nanostructures, the above procedure, called as one cycle (1X), was repeated up to ten times (10X). To further increase the nanostructure density and control the nanostructure size, 0.1 mM surfactants like L-cysteine or CTAB were mixed independently with 0.3 mM metal precursor solutions and utilized in the deposition process. Figure 3.1 describes the entire deposition process called as one cycle (1X). To prepare the dye solution, 0.8 mg of R6G was dissolved in 5 mL of deionized water, and used as stock solution. Similarly, paraoxon stock solution was prepared by mixing 30 μL of oily concentrated paraoxon with 0.98 mL deionized water. To prepare sample for SERS measurement, a small volume of the stock

solution was diluted to the desired concentration. Then, 300 μL of the diluted solution was drop cast onto the sample, and was dried under ambient condition. To improve wetting, prior to drop casting, the sample was treated with ambient air plasma for 1 minute under medium radio frequency power level (11 W) by a plasma cleaner (PDC-001, Harrick Plasma, Ithaca, NY)

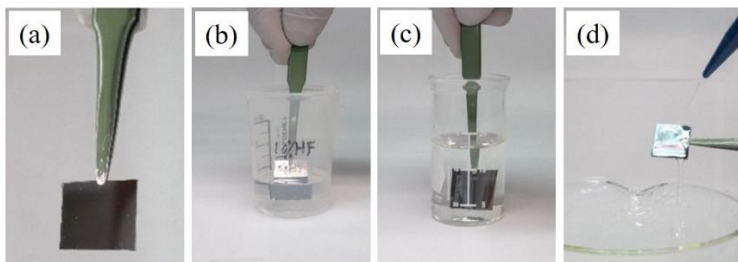


Figure 3.1 *Experimental steps of the synthesis process. (a) Cleaved and cleaned Si substrate. (b) Immersion in 10% HF for 2 min, to dissolve the surface oxide. (c) Immersion in 0.3 mM metal precursor solution for 5 min. (d) Rinse sample with deionized water.*

The size, size distribution and morphology of the nanostructures were studied by scanning electron microscopy (SEM) using a FEI Quanta-250 SEM instrument at 10 kV accelerating voltage. Topography of the generated surfaces was obtained by atomic force microscopy (AFM) using a Veeco Dimension 3100 AFM instrument in intermittent contact mode with a commercial Si probe (nominal radius~8nm, nominal frequency~320 kHz) at a scan size of $2\mu\text{m} \times 2\mu\text{m}$. To investigate the composition and crystallinity of the nanostructures, X-ray diffraction (XRD) was performed using the Siemens D500 instrument. The absorption properties were analyzed by obtaining UV-Visible (UV-Vis) absorption spectra. For the UV-Vis absorption measurement the samples were prepared by sonicating the Au nanoparticles off the Si substrate using 1.5 mL of deionized water. The sonication was carried out for 3 min. The Au nanoparticles suspended in deionized water was used for UV-Vis measurements. The oxidation states of the synthesized nanostructures were studied using an X-ray photoelectron spectroscopy (XPS), a Kratos Amicus/ESCA 3400 instrument.

For the XPS data acquisition, the sample was irradiated with a 240 W Mg K α X-ray and the photoelectrons normal to the substrate were analyzed. Auger electron spectroscopy (AES) was also utilized for sample characterization. Raman measurements were performed at room temperature on a Renishaw Dispersive Raman Spectrometer with Ar-ion laser of 488 nm. A 50X objective lens with incident power density of 8.2 mW/cm² and a total accumulation time of 2 min was used to acquire Raman data. The Raman spectra were collected from several random locations on each sample to confirm reproducibility.

Results and Discussion

The SEM images in Figure 3.2 represent Au nanostructures synthesized during successive deposition cycles from the first to the tenth cycle and show the corresponding morphological evolution of the Au nanoparticles. After the completion of the first deposition cycle the Au nanostructures appeared to be quasi-spherical in shape with an average diameter of 14 nm (Figure 3.2a). The nanoparticles were not deposited uniformly over the entire Si substrate. With the second deposition cycle the Au nanostructures were a combination of quasi-spherical nanoparticles and elongated branched nanostructures. The additional deposition cycles produced more nanostructures on the substrate and the morphological evolution of the deposited Au nanostructures was evident. Up to five deposition cycles, Au nanostructures appeared as chains of nanoparticles having a continuous network, and the average width of the Au nanostructures increased from 18 nm to 32 nm. Then, after six deposition cycles, the chains of nanoparticles coalesced further to form a sub-monolayer. Upon increasing to eight and ten deposition cycles, Au nanostructures grew more vertically, and their coverage shrank slightly. The observed shrinking of Au coverage was a general behavior of metals when deposited on semiconductor substrates,²⁸ possibly due to further coalescence and intra-nanostructure ripening. With increase in the deposition cycle, the Au

nanostructures appeared as chains of nanoparticles having a continuous network. The average width of the Au nanostructure increased from 18 nm to 32 nm with increase in the deposition cycles.

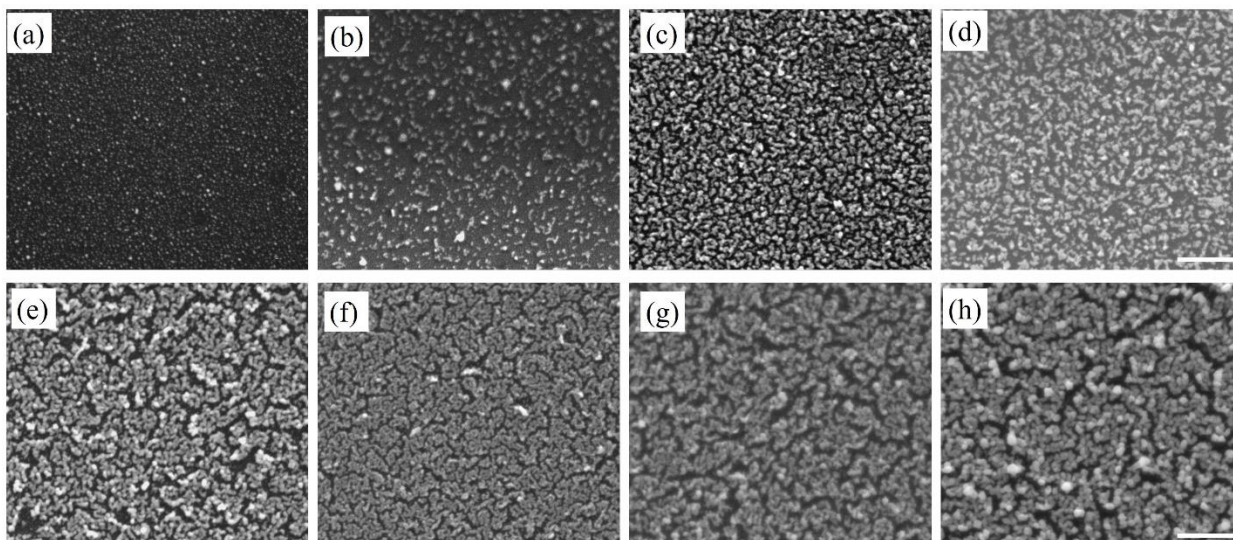


Figure 3.2 *SEM images of Au nanostructures deposited on Si substrate after (a) first, (b) second, (c) third, (d) fourth and (e) fifth, (f) sixth, (g) eighth, and (h) tenth deposition cycle. The scale bar is 500 nm.*

Along with the deposition of Au nanostructures, Cu-based nanostructures were also deposited using the galvanic displacement technique (Figure 3.3). Unlike Au nanostructures, the deposited Cu-based nanostructures were sparse during the initial deposition cycles. This sparse deposition could be due to the lower redox potential of Cu compared to Au. With increase in the deposition cycles the Cu-based nanostructure's number density increased. The nanostructures exhibited additional polydispersity, since nucleation and growth occurred during every deposition cycle. Moreover, the morphological evolution did not follow similar trend established by the Au nanostructures. There was no evidence of nanoparticle chain formation since each nanoparticle appeared as an individual entity. The average size of the Cu-based nanostructure increased from 23 nm to 42 nm with increasing deposition cycles. The difference in the morphological evolution between Au and Cu-based nanostructures

could be governed by the difference in their surface energies. The Au nanostructures appeared like a network of nanoparticle chains, while the Cu-based nanostructures appeared more spherical with limited agglomeration. It has been demonstrated in literature that the surface energies of low index planes for Au are much lower than that of Cu. Thus surface energies of low index planes could influence the resulting morphologies^{6, 9, 29}.

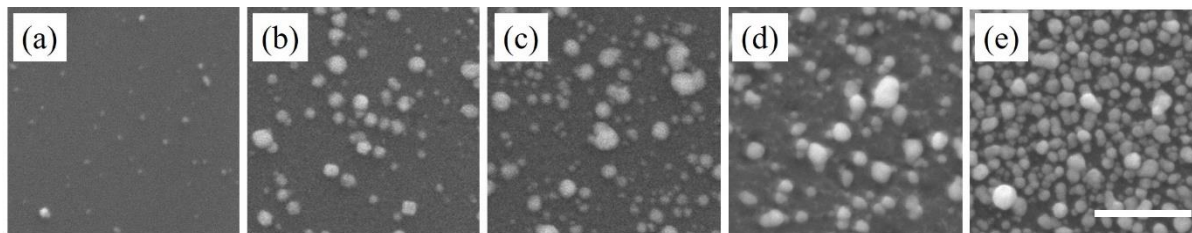


Figure 3.3 SEM images of Cu-based nanostructures deposited on Si substrate after (a) first, (b) second, (c) third, (d) fourth and (e) fifth deposition cycle. The scale bar is 500 nm.

From the SEM images, it was clear that the deposition of Au and Cu-based nanostructures on the Si substrate occurred via the Volmer-Weber growth mode. The number density of the deposited nanostructures in the first cycle appeared to be higher than the immediate successive cycle. This initial decrease in the number density could be attributed to weak adhesion between the deposited nanostructures and the underlying Si substrate⁹. Also in the Volmer-Weber growth mode the binding energy between atoms within the deposited nanostructures is higher than that with the substrate. However, with increase in the deposition cycles the number density increases, which perhaps occurs after the stabilization of the initial nanoparticle size. Further, availability of the Si substrate is important since additional deposition is possible if regions on the Si substrate are accessible for reaction with HF acid. Alongside due to the nature of this deposition process there is nucleation and growth occurring at every deposition cycle, which leads to additional polydispersed nanostructures.

In order to decrease the polydispersity, the use of surfactants has been a common practice. Surfactants like L-cysteine (L-Cys) and cetyl trimethylammonium bromide (CTAB) are often used for the stabilization of nanoparticles in solutions³⁰⁻³¹ and also on templates³²⁻³³. The ability of surfactants to selectively adsorb on crystal facets facilitates the control of size and morphology of the synthesized nanostructures. Thus the surfactants, L-Cys and CTAB were used during the deposition process. The surfactants were added independently into the Au and Cu precursor solutions and the final solution was used for the deposition of Au and Cu-based nanostructures. Figures 3.4-3.7 show SEM images of Au and Cu-based nanostructures deposited in the presence of L-Cys and CTAB. The presence of surfactants drastically reduced the nanostructure size and produced highly dense monodispersed nanoparticles during the initial deposition cycle. The reduction in size indicated that surfactants adsorbed on the deposited nanostructures and impeded their growth and also minimized their surface energy. It is known from the literature that L-Cys promotes the growth of Au nanostructures in the $\langle 111 \rangle$ direction by adsorbing on high surface energy planes³⁴⁻³⁵. It is also known that CTAB has a tendency to adsorb on to the (100) and (110) planes of fcc crystal structure³⁶⁻³⁷.

Consequently, the highly reduced nanoparticle size, facilitated the availability of larger Si substrate area for further reaction. Thus, there was an increase in the overall nanostructure density when compared with their non-surfactant counterparts. Figure A 3.1, in the supplementary information provides number density for Au and Cu-based nanoparticles after the completion of the first deposition cycle. It was noted that the number density increased by several times for both Au and Cu-based nanoparticles compared to their non-surfactant counterparts. During all the deposition cycles, the Au nanostructures underwent

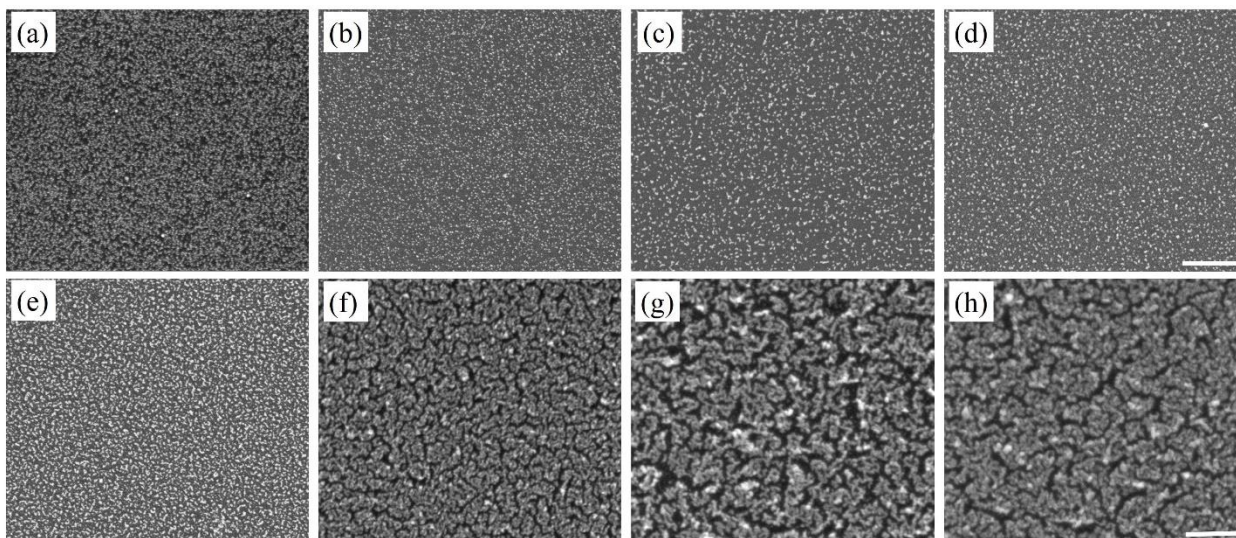


Figure 3.4 SEM images of Au nanostructures deposited on Si substrate after (a) first, (b) second, (c) third, (d) fourth and (e) fifth, (f) sixth, (g) eighth, and (h) tenth deposition cycle with L-Cys added as surfactant. The scale bar is 500 nm.

morphological evolution. The overall evolution demonstrated quite similar trends to their non-surfactant counterparts with the distinction of obtaining consistently lower nanostructure sizes and narrow size distribution at low numbers of deposition cycles, typically 1X – 5X. Noticeably, Au nanostructures with L-Cys as additive appeared to have the slowest growth rate. Based on our results with 1X – 5X, Cu nanostructures with either additive would be expected to grow in the same manner as Au nanostructures.

The average nanoparticle size of Au and Cu-based samples is given, for comparison, in Table 3.1. From the table it is clear that the Cu-based nanoparticles are larger in size compared to the Au nanoparticles after the completion of the first deposition cycle.

Additionally, the size of Au and Cu nanoparticles deposited in the presence of surfactants was consistently smaller than their non-surfactant counterparts. It was also noted that the number density of Cu-based nanoparticles was lower than that of Au nanoparticles (Figure A 3.1). The lower number density of Cu-based nanoparticles, compared to Au nanoparticles, could be attributed to the lower redox potential of Cu compared to Au^{6,9}. Furthermore, the

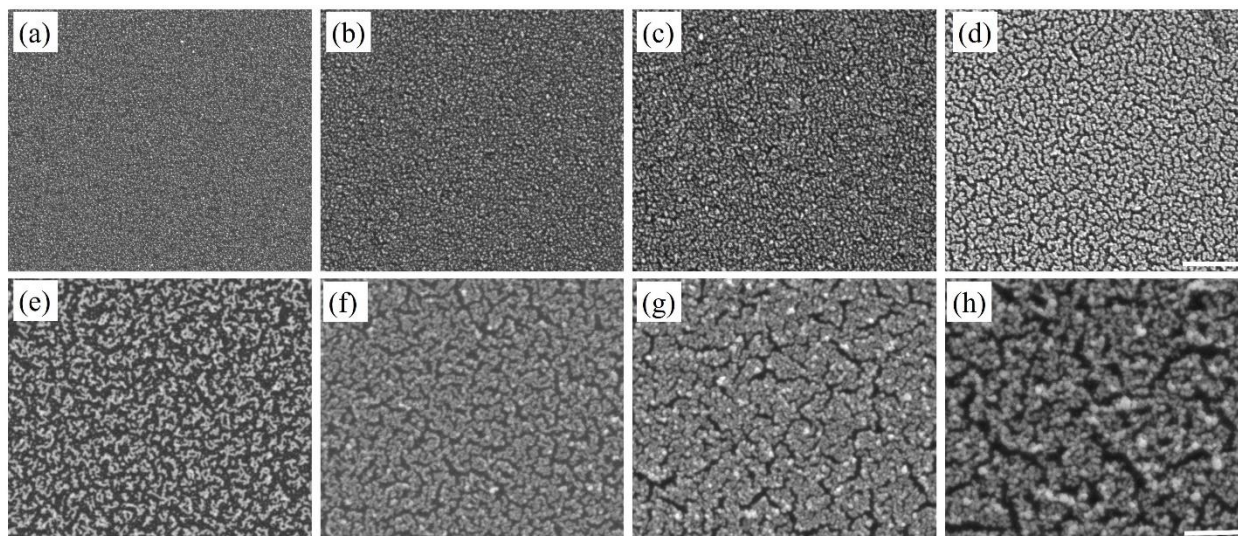


Figure 3.5 SEM images of Au nanostructures deposited on Si substrate after (a) first, (b) second, (c) third, (d) fourth and (e) fifth, (f) sixth, (g) eighth, and (h) tenth deposition cycle with CTAB added as surfactant. The scale bar is 500 nm.

surface energy of low index planes of Au is lower than Cu, leading to the formation of larger nanoparticles with small number density²⁹. The nanoparticle size distribution for all the Au and Cu-based samples was also obtained by analyzing 300 – 5000 nanoparticles. The size distribution data is presented in the supplementary information Figure A 3.2).

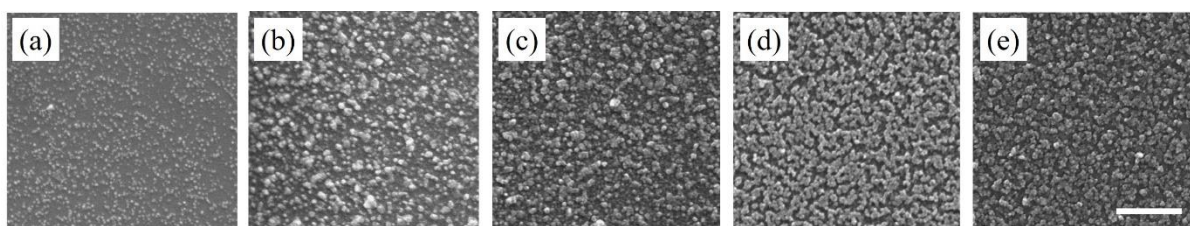


Figure 3.6 SEM images of Cu-based nanostructures deposited on Si substrate after (a) first, (b) second, (c) third, (d) fourth and (e) fifth deposition cycle with L-Cys added as surfactant. The scale bar is 500 nm

As mentioned above the number density of Au and Cu-based nanostructures increased in the presence of surfactants. Thus the formation of high density nanostructures can be promoted by the presence of surfactants. The two surfactants, L-Cys and CTAB are reported to act as mild reductants^{31, 34, 38-40}. There are literature reports indicating that

Table 3.1 Average nanoparticle size for Au and Cu-based nanoparticles after first deposition cycle

Type of nanoparticles	Nanoparticle size (nm) after first deposition cycle		
	Without surfactant	With L-Cys	With CTAB
Au samples	11 ± 4	8 ± 3	9 ± 3
Cu-based samples	23 ± 5	18 ± 7	19 ± 5

each thiol group of L-Cys is capable of donating one electron to reduce metal ions. The metal ions bind to the remaining L-Cys to form a complex. Thus several of the metal ion – cysteine complexes can undergo polymerization forming macromolecular structures, which can be degraded by the electrons from the Si substrate. Consequently, the metal ions were reduced to metallic Au (0) or Cu (0). Thus, the additional reduction function of L-Cys surfactant and the ability to concentrate metal (I) ions within the macromolecular structure facilitated the galvanic displacement process to form highly dense nanostructures with reduced size.⁴¹

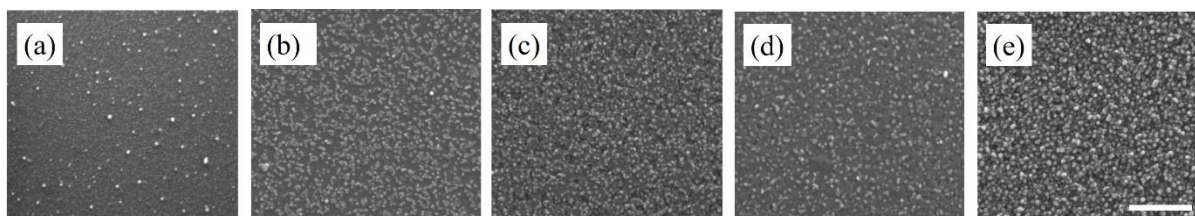


Figure 3.7 SEM images of Cu-based nanostructures deposited on Si substrate after (a) first, (b) second, (c) third, (d) fourth and (e) fifth deposition cycle with CTAB added as surfactant. The scale bar is 500 nm

Similarly, CTAB has also been reported as a mild reductant. The negatively charged Au precursor (AuCl_4^-) binds to the cationic CTAB surfactant via electrostatic interactions. The degradation of the long carbon chains in CTAB facilitates the reduction of the metal ions⁴²⁻⁴³. For Cu-based nanostructures, the Cu^{2+} cation will not electrostatically interact with CTAB head group. However, the Cu^{2+} ions could bind with CTAB via intermediate Br^-

counterions and thus participate in the reduction process. More detailed study will be carried out in the future to clearly elucidate the reduction mechanism of metal ions to metallic Au (0) or Cu (0) in the presence of surfactants like L-Cys and CTAB.

To investigate whether surfactant adsorption to Si substrate would affect the overall density and size distribution of the nanostructures, we conducted the following additional experiments. In one set of experiments, Si substrate was first immersed in 10% HF solution for 2 minutes, followed by 0.1 mM L-Cys solution for 5 minutes, then 0.3 mM HAuCl₄ solution for 5 minutes. Next, the same experimental sequence was performed, except that the final solution contained a mixture of 0.3 mM HAuCl₄ and 0.1 mM L-Cys. In another set of experiments, CTAB was used in place of L-Cys while other conditions and reagents were maintained. Figure 3.8 shows SEM images of resulting Au nanostructures obtained from the above treatments. When L-Cys was used separately prior to HAuCl₄ (Figure 3.8a), the resulting Au nanostructures appeared to be similar in size and density to those obtained without L-cys additive (Figure 3.2a). On the other hand, when L-Cys was used separately, followed by mixture of HAuCl₄ and L-Cys, we observed larger and elongated Au nanostructures (Figure 3.8b). When CTAB was used separately prior to HAuCl₄ (Figure 3.8c), we observed significant reduction in density and increase in size of Au nanostructures, which were opposite to those observed when only mixture of HAuCl₄ and CTAB was used (Figure 3.5a). When mixture of HAuCl₄ and CTAB was used, following a separate CTAB treatment step, we observed a noticeable increase in Au nanostructure density and a slight increase in size (Figure 3.8d). Nevertheless, even in this case, the density was still considerably lower than what was observed in Figure 3.5a.

Based on the preceding results, we proposed the following explanation. When L-Cys, a zwitterionic surfactant, was used, adsorption to Si substrate was very weak. When Si substrate was directly transferred from L-Cys solution to the deposition solution, some small amount of L-Cys remained adsorbed on the surface. Since the adsorption was very weak, L-Cys would quickly enter the deposition solution rather than remain adsorbed to the Si surface. That explained the similar outcomes observed in Figure 3.8a and Figure 3.2a. The

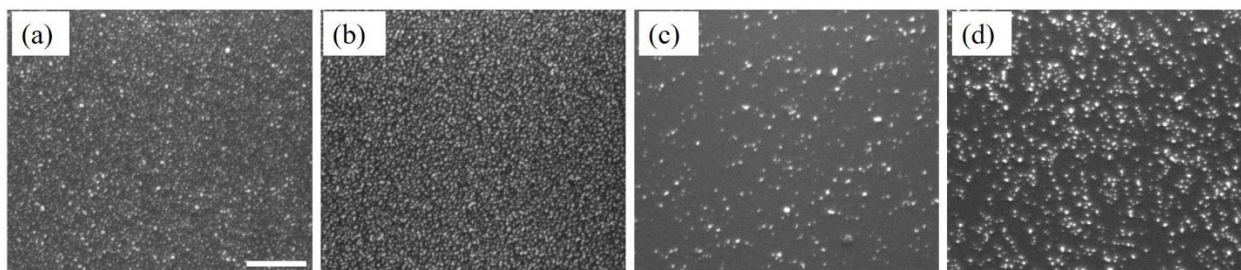


Figure 3.8 SEM images of Au nanostructures deposited on Si substrate after sequential exposure to (a) L-Cys then HAuCl₄, (b) L-Cys then mixture of HAuCl₄ and L-Cys, (c) CTAB then HAuCl₄, and (d) CTAB then mixture of HAuCl₄ and CTAB. The scale bar is 500 nm

situation in Figure 3.8b was slightly different because the deposition solution contained metal ion-cysteine complexes that were readily reduced to Au (0). Aided by additional L-Cys from the preceding L-Cys solution, Au nanostructures in this case would eventually grow larger and denser. In contrast, CTAB was able to bind more strongly to Si substrate due to electrostatic attraction between protonated hydroxylated Si surface and the bromide counterion.^{25,26} Thus, upon exposed to CTAB solution prior to deposition, a significant portion of Si surface was adsorbed by CTAB, hindering metallic deposition. That explained the low density observed in Figure 3.8c and Figure 3.8d. When fewer sites were available for deposition, the size of the resulting Au nanostructures would be larger. The blocking of deposition sites did not occur when CTAB was mixed with HAuCl₄ prior to deposition, due to the binding between them (Figure 3.5a). Hence, depending on the kind of surfactant used,

the effect of surfactant adsorption to Si substrate on overall Au nanostructure deposition would vary.

Figure 3.9 shows topographical images of Au samples after one, three, and five deposition cycles as measured using the AFM. It can be observed that increasing the number of deposition cycles resulted in Au nanostructures with increasing height and lateral size, thus, supporting the SEM results. When surfactants were added, they alleviated aggregation and agglomeration, as indicated by smoother surfaces. Figure 3.11 shows the root mean square (RMS) roughness values for the prepared samples. It can be observed that increasing the number of deposition cycles (from 1X to 5X) increased the surface roughness of the samples due to the increasing size of the Au nanostructures. The data confirms the visual observations from the SEM images regarding the role of surfactants in reducing aggregation and agglomeration, thereby leading to a more homogeneous surface by L-Cysteine, followed by CTAB.

Along with the measurement of number density, size and size distribution, the absorption properties of Au nanoparticle deposited during the first deposition cycle were analyzed in detail. Figure 3.10 shows the UV-Vis absorption spectra for Au nanoparticles deposited in the absence and presence of either L-Cys or CTAB. The surface plasmon resonance (SPR) for gold appears in the range of 500 – 600 nm and is attributed to the transverse plasmon mode⁴⁶. The UV-Vis for Au nanoparticles in the absence of surfactants shows a broad spectrum with two maxima. The two maxima are centered approximately at 532 nm and 610 nm, confirming the formation of Au and indicating the presence of at least

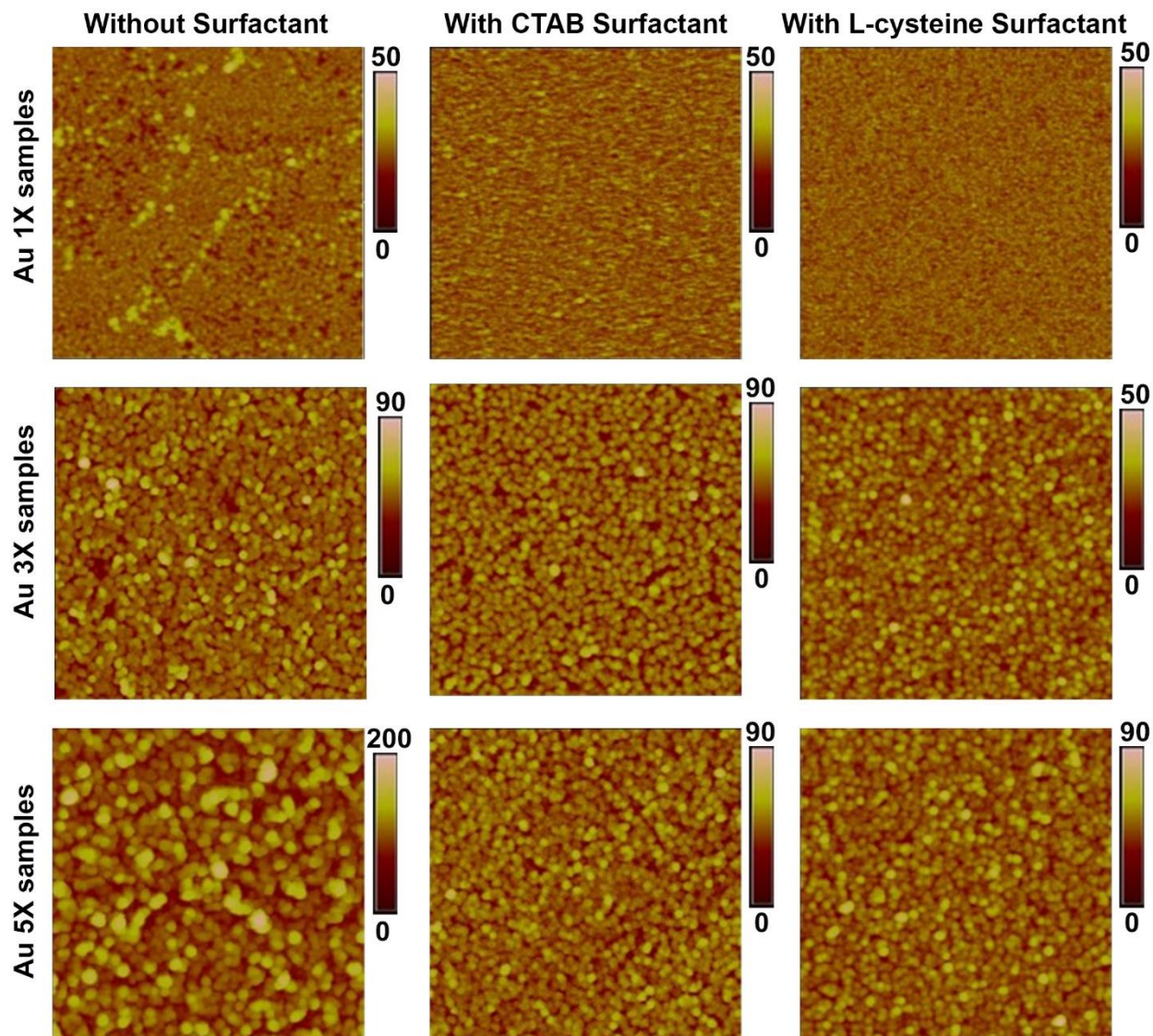


Figure 3.9 Representative AFM topography maps of the Au samples after one (1X), three (3X), and five (5X) deposition cycles. Scan size of $2\ \mu\text{m} \times 2\ \mu\text{m}$. Height scale is in nm.

two nanoparticle sizes in the Au sample. The UV-Vis spectra for other Au nanoparticles deposited in the presence of surfactants like L-Cys and CTAB indicate a narrower line width with a single maximum at 532 nm. The comparison of UV-Vis absorption spectra indicates that the Au nanoparticles deposited in the absence of surfactants are polydispersed, whereas the Au nanoparticles deposited in the presence of surfactants are monodispersed. The

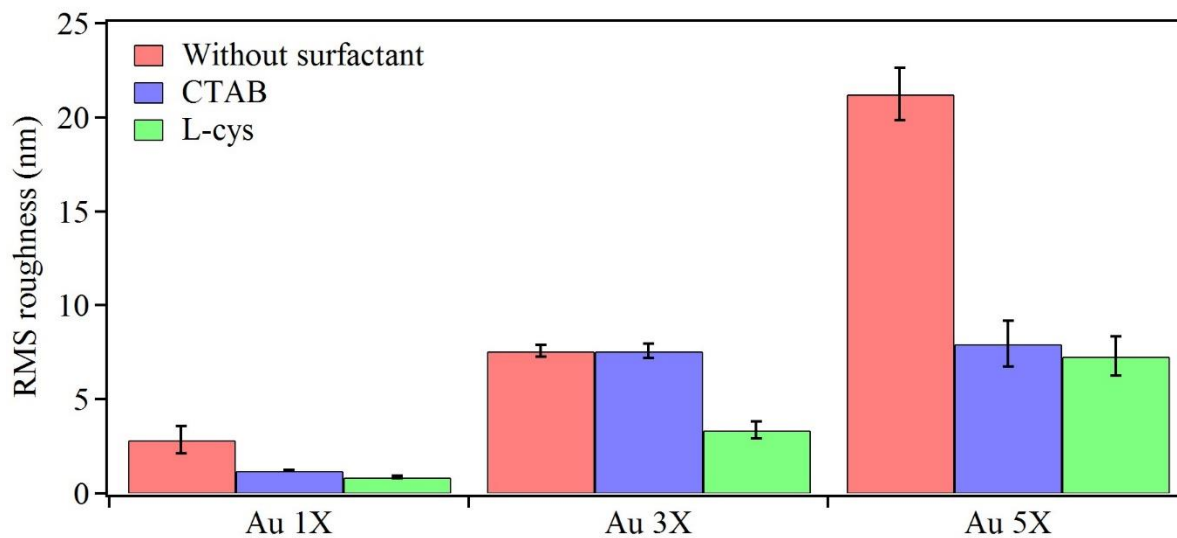


Figure 3.11 *RMS roughness of Au samples after one (1X), three (3X), and five (5X) deposition cycles. Mean values from five different locations on each sample are shown. Error bars represent 95% confidence intervals.*

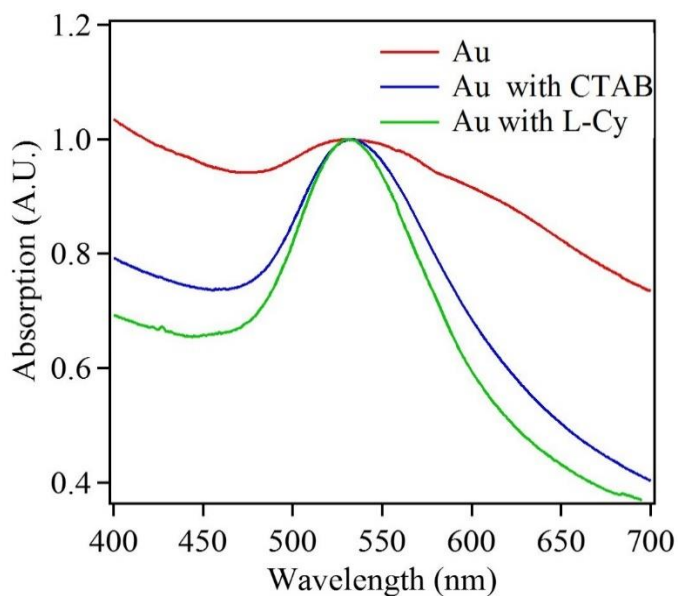


Figure 3.10 *Absorption spectra of Au nanoparticles after the first deposition cycle in the absence and presence of surfactants.*

nanoparticle dispersity is confirmed from the SEM images of these Au samples shown in Figure 3.2a, Figure 3.4a and Figure 3.5a.

Further, UV-Vis absorption spectra were recorded for all Au samples prepared in the absence and presence of surfactants, from one deposition cycle to five deposition cycles. With increase in deposition cycles, the absorption maximum essentially red-shifted, and the line width of the absorption spectrum increased. The red-shift of the absorption maximum and the peak broadening have been described in the literature as a result of the increase in Au nanostructure size, due to increasing aggregation, and the decrease in distance between these nanostructures, resulting in increased interparticle plasmon coupling. In addition, the overall trend of increasing absorption line width indicates that the nanoparticle dispersity increased with increase in the number of deposition cycles. This inference is supported by the virtue of the deposition process. At every deposition cycle, nucleation and growth of new nanoparticles occurred and thus there was a high possibility of polydispersity with increase in deposition cycles. Figure A 3.3 and Table A 3.1, in supporting information, shows the UV-Vis spectra and the corresponding absorption maxima, respectively, of Au samples in the absence and presence of surfactants.

The Cu-based nanostructures were characterized by XPS. Figure 3.12 shows XPS spectra and an AES spectrum of Cu-based nanostructures. The broad peak of Cu 2p^{3/2} in Figure 3.12a was composed of two peaks with maxima at 932.9 and 934.9 eV. Two Gaussian curves were fitted to this broad peak of Cu 2p^{3/2} as shown in Figure 3.12a. Similarly, a broad peak of Cu 2p^{1/2} was composed of two peaks at 952.2 and 954.7 eV. Additionally, two strong Cu²⁺ satellite peaks were observed in the XPS spectrum. The presence of Cu 2p^{3/2} (934.9 eV), Cu 2p^{1/2} (954.7 eV) and satellite peaks indicate the presence of Cu(OH)₂ on the surface of the Cu-based sample.^{49,50} Furthermore, while Cu 2p_{1/2} and Cu 2p_{3/2} peaks at 952.2 and 932.9 eV, respectively, can confirm the presence of metallic Cu, they may imply the presence of Cu₂O

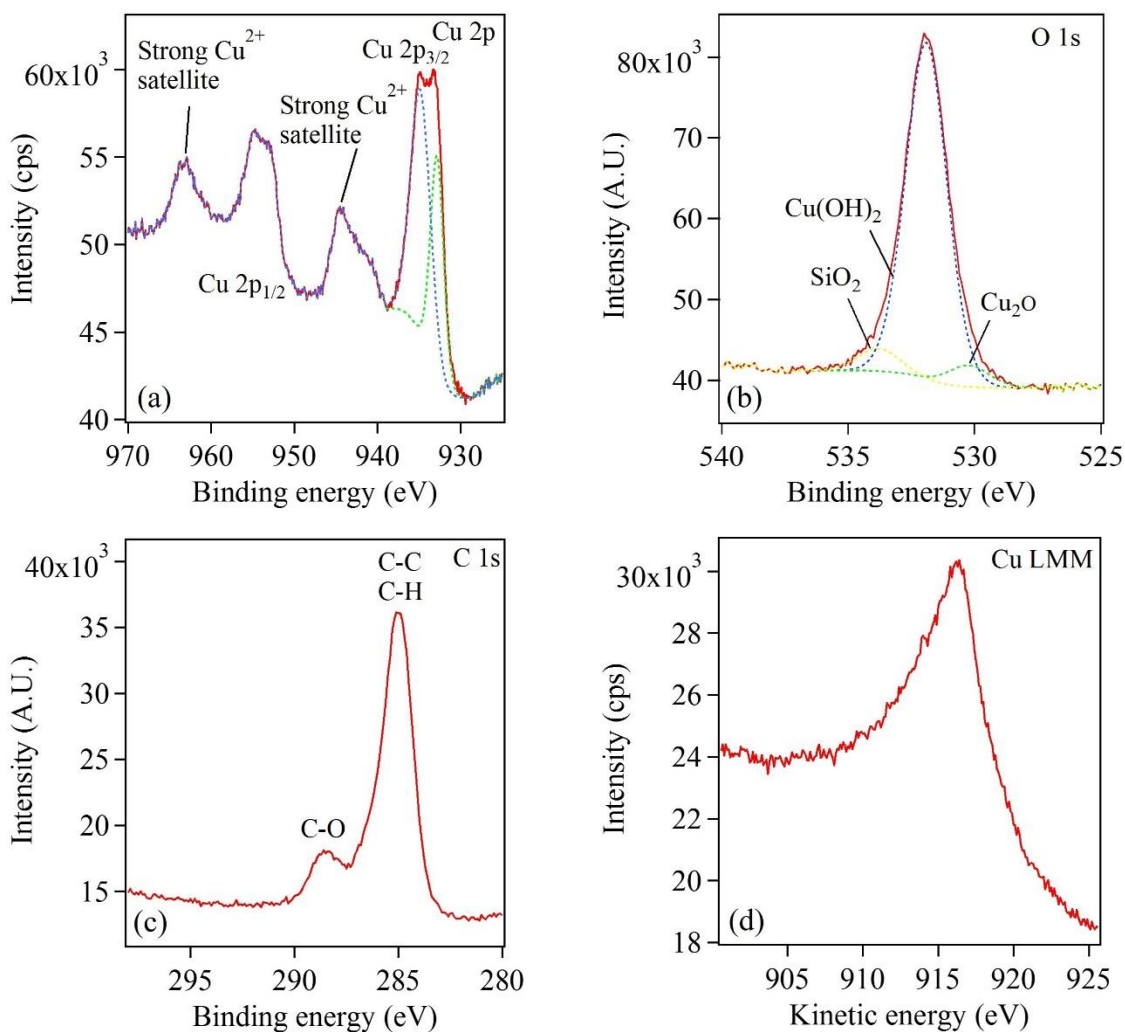


Figure 3.12 XPS spectra showing (a) Cu 2p peaks corresponding to different oxidation states of Cu, (b) O 1s peaks corresponding to different oxide species, and (c) C 1s peaks corresponding to various carbon bonds (d) AES spectrum showing Cu LMM peak resembling that of Cu(OH)₂ and Cu₂O. The dashed curves in (a) and (b) represent fitted Gaussian curves

as well, because Cu 2p peaks of Cu and Cu₂O are indistinguishable.^{49,50} An AES spectrum (Figure 3.12d) was obtained for the Cu-based sample to further elucidate the chemical composition of Cu-based sample.⁵⁰⁻⁵² A broad Cu LMM peak centered at 916.4 eV was observed in the AES spectrum. This broad peak can be attributed to an overlap of two peaks with maxima at 916.3 and 916.7 eV, which correspond to the presence of Cu(OH)₂ and Cu₂O respectively.^{51,52}

Further, the location of the O 1s peak was analyzed to study the nature of the oxide species. Figure 3.12b shows a broad peak that is composed of three peaks at 530.3, 531.9, and 533.8 eV, which represent characteristic oxides of Cu_2O , $\text{Cu}(\text{OH})_2$, and SiO_2 , respectively.⁵³ Figure 3.12c provides information on surface adsorbed species. The strong peak at 285.1 eV can be matched with C-C and C-H bonds and peak at 288.6 eV can be assigned to C-O bond, which arise from surface contaminants.^{53,54} It is also important to note that XPS and AES are surface characterization techniques and thus divulge surface information of samples with good precision. Thus from the XRD (Supplementary information Figure A 3.4), XPS and AES characterization of Cu-based nanostructures, it can be inferred that the Cu-based sample was composed of a metallic Cu core with a Cu_2O and $\text{Cu}(\text{OH})_2$ outer layer. Similar systems of copper core and very thin copper oxide shell have also been described in the literature⁵⁵⁻⁵⁶.

Finally, to evaluate scattering properties of the deposited Au and Cu nanostructures, Raman spectroscopy measurements were performed to determine their applicability for SERS. Au has been the material of choice for SERS due to its stability, biocompatibility, and easy surface treatment.⁵⁷ While charge transfer between adsorbed molecules and the metal substrate also contributes to the enhancement, the effect of localized surface plasmon resonance by the presence of Au nanostructures is an exclusively dominating mechanism.^{58,59} Figure 3.13 shows Raman spectra of R6G dye upon drop casting onto Au nanostructure substrates with 5, 8, and 10 deposition cycles. For comparison, the same amount of R6G was also drop cast onto bare Si substrate without Au deposition. When only bare Si was used as the substrate, no Raman signal was detected. On the other hand, several strong Raman peaks were observed when the substrate was deposited with Au nanostructures after ten deposition

cycles (Au/Si 10X). These peaks can be identified as those resulting from different molecular vibrational modes of R6G. Table 3.2 provides detailed assignment for every peak in Figure 3.13 according to published data. As the number of deposition cycles decreased to 8X and 5X, those Raman peaks of R6G were still clearly seen. However, their intensities decreased respectively. Since under similar experimental conditions, Raman signals from R6G were only observed for substrates with Au nanostructures, it was reasonable to conclude that Au nanostructures enhanced Raman scattering of the dye molecules adsorbed on them. Raman peaks from R6G were also observed for Cu nanostructures although their intensities were much weaker at higher R6G concentration (Figure 3.14). Figure 3.15 shows Raman spectra of R6G at two different concentrations. At as low concentration as 10^{-6} M, although some peaks were missing, it was still possible to detect R6G because the most prominent Raman peaks were still clearly visible, indicating that our substrates can still be useful in applications that require detection of very low analyte concentrations. In the next set of SERS experiments, paraoxon was used as probe molecule. Paraoxon is an organophosphorous compound and one of the most hazardous pesticides. Thus, only a trace amount of this compound in the environment can cause serious health problem.⁶⁰ SERS is a simple and fast method with excellent sensitivity for paraoxon detection. Figure 3.16 shows Raman spectrum of 10^{-2} M paraoxon adsorbing on Au nanostructures. The four strongest fingerprint peaks representing different vibrational modes of paraoxon molecules were clearly seen in these spectra.^{61,62} Raman scattering was certainly enhanced by the metallic nanostructures because none of these peaks was observed when bare Si was used as SERS substrate.

One way to quantitatively determine the effectiveness of SERS substrate is to calculate the enhancement factor (EF). The most widely used definition of the EF is described as

$$EF = \frac{I_{SERS}/C_{SERS}}{I_{RS}/C_{RS}}$$

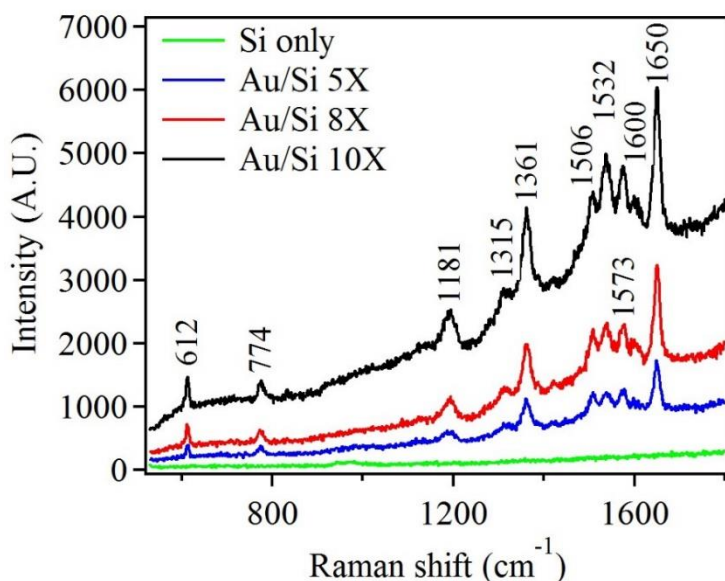


Figure 3.13 Raman spectra of R6G adsorbed on bare Si, and Si deposited with Au nanostructures after five, eight, and ten deposition cycles. The R6G concentration was 10^{-5} M.

where I_{SERS} and I_{RS} are Raman intensities of SERS and non-SERS substrates, respectively, while C_{SERS} and C_{RS} are analyte concentrations used for SERS and non-SERS substrates, respectively.⁶³ In our case, we used the same R6G concentrations for both Au/Si and bare Si substrates. Thus, EF was simply a ratio of I_{SERS} and I_{RS} . However, since Raman signal obtained from bare Si substrate (I_{RS}) was too weak to be detected by our instrument, it was not possible to obtain absolute values for EF. Instead, we only roughly estimated EFs in a manner similar to those reported by Yamamoto et al.⁵⁹ Thus, EF values for SERS substrates

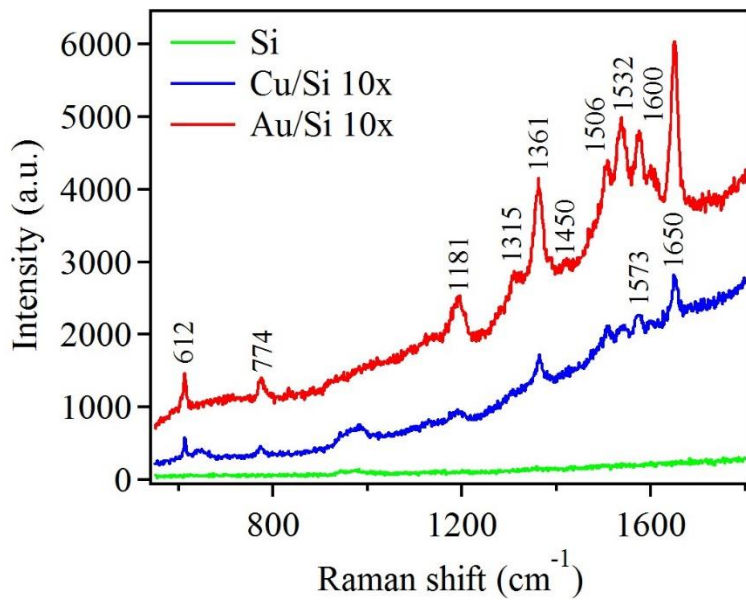


Figure 3.14 Raman spectra of R6G adsorbed on bare Si, and Si deposited with Au and Cu nanostructures after ten deposition cycles. The R6G concentrations were 10^{-4} M for bare Si and Cu/Si, and 10^{-5} M for Au/Si.

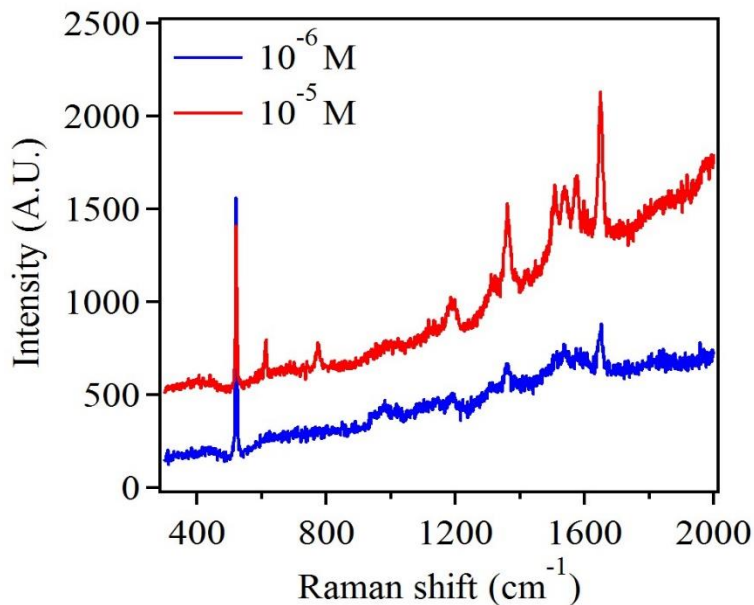


Figure 3.15 Raman spectra of R6G at two different concentrations drop cast onto Si deposited with Au nanostructures after five deposition cycles.

Table 3.2 Raman peak assignments for R6G dye and paraoxon

Peak position (cm ⁻¹)	Assignment for R6G	Reference
612	In-plane bending of C-C-C ring	64, 65, 66
774	C-H out-of-plane bending	59, 64, 65, 66
1181	In-plane xanthene ring deformation, C-H bending, N-H bending	59, 64, 65, 66
1315	Aromatic C-C stretching	64, 65
1361	Aromatic C-C stretching, in-plane C-H bending	59, 64, 65, 66
1450		65
1506	Aromatic C-C stretching, C-N stretching, C-H bending, N-H bending	59, 64, 65
1532		65
1573	Aromatic C-C stretching, in-plane N-H bending	59, 64, 65
1600		59, 64, 65
1650	Aromatic C-C stretching, in-plane C-H bending	59, 64, 65, 66
Peak position (cm ⁻¹)	Assignment for paraoxon	Reference
857	NO ₂ scissor (Aromatic -NO ₂)	61, 62
1110	C-H band (in plane)/NO ₂ asymmetric stretching	61, 62
1348	Symmetry stretching NO ₂	61, 62
1592	Phenyl ring vibration	61, 62

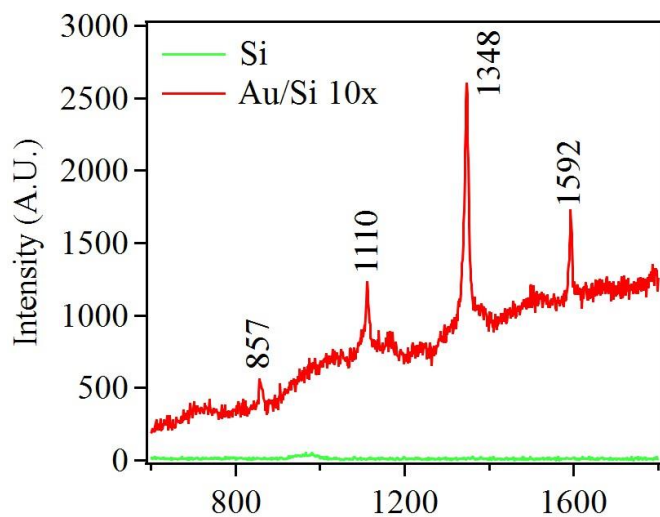


Figure 3.16 Raman spectrum of 10-2 M paraoxon adsorbed on Au nanostructures deposited on Si substrate after ten deposition cycles. Raman spectrum of paraoxon adsorbed on bare Si substrate is shown for comparison.

with Au nanostructures deposited for five, eight, and ten cycles were $\sim 0.8 \times 10^3$, $\sim 1.5 \times 10^3$, and $\sim 2 \times 10^3$, respectively, when 10^{-5} M R6G was used. Similarly, EF value for SERS substrate with Cu nanostructures deposited for ten cycles was $\sim 0.5 \times 10^3$ when 10^{-4} M R6G was used. For paraoxon, we estimated that the EF value would reach $\sim 1.5 \times 10^3$ when 10^{-2} M paraoxon was used. The important factor that led to the SERS properties of our substrates was the dense coverage of Au nanostructures as observed in Figure 3.2, and the SERS effect was proportional to the density as shown in Figure 3.13. In addition, the chains of nanoparticles, which formed a continuous network, created numerous crevices to concentrate light. Likewise, denser coverage narrowed the gaps between nanostructures, therefore created several additional “hot spots” for light amplification.⁵⁸

Conclusion

In summary, this report presents a modification of the electroless deposition method. Here the Au and Cu-based nanostructures were deposited on n-type Si (100) substrate using limited HF exposure. The density of the nanostructures was controlled by varying the deposition cycles. The density and size of the nanostructures was controlled by the incorporation of surfactants like L-Cys and CTAB in the deposition process. The presence of surfactants produced monodispersed, highly dense quantum sized nanoparticles in the first deposition cycle. As the number of deposition cycles increased there was morphological evolution in Au and Cu-based samples to form a more connected network of nanostructures. The UV-Vis absorption indicated the presence of monodispersed Au nanostructures. The XPS and XRD data indicated the presence of a Cu core and Cu_2O or $\text{Cu}(\text{OH})_2$ shell. The Raman measurements demonstrated enhancement for both Au and Cu-based samples compared to the Si substrate.

References

1. Carraro, C.; Maboudian, R.; Magagnin, L., Metallization and nanostructuring of semiconductor surfaces by galvanic displacement processes. *Surface Science Reports* 2007, 62 (12), 499-525.
2. Ali, H. O.; Christie, I. R. A., A review of electroless gold deposition processes. *Gold Bulletin* 1984, 17 (4), 118-127.
3. Gutés, A.; Carraro, C.; Maboudian, R., Ultrasooth Gold Thin Films by Self-Limiting Galvanic Displacement on Silicon. *ACS Applied Materials & Interfaces* 2011, 3 (5), 1581-1584.
4. Sayed, S. Y.; Buriak, J. M., Epitaxial Growth of Nanostructured Gold Films on Germanium via Galvanic Displacement. *ACS Applied Materials & Interfaces* 2010, 2 (12), 3515-3524.
5. Darosa, C. I., E.; Maboudian, R., Dynamics of Copper Deposition onto Silicon by Galvanic Displacement. *J. Electrochem. Soc.* 2008, 155 (3), 6.
6. Yae, S.; Nasu, N.; Matsumoto, K.; Hagihara, T.; Fukumuro, N.; Matsuda, H., Nucleation behavior in electroless displacement deposition of metals on silicon from hydrofluoric acid solutions. *Electrochimica Acta* 2007, 53 (1), 35-41.

7. Warren, S.; Reitzle, A.; Kazimirov, A.; Ziegler, J. C.; Bunk, O.; Cao, L. X.; Renner, F. U.; Kolb, D. M.; Bedzyk, M. J.; Zegenhagen, J., A structure study of the electroless deposition of Au on Si(1 1 1):H. *Surface Science* 2002, 496 (3), 287-298.
8. Peng, K.; Zhu, J., Morphological selection of electroless metal deposits on silicon in aqueous fluoride solution. *Electrochimica Acta* 2004, 49 (16), 2563-2568.
9. Magagnin, L.; Maboudian, R.; Carraro, C., Gold Deposition by Galvanic Displacement on Semiconductor Surfaces: Effect of Substrate on Adhesion. *The Journal of Physical Chemistry B* 2002, 106 (2), 401-407.
10. Zhang, X.; Qiao, Y.; Xu, L.; Buriak, J. M., Constructing Metal-Based Structures on Nanopatterned Etched Silicon. *ACS Nano* 2011, 5 (6), 5015-5024.
11. Aizawa, M.; Buriak, J. M., Nanoscale Patterning of Two Metals on Silicon Surfaces Using an ABC Triblock Copolymer Template. *Journal of the American Chemical Society* 2006, 128 (17), 5877-5886.
12. Fabre, B.; Hennous, L.; Ababou-Girard, S.; Meriadec, C., Electroless Patterned Assembly of Metal Nanoparticles on Hydrogen-Terminated Silicon Surfaces for Applications in Photoelectrocatalysis. *ACS Applied Materials & Interfaces* 2013, 5 (2), 338-343.

13. Gorostiza, P.; Allongue, P.; Díaz, R.; Morante, J. R.; Sanz, F., Electrochemical Characterization of the Open-Circuit Deposition of Platinum on Silicon from Fluoride Solutions. *The Journal of Physical Chemistry B* 2003, *107* (26), 6454-6461.
14. Zhang, Y.; Ang, S. S.; Tay, A. A. O.; Xu, D.; Kang, E. T.; Neoh, K. G.; Chong, L. P.; Huan, A. C. H., Characterization of Electrolessly Deposited Copper and Nickel Nanofilms on Modified Si(100) Surface. *Langmuir* 2003, *19* (17), 6802-6806.
15. Cho, J. S. H.; Kang, H.-K.; Wong, S. S.; Shacham-Diamand, Y., Electroless Cu for VLSI. *MRS Bulletin* 1993, *18* (6), 31-38.
16. Scheck, C.; Liu, Y.-K.; Evans, P.; Schad, R.; Bowers, A.; Zangari, G.; Williams, J. R.; Issacs-Smith, T. F., Photoexcited electrodeposition of Cu structures on p-Si(001). *Journal of Vacuum Science & Technology A* 2004, *22* (4), 1842-1846.
17. Lim, S. M., R.; Pianetta, P.; Chidsey, C. , Effect of Silicon Surface Termination on Copper Deposition in Deionized Water. *Journal of the Electrochemical Society* 2001, , *148* (1), 4.
18. Porter, L. A.; Choi, H. C.; Schmeltzer, J. M.; Ribbe, A. E.; Elliott, L. C. C.; Buriak, J. M., Electroless Nanoparticle Film Deposition Compatible with Photolithography, Microcontact Printing, and Dip-Pen Nanolithography Patterning Technologies. *Nano Letters* 2002, *2* (12), 1369-1372.

19. Yang, X.; Zhong, H.; Zhu, Y.; Shen, J.; Li, C., Ultrasensitive and recyclable SERS substrate based on Au-decorated Si nanowire arrays. *Dalton Transactions* 2013, 42 (39), 14324-14330.
20. Lahiri, A.; Wen, R.; Kuimalee, S.; Kobayashi, S.-i.; Park, H., One-step growth of needle and dendritic gold nanostructures on silicon for surface enhanced Raman scattering. *CrystEngComm* 2012, 14 (4), 1241-1246.
21. Blackwood, D. J.; Khoo, S. M., Electroless plating of noble metal nanoparticles for improved performance of silicon photodiodes via surface plasmon resonance. *Solar Energy Materials and Solar Cells* 2010, 94 (7), 1201-1206.
22. Yu, P.; Chiu, C. H.; Wu, Y.-R.; Yen, H. H.; Chen, J. R.; Kao, C. C.; Yang, H.-W.; Kuo, H. C.; Lu, T. C.; Yeh, W. Y.; Wang, S. C., Strain relaxation induced microphotoluminescence characteristics of a single InGaN-based nanopillar fabricated by focused ion beam milling. *Applied Physics Letters* 2008, 93 (8), 081110.
23. Kye, J.; Shin, M.; Lim, B.; Jang, J.-W.; Oh, I.; Hwang, S., Platinum Monolayer Electrocatalyst on Gold Nanostructures on Silicon for Photoelectrochemical Hydrogen Evolution. *ACS Nano* 2013, 7 (7), 6017-6023.

24. R. Rosenberg; D. C. Edelstein; C.-K. Hu, a.; Rodbell, K. P., Copper Metallization for High Performance Silicon Technology. *Annual Review of Materials Science* 2000, 30 (1), 229-262.
25. Pai, P. L.; Ting, C. H., Selective electroless copper for VLSI interconnection. *IEEE Electron Device Letters* 1989, 10 (9), 423-425.
26. Peng, Z.; Hu, H.; Utama, M. I. B.; Wong, L. M.; Ghosh, K.; Chen, R.; Wang, S.; Shen, Z.; Xiong, Q., Heteroepitaxial Decoration of Ag Nanoparticles on Si Nanowires: A Case Study on Raman Scattering and Mapping. *Nano Letters* 2010, 10 (10), 3940-3947.
27. Chen, R.; Li, D.; Hu, H.; Zhao, Y.; Wang, Y.; Wong, N.; Wang, S.; Zhang, Y.; Hu, J.; Shen, Z.; Xiong, Q., Tailoring Optical Properties of Silicon Nanowires by Au Nanostructure Decorations: Enhanced Raman Scattering and Photodetection. *The Journal of Physical Chemistry C* 2012, 116 (7), 4416-4422.
28. Li, M.; Sui, M.; Pandey, P.; Zhang, Q.; Kim, E.; Lee, J. *Nanoscale Research Letters* 2015, 10, 1-14.
29. Vitos, L.; Ruban, A. V.; Skriver, H. L.; Kollár, J., The surface energy of metals. *Surface Science* 1998, 411 (1-2), 186-202.
30. Grzelczak, M.; Perez-Juste, J.; Mulvaney, P.; Liz-Marzan, L. M., Shape control in gold nanoparticle synthesis. *Chemical Society Reviews* 2008, 37 (9), 1783-1791.

31. Love, J. C.; Estroff, L. A.; Kriebel, J. K.; Nuzzo, R. G.; Whitesides, G. M., Self-Assembled Monolayers of Thiolates on Metals as a Form of Nanotechnology. *Chemical Reviews* 2005, *105* (4), 1103-1170.
32. Padalkar, S.; Capadona, J. R.; Rowan, S. J.; Weder, C.; Won, Y.-H.; Stanciu, L. A.; Moon, R. J., Natural Biopolymers: Novel Templates for the Synthesis of Nanostructures. *Langmuir* 2010, *26* (11), 8497-8502.
33. Padalkar, S.; Capadona, J. R.; Rowan, S. J.; Weder, C.; Moon, R. J.; Stanciu, L. A., Self-assembly and alignment of semiconductor nanoparticles on cellulose nanocrystals. *Journal of Materials Science* 2011, *46* (17), 5672-5679.
34. Zhang, W.-W.; Lu, C.-S.; Zou, Y.; Xie, J.-L.; Ren, X.-M.; Zhu, H.-Z.; Meng, Q.-J., Self-Assembly of L-Cysteine-Copper(II)/Copper(I) Multilayer Thin Films on Gold. *Journal of Colloid and Interface Science* 2002, *249* (2), 301-306.
35. Sakai, N.; Fujiwara, Y.; Arai, M.; Yu, K.; Tatsuma, T., Electrodeposition of gold nanoparticles on ITO: Control of morphology and plasmon resonance-based absorption and scattering. *Journal of Electroanalytical Chemistry* 2009, *628* (1–2), 7-15.
36. Bhanushali, S.; Ghosh, P.; Ganesh, A.; Cheng, W. L., 1D Copper Nanostructures: Progress, Challenges and Opportunities. *Small* 2015, *11* (11), 1232-1252.

37. Nikoobakht, B.; El-Sayed, M. A., Evidence for Bilayer Assembly of Cationic Surfactants on the Surface of Gold Nanorods. *Langmuir* 2001, *17* (20), 6368-6374.
38. Brust, M.; Blass, P. M.; Bard, A. J., Self-Assembly of Photoluminescent Copper(I)-Dithiol Multilayer Thin Films and Bulk Materials. *Langmuir* 1997, *13* (21), 5602-5607.
39. Li, B.; Xie, Y.; Xue, Y., Controllable Synthesis of CuS Nanostructures from Self-Assembled Precursors with Biomolecule Assistance. *The Journal of Physical Chemistry C* 2007, *111* (33), 12181-12187.
40. Briñas, R. P.; Hu, M.; Qian, L.; Lyman, E. S.; Hainfeld, J. F., Gold Nanoparticle Size Controlled by Polymeric Au(I) Thiolate Precursor Size. *Journal of the American Chemical Society* 2008, *130* (3), 975-982.
41. Bunton, C. A.; Nome, F.; Quina, F. H.; Romsted, L. S., Ion binding and reactivity at charged aqueous interfaces. *Accounts of Chemical Research* 1991, *24* (12), 357-364.
42. Tang, J.; Huang, J.; Man, S.-Q., Preparation of gold nanoparticles by surfactant-promoted reductive reaction without extra reducing agent. *Spectrochimica Acta Part A: Molecular and Biomolecular Spectroscopy* 2013, *103*, 349-355.

43. Min, Z.; Baoxiang, W.; Zbigniew, R.; Zhaohui, X.; Jon Otto, F.; Xiaofeng, Y.; Steinar, R., Minute synthesis of extremely stable gold nanoparticles. *Nanotechnology* 2009, *20* (50), 505606.
44. Roman, P.; Hwang, D.; Torek, K.; Ruzylo, J.; Kamieniecki, E.; Liehr, M.; Heyns, M.; Hirose, M.; Parks, H. *Ultraclean Semiconductor Processing Technology and Surface Chemical Cleaning and Passivation* **1995**, 386, 401-406.
45. Tummala, N.; Shi, L.; Striolo, A. *Journal of Colloid and Interface Science* **2011**, 362 (1), 135-143.
46. Link, S.; El-Sayed, M. A., Spectral Properties and Relaxation Dynamics of Surface Plasmon Electronic Oscillations in Gold and Silver Nanodots and Nanorods. *The Journal of Physical Chemistry B* 1999, *103* (40), 8410-8426.
47. Brinson, B.; Lassiter, J.; Levin, C.; Bardhan, R.; Mirin, N.; Halas, N. *Langmuir* **2008**, *24* (24), 14166-14171.
48. Ghosh, S.; Pal, T. *Chemical Reviews* **2007**, *107* (11), 4797-4862.
49. Biesinger, M.; Lau, L.; Gerson, A.; Smart, R. *Applied Surface Science* **2010**, *257* (3), 887-898.

50. McIntyre, N. S.; Cook, M. G. *Analytical Chemistry* **1975**, *47* (13), 2208-2213.
51. McIntyre, N. S.; Sunder, S.; Shoesmith, D. W.; Stanchell, F. W. *Journal of Vacuum Science & Technology* **1981**, *18* (3), 714-721.
52. Ma, Q.; Hofmann, J.; Litke, A.; Hensen, E. *Solar Energy Materials and Solar Cells* **2015**, *141*, 178-186.
53. Chavez, K.; Hess, D. *Journal of the Electrochemical Society* **2001**, *148* (11), G640-G643.
54. Baklanov, M.; Shamiryan, D.; Tokei, Z.; Beyer, G.; Conard, T.; Vanhaelemeersch, S.; Maex, K. *Journal of Vacuum Science & Technology B* **2001**, *19* (4), 1201-1211.
55. Sudipa, P.; Subrata, K.; Soumen, B.; Snigdhamayee, P.; Subhra, J.; Surojit, P.; Sujit Kumar, G.; Anjali, P.; Tarasankar, P., Cysteine functionalized copper organosol: synthesis, characterization and catalytic application. *Nanotechnology* 2006, *17* (21), 5461.
56. Biçer, M.; Şişman, İ., Controlled synthesis of copper nano/microstructures using ascorbic acid in aqueous CTAB solution. *Powder Technology* 2010, *198* (2), 279-284.

57. Israelsen, N. D.; Hanson, C.; Vargis, E., Nanoparticle properties and synthesis effects on surface-enhanced Raman scattering enhancement factor: an introduction. *The Scientific World Journal* 2015, 2015, 124582-124582.
58. Sharma, B.; Frontiera, R.; Henry, A.; Ringe, E.; Van Duyne, R. *Materials Today* **2012**, 15 (1-2), 16-25.
59. Yamamoto, Y.; Hasegawa, K.; Hasegawa, Y.; Takahashi, N.; Kitahama, Y.; Fukuoka, S.; Murase, N.; Baba, Y.; Ozaki, Y.; Itoh, T. *Physical Chemistry Chemical Physics* **2013**, 15 (35), 14611-14615.
60. Aragay, G.; Pino, F.; Merkoci, A. *Chemical Reviews* **2012**, 112 (10), 5317-5338.
61. Wang, B.; Zhang, L.; Zhou, X. *Spectrochimica Acta Part a-Molecular and Biomolecular Spectroscopy* **2014**, 121, 63-69.
62. Li, P.; Dong, R.; Wu, Y.; Liu, H.; Kong, L.; Yang, L. *Talanta* **2014**, 127, 269-275.
63. Le Ru, E.; Blackie, E.; Meyer, M.; Etchegoin, P. *Journal of Physical Chemistry C* **2007**, 111 (37), 13794-13803.

64. He, X.; Gao, Y.; Mahjouri-Samani, M.; Black, P.; Allen, J.; Mitchell, M.; Xiong, W.; Zhou, Y.; Jiang, L.; Lu, Y. *Nanotechnology* **2012**, *23* (20).
65. Hildebrandt, P.; Stockburger, M. *Journal of Physical Chemistry* **1984**, *88* (24), 5935-5944.
66. Zhang, Y.; Zheng, J.; Gao, G.; Kong, Y.; Zhi, X.; Wang, K.; Zhang, X.; Cui, D. *International Journal of Nanomedicine* **2011**, *6*, 2899-2906.
67. Nalawade, P.; Mukherjee, T.; Kapoor, S. *Advances in Nanoparticles* **2013**, *2*, 78-86.
68. Wu, S.; Chen, D. *Journal of Colloid and Interface Science* **2004**, *273* (1), 165-169.
69. Panigrahi, S.; Kundu, S.; Basu, S.; Praharaj, S.; Jana, S.; Pande, S.; Ghosh, S.; Pal, A.; Pal, T. *Nanotechnology* **2006**, *17* (21), 5461-5468.
70. Lam, Y.; Zheng, H.; Tjeung, R.; Chen, X. *Journal of Physics D-Applied Physics* **2009**, *42* (4).

Appendix

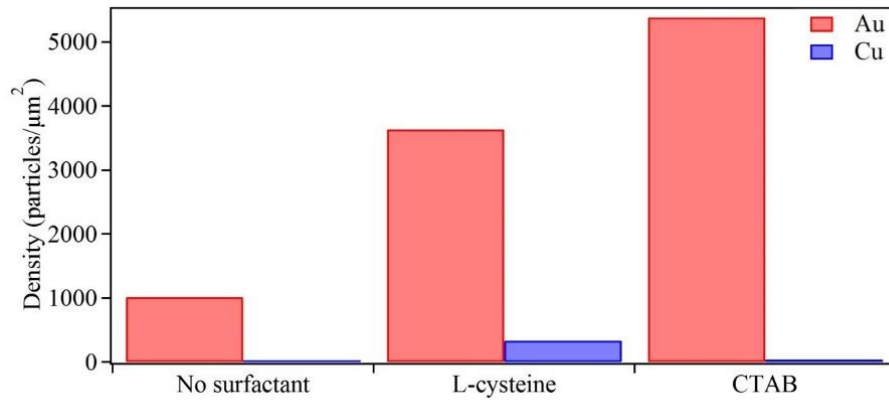


Figure A 3.1 The number densities of Au and Cu-based nanoparticles with and without surfactant after one deposition cycle.

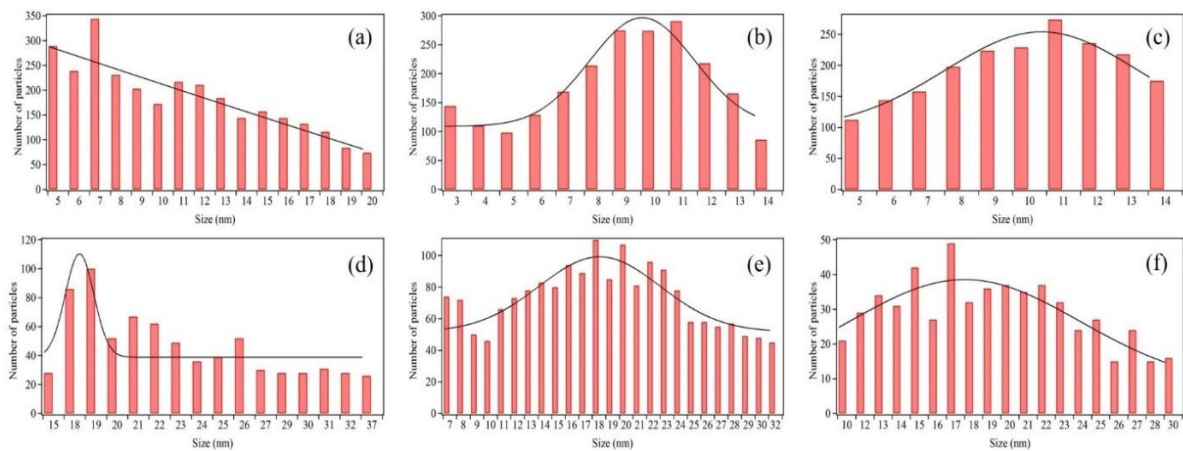


Figure A 3.2 Size distribution with Gaussian curve fitting of Au nanoparticles (a) without surfactant, (b) with L-cysteine, and (c) with CTAB, and Cu-based nanoparticles (d) without surfactant, (e) with L-cysteine, and (f) with CTAB after one deposition cycle. The distribution was constructed based on (a) 2941, (b) 2174, (c) 1968, (d) 742, (e) 1823, and (f) 563 particles.

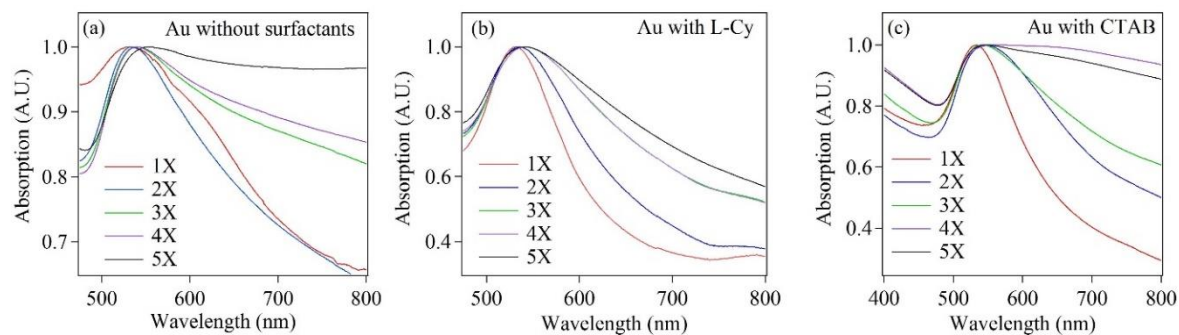


Figure A 3.3 UV-Vis spectra of Au samples without surfactants (a), with L-Cys (b) and with CTAB (c). The first deposition cycle is 1X and the fifth deposition cycle is 5X.

Table A 3.1 SPR peak positions of Au samples in the absence and presence of surfactants, recorded corresponding to each deposition cycle.

# of deposition cycles	SPR peak position (nm)		
	Au only	Au with L-Cys	Au with CTAB
1X	534	532	534
2X	534	535	546
3X	539	544	543
4X	541	544	546
5X	554	542	546

The XRD patterns of Au and Cu-based nanostructures on Si substrate after five deposition cycles are given in Figure A 3.4 (a) and (b) respectively. The sharp peaks seen in the XRD pattern of Au nanostructures indicate that their crystalline structure is of face-centered cubic (fcc) Au.⁶⁷ The peak with the highest intensity is centered at $2\theta = 38.3^\circ$ and can be indexed to Au (111) crystal plane, indicating that a majority of crystal facets in Au nanostructures was (111).

For the Cu-based nanostructures, we observed two weak peaks located at $2\theta = 43.45^\circ$ and 50.55° , which corresponded to Cu (111) and Cu (200) crystal planes of fcc Cu, respectively.^{56,68,69} Thus, based on the XRD data, the composition of Cu-based nanostructures consists of fcc Cu. It should be noticed that, in both Au and Cu-based XRD patterns, Si (111) and (100) peaks were clearly seen.⁷⁰

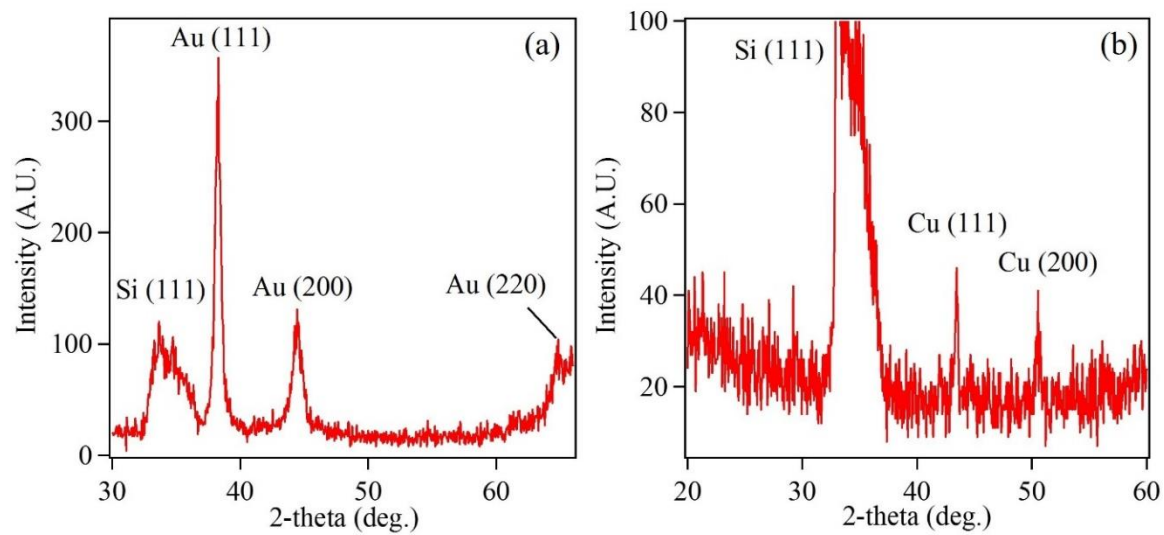


Figure A 3.4 XRD pattern of Au (a) and Cu (b) nanostructures on Si substrate. The patterns suggest an FCC structure of Au and Cu.

CHAPTER 4. EXPLORING THE EFFICACY OF PLATINUM AND PALLADIUM NANOSTRUCTURES FOR ORGANIC MOLECULE DETECTION VIA RAMAN SPECTROSCOPY

Minh Tran¹, Alison Whale² and Sonal Padalkar^{1,3*}

1. Department of Mechanical Engineering, Iowa State University, Ames, IA 50011, USA

2. Department of Materials Science and Engineering, Iowa State University, Ames, IA 50011, USA

3. Microelectronics Research Center, Iowa State University, Ames, IA 50011, USA

* Correspondence: padalkar@iastate.edu; Tel.: +1-51529-46066

Abstract

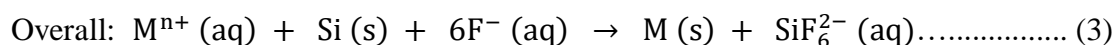
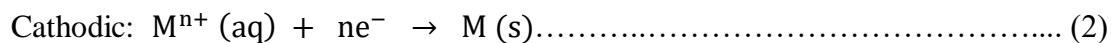
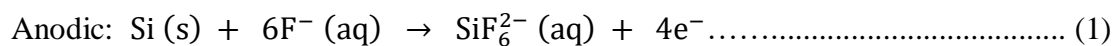
Noble transition metals, like palladium (Pd) and platinum (Pt), have been well-known for their excellent catalytic and electrochemical properties. However, they have been considered non-active for surface enhanced Raman spectroscopy (SERS). In this work, we explore the scattering contributions of Pd and Pt for the detection of organic molecules. The Pd and Pt nanostructures were synthesized on silicon substrate using a modified galvanic displacement method. The results show Pt nanoparticles and dendritic Pd nanostructures with controlled density and size. The influence of surfactants, including sodium dodecyl sulfate and cetyltrimethylammonium bromide, on the size and morphology of the nanostructures was investigated. The Pd and Pt nanostructures with a combination of large size and high density were then used to explore their applicability for the detection of 10^{-5} M Rhodamine 6G and 10^{-2} M paraoxon

Introduction

Galvanic displacement is one of the electrochemical methods used to fabricate metals on semiconductor surfaces. In this method, metallic precursors are reduced by semiconductor substrates in place of reductants or external current source.^{1,2} As a result, galvanic displacement is simple, inexpensive and self-limiting. Galvanic displacement is also substrate selective since metals can only be deposited on substrates, where electron exchange can occur. This selectivity also leads to conformity of the coating regardless of the geometric complexity of the substrates.^{3,4} Metallic deposition via galvanic displacement is a self-limiting process, which is hindered by the complete metal coverage of the substrate thereby blocking the access to electron for further reduction of the metallic precursors¹. With these advantages, there has been an increase in the use of galvanic displacement for nanofabrication in which metals, having distinct morphologies, are distributed randomly or with defined patterns on Si substrates⁵⁻¹¹. Likewise, galvanic displacement was also used to deposit metals on 1D Si nanostructures¹²⁻¹⁴. Further, the growth and interface characteristics of metals on underlying semiconductor substrates by galvanic displacement have served as important topics for fundamental studies¹⁴⁻¹⁸. So far, a variety of metals has been deposited by galvanic displacement on Si and Ge substrates, including noble metals Au/Si,^{3,6,7,10,12,14-21} Au/Ge,^{3,8} Ag/Si,^{9,13,15,16,20,22} platinum-group metals such as Pt/Si,^{7,11,15,23} Pt/Ge,⁸ Pd/Ge,^{8,15} Pd/Si,¹⁵ Rh/Si,¹⁵ base metals such as Cu/Si,^{5,15,24-31} Ni/Si,²⁶ and several metals on III-V semiconductor substrates.¹

In galvanic displacement, the semiconductor substrate acts as an electron source via its surface oxidation. Likewise, metal ions in solution, taking up electrons supplied by the substrate, are reduced to metal atoms. Thus, the overall displacement process occurs when

metals are deposited on the semiconductor substrate and the surface oxide is dissolved, as described by the following chemical equations:^{1,3}



where M denotes any metal whose standard redox potential is higher than that of hydrogen. The role of hydrofluoric acid (HF) is to maintain electron supply by dissolving the surface oxide.

Platinum (Pt) and palladium (Pd) are noble transition metals whose excellent catalytic and electrochemical properties have been widely used in modern technologies, including chemical and biosensing,³²⁻³⁴ photocatalysis,^{35,36} electrocatalysis,³⁷⁻⁴⁰ and Si nanowire growth^{4,41}. Although they are promising candidates for a variety of applications, they are not favorably suited for detection via Raman spectroscopy, also called as Surface Enhanced Raman Spectroscopy (SERS). These transition metals have interband excitation occurring in the visible light region and thus quenching the effect of surface plasmon resonance (SPR),⁴²⁻⁴⁴ which has been considered the major mechanism behind the Raman signal enhancement observed in SERS-active materials like Au and Ag. One method to improve the SERS efficiency of Pt and Pd is called borrowing SERS activity in which the SERS substrate is constituted of a SERS-active core (Au or Ag) and a transition metal shell.⁴⁵ However, to avoid blocking the SPR effect of the rough core underneath, the transition metal shell are required to be atomically thin. Further, the shell must be pinhole free to avoid the core from adsorbing the analytes. Both requirements can be challenging to fabricate.^{42,43} Alternatively, Pt or Pd alone can be used as substrate material, whose surface nanostructure can be

engineered to generate SERS signal. Electrochemically roughened Pd and Pt surfaces were used to detect 0.01 M pyridine^{46,47} and 10^{-5} M thiocyanate⁴⁸ with an enhancement factor (EF) up to three orders of magnitude for Pd, via SERS⁴⁷. While the authors showed that SERS activities were dependent on surface roughness, the surface morphologies were often inhomogeneous across the surface and between substrates, leading to deviations in SERS measurements. Bartlett et al. reported that close packed hexagonal arrays of uniform and well-defined Pd and Pt nanovoids exhibited SERS spectra for 10^{-2} M benzenethiol with significant EFs for Pd and Pt⁴⁴. Monodisperse Pt and Pd nanostructures of several different morphologies have also been synthesized for SERS, including Pd urchins/flowers/hemispheres and Pt pinecones/microspheres/flowers by galvanic displacement for the detection of rhodamine 6G (R6G),^{37,49} Pd flowers/pinecones and Pt nanothorns by electrodeposition for 4-mercaptopyridine and pyridine,^{50,51} and Pd nanodendrites/polyhedra by solution-based chemical reduction for R6G and 4-mercaptobenzoic acid^{40,52}. So far, analyte concentration as low as 10^{-6} M R6G and EF up to 10^5 for 4-mercaptopyridine have been achieved with Pd urchins⁴⁹ and Pd flowers,⁵⁰ respectively, which are comparable to those of Ag or Au.

Several Au and Ag-based SERS substrates have been fabricated by galvanic displacement due to its simplicity and rapid formation of the nanostructures⁵³. On the other hand, there has been limited number of papers describing galvanic displacement as the fabrication method for Pt and Pd-based SERS substrates. Likewise, when HF is used in the plating solution, it may create some limitations. To achieve high deposition rate, many authors described the use of high HF concentrations, up to a few molars. Concentrated HF may reduce the deposition density by replacing Si-H bonds with Si-F bonds, thus slowing

down new nucleation.^{4,36} Further, HF is highly corrosive and poisonous. The use of excessive HF will require extra caution and expensive waste treatment.

To overcome these limitations, few authors reported successful fabrication of metallic nanostructures on Si without HF.^{7,19} As demonstrated in the present work, a very short reaction time, the fluoride-free method, is likely to result in controlled density, size, and growth. Here, we report on the deposition of Pt and Pd on n-Si (100) substrate by modification of the galvanic displacement process. Only small amount of HF would be added to the plating solution, and HF would be concentrated at the solid-liquid interface, making metallic deposition more efficient. By using cyclic deposition, the size and morphology evolution was observed. Further, high density nanostructures were successfully achieved in the absence of concentrated reagents. Additionally, the influence of surfactants, including sodium dodecyl sulfate (SDS) and cetyltrimethylammonium bromide (CTAB), on the size and morphology of the nanostructures was investigated. The deposited Pd and Pt nanostructures were then used for SERS detection of R6G and paraoxon with detection limits of 10^{-5} M and 10^{-2} M, as well as EFs up to 10^2 and 10, respectively.

A range of characterization methods was employed to assist the investigation. Scanning electron microscopy (SEM) was used to determine morphology, size, and density of the nanostructures. Chemical information of the nanostructures was obtained by energy dispersive x-ray spectroscopy (EDX). Finally, surface plasmon resonance (SPR) absorption and SERS properties of the nanostructures were recorded by UV-Vis spectroscopy and Raman spectroscopy, respectively.

Experimental Details

The chemicals used for metallic deposition included potassium tetrachloroplatinate(II) (K_2PtCl_4 , $\geq 99.9\%$), sodium tetrachloropalladate(II) (Na_2PdCl_4 , 98%),

and cetyltrimethylammonium bromide ($C_{19}H_{42}BrN$, $\geq 99.9\%$) purchased from Sigma Aldrich (Milwaukee, WI, USA), sodium dodecyl sulfate ($C_{12}H_{25}NaO_4S$, $\geq 99\%$) from Fisher Scientific, which were used as received. Hydrofluoric acid (HF, 48-51%) was purchased from Thermo Fisher Scientific (Waltham, MA, USA). For SERS experiments, Rhodamine 6G dye (R6G, 99%) and paraoxon-ethyl ($C_{10}H_{14}NO_6P$, $\geq 90\%$) were purchased from Sigma Aldrich (Milwaukee, WI, USA). All solutions were prepared using deionized (DI) water. HF was contained in a polypropylene beaker for experimental use. The substrate was Si (100) wafer (4", single-crystalline, n-type, $\rho = 3-9 \Omega\text{cm}$) purchased from El-Cat Inc. (Ridgefield Park, NJ, USA). Prior to deposition, Si wafer was cleaved into $1.5 \text{ cm} \times 1.5 \text{ cm}^2$ pieces. The chemicals used for cleaning Si substrate were acetone and ethanol (100%, 200 proof).

The Pd and Pt nanostructures were synthesized by the galvanic displacement method as illustrated in Figure 4.1. The synthesis procedure includes, cleaning the Si substrate with acetone, followed by ethanol and DI water. Each cleaning step was performed for 10 min., in an ultrasonic bath to degrease and de-contaminate the substrate. For the deposition, the Si substrate was immersed in 10% (w/w) HF solution for 2 minutes to eliminate surface oxide and activate the surface. The substrate was then instantly immersed for 5 min. in 0.3 mM K_2PtCl_4 or Na_2PdCl_4 for Pt or Pd deposition, respectively followed by rinsing with deionized water. This deposition procedure will be denoted as 1 deposition cycle. Multiple deposition cycles were also used in the present investigation. For experiments with surfactants, the metallic precursor solution was composed of 0.1 mM SDS or CTAB with 0.3 mM K_2PtCl_4 or Na_2PdCl_4 . Finally, the Pt and Pd nanostructures were air dried and stored for further characterization.

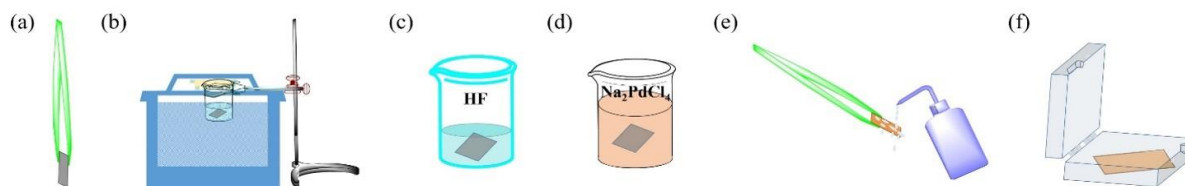


Figure 4.1 (a) Cleaved Si substrate. (b) Clean Si substrate with acetone, ethanol, and DI water in an ultrasonic bath. (c) Immersion in 10% (w/w) HF solution. (d) Immersion of Si substrate in 0.3 mM metallic precursor solution. (e) Rinse sample with DI water (f) Store dry sample.

The R6G dye solution was prepared by dissolving 0.8 mg of R6G in 5 mL of DI water and used as stock solution. Similarly, paraoxon stock solution was prepared by mixing 30 μL paraoxon with 0.98 mL deionized water. The SERS substrates were prepared by using Si substrates with Pt or Pd nanostructures, on which a small volume (300 μL) of the stock solution was drop casted and dried under ambient conditions. Prior to drop casting the analyte, the sample was treated with ambient air plasma for 1 minute under medium radio frequency power level (11 W) by a plasma cleaner (PDC-001, Harrick Plasma, Ithaca, NY).

The size and morphology of the nanostructures were studied by scanning electron microscopy (SEM) using a FEI Quanta-250 SEM instrument at 10 kV accelerating voltage. The SEM instrument was equipped with an Oxford Aztec energy dispersive x-ray (EDX) analysis system, which was used to conduct elemental analyses of the deposited nanostructures. UV-Vis absorption spectroscopy was recorded by a Perkin Elmer Lambda 25 spectrophotometer. To prepare samples for UV-Vis measurements, each sample was immersed in 1 mL DI water and sonicated at the highest power for 1-3 minutes to detach the metallic nanostructures from Si substrate and disperse them in DI water. SERS measurements were performed at room temperature on a Renishaw Dispersive Raman Spectrometer with Ar-ion laser running at 488 nm, using 50x objective lens, with incident

power of 5 mW for 4 accumulations, each of 30 s duration. SERS spectra were collected from several random regions on each sample to confirm reproducibility.

Results and Discussions

Figure 4.2 correlates the number of deposition cycles with the density, morphology evolution, and size of Pd nanostructures on Si substrate (additional lower-magnification SEM images as well as size distribution and density charts can be seen in the Supporting Information).

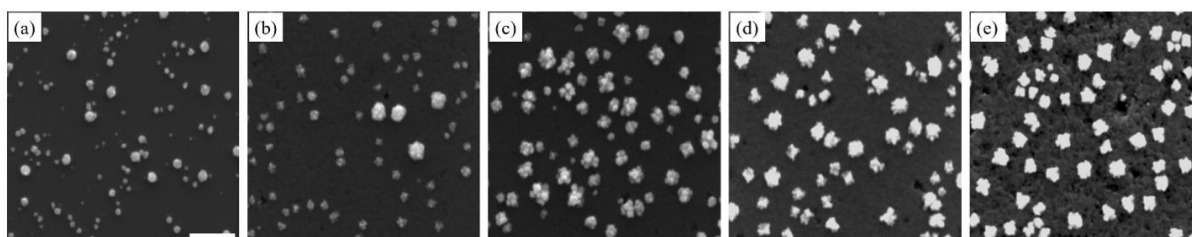


Figure 4.2 SEM images of Pd nanostructures deposited on Si substrate after (a) first, (b) third, (c) fifth, (d) eighth, and (e) tenth deposition cycle. The scale bar is 500 nm.

Upon the first deposition cycle, Pd nanostructures appeared to be quasi-spherical (Figure 4.2a). The large size distribution indicated that nucleation and growth occurred simultaneously, following the progressive nucleation mode. When the number of deposition cycles increased, Pd nanostructures also increased in size (Figure 4.2 b, c). The growth was anisotropic due to new Pd atoms preferably deposited on high-energy facets in the radial direction. Pd nanostructures, thus, had very rough surfaces. In several cases, the anisotropic growth led to the formation of flower like structures or clusters of small Pd nanostructures. With the increase in the deposition cycles, the dendritic Pd nanostructures appeared more compact, minimizing the surface area to achieve a stable configuration (Figure 4.2 d, e)⁵⁴. Likewise, when the number of deposition cycles increased, the size distribution was reduced. After repeated deposition cycles, the native oxide on the Si substrate was continuously dissolved by HF, creating a very rough and porous Si layer on the substrate. This layer had

high electrical resistance enough to hinder electron transfer between Pd and the substrate, and suppresses nucleation. In addition, more Pd nanostructures acted as nucleation centers to compete with Si substrate for new Pd atoms. New Pd atoms would preferably adsorb on the existing Pd nanostructures since they had higher electronegativity than Si.⁴¹

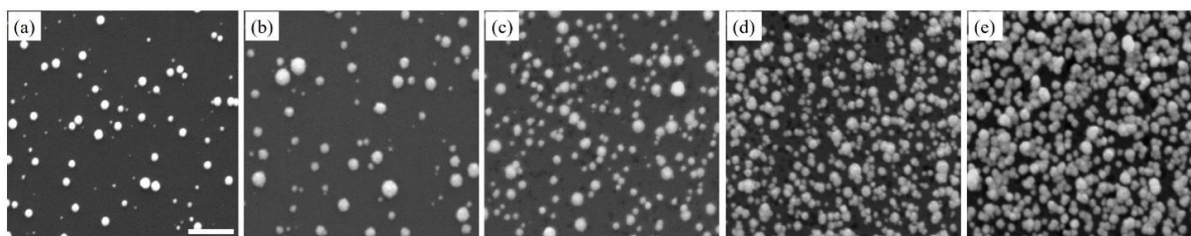


Figure 4.3 SEM images of Pt nanostructures deposited on Si substrate after (a) first, (b) third, (c) fifth, (d) eighth, and (e) tenth deposition cycle. The scale bar is 500 nm.

In contrast, Pt nanostructures showed a steady increase in density with respect to increasing number of deposition cycles (Figure 4.3 and Figure A 4.3b). This increase in density was a result of the continuous formation of new nuclei at every deposition cycle as the growth and nucleation followed the progressive mode. However, it is also noteworthy that Pt nanostructures were more uniform in size after repeated deposition cycles (Figure A 4.2), likely due to Ostwald ripening and the faster growth of smaller, high-energy nanostructures. In addition, while Pt nanostructures grew larger in size, their growth was isotropic and they maintained a spherical shape. When Pt nanostructures were sufficiently close to each other, they diffused and aggregated. At high densities, fusion between Pt nanostructures occurred, resulting in large regions of continuous Pt up to a micron in size. In Figure 4.2 and Figure 4.3, considerable number of deep pits of different sizes were noticed on the substrate surface. On n-type Si substrate, these pits were the locations of surface defects, and electrons/holes exchange occurred locally at these pits during the very early stages of deposition^{55,56}.

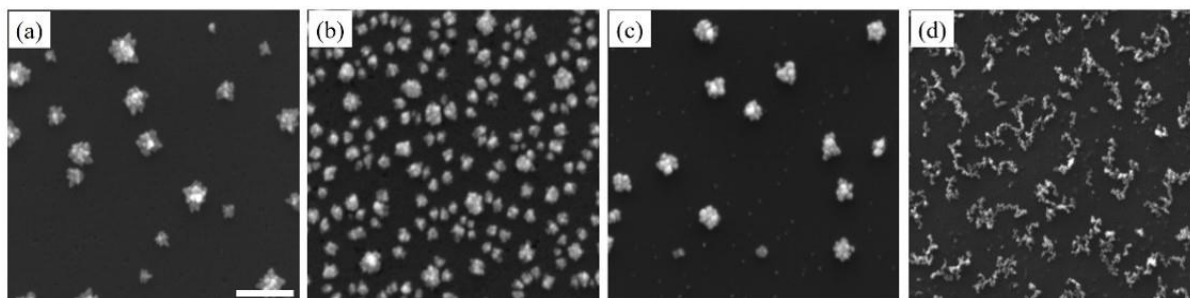


Figure 4.4 SEM images of Pd nanostructures deposited on Si substrate after (a) first, (b) tenth deposition cycle with SDS surfactant added, and (c) first, (d) tenth deposition cycle with CTAB surfactant added. The scale bar is 500 nm.

Sodium dodecyl sulfate (SDS), an anionic surfactant, and cetyltrimethylammonium bromide (CTAB), a cationic surfactant, have been widely used as stabilizers^{57,58} and morphology-directing reagents^{49,59,60} for the growth of various metallic nanostructures. As shown in Figure 4.4, upon the addition of SDS and CTAB, dendritic Pd nanostructures were observed after just one deposition cycle (Figure 4.4 a, c). Clearly, the presence of surfactants promoted anisotropic growth by selectively adsorbing on certain crystal facets of the growing Pd nanostructures and slowing down the diffusion of Pd atoms to those facets. The dendritic Pd nanostructures with SDS also had longer and sharper branches, indicating that SDS induced anisotropic growth more strongly. Furthermore, adding either SDS or CTAB appeared to accelerate the growth of Pd nanostructures. In the case of SDS, the adsorption of free anionic surfactant molecules to the surfaces would give Pd nanostructures additional negative charges, which electrostatically attracted Pd atoms toward them. On the other hand, at the concentration of 0.1 mM, CTAB would adsorb on the surfaces of the Pd nanostructures as both sub-micelle aggregates and free surfactant molecules.⁶¹ Their positively charged head groups, electrostatically binding PdCl_4^{2-} , thus attract and concentrate Pd precursors toward the Pd nanostructures. Figure 4.4b and Figure 4.4d show Pd nanostructures with SDS and CTAB after ten deposition cycles, respectively. The Pd nanostructures with SDS were

smaller when compared with Pd nanostructures without surfactant. Their branches were also shorter and blunt after ten deposition cycles. The observed shrinking of Pd nanostructures after multiple deposition cycles could be a combination of the increasing impeded growth caused by a denser and thicker surfactant layer, and the rearrangement of the high-energy and unstable Pd atoms at the sharp tips of the branches. On the other hand, Pd nanostructures with CTAB after ten deposition cycles transformed into 2D fragmented networks of much smaller Pd nanoparticles. The mechanism behind the formation of such structures is unclear and subject to further investigation.

Figure 4.5 shows SEM images of Pt nanostructures obtained by the addition of surfactants like SDS and CTAB. Unlike the Pd nanostructures, there was no noticeable difference between Pt nanostructures with and without SDS, indicating that SDS had limited influence toward the growth of Pt nanostructures (Figure 4.5 a, b). In Figure 4.5b there were large number of pits on the Si surface, which could be due to Pt nanostructure detachment. The addition of CTAB considerably increased the density of Pt nanostructures. The formation of sub-micelle aggregates facilitated the galvanic displacement process by confining metal ions close to the surface of the sub-micelles, thus increasing reaction rate by bringing the reactants closer together at the micellar interface.⁶¹ The morphology, however, slightly deviated from the spherical shape and this can be attributed to the slight anisotropic growth induced by selective adsorption of CTAB (Figure 4.5c). With further deposition cycles (Figure 4.5d), high density of Pt nanostructures was observed. The densely packed nanostructures combined with anisotropic growth led to coalescence of nearby nanostructures and a sub-monolayer coverage.

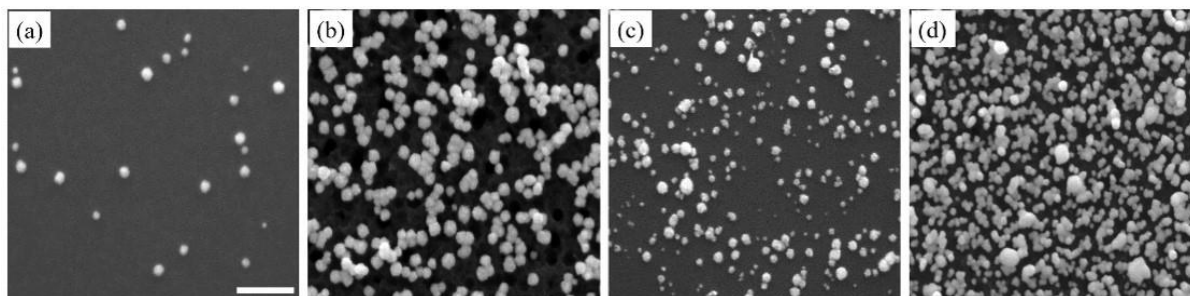


Figure 4.5 SEM images of Pt nanostructures deposited on Si substrate after (a) first, (b) tenth deposition cycle with SDS surfactant added, and (c) first, (d) tenth deposition cycle with CTAB surfactant added. The scale bar is 500 nm.

Chemical compositions of the as-synthesized samples were determined by EDX (Figure 4.6). The Pd or Pt peaks were observed for each respective metal-deposited sample. In addition, different Pd or Pt peak intensities were observed at different spots, reflecting different sizes of the nanostructures. A very strong Si peak was obtained from the substrate. C peak was detected due to possible organic contaminants adsorbing on the sample surface prior to its introduction to the SEM vacuum chamber, while O peak could be a result of the slight oxidation of the Si surface.

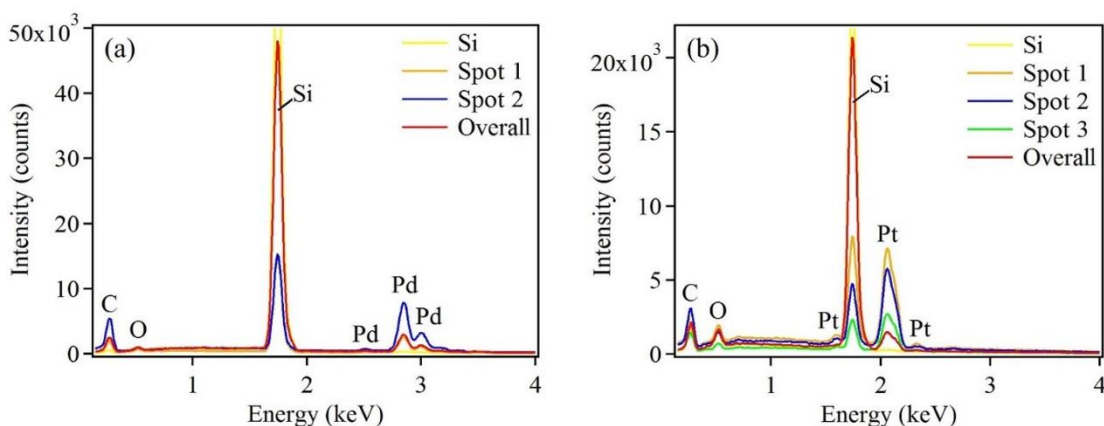


Figure 4.6 EDX patterns of (a) Pd and (b) Pt nanostructures deposited on Si substrates after five deposition cycles showing the presence of Pd and Pt, respectively. EDX patterns recorded from individual nanostructures are presented as spots 1, 2, and 3.

In addition to EDX, UV-Vis data was also obtained. Figure 4.7 shows UV-Vis spectra of Pt and Pd nanostructures deposited on Si substrates. Both spectra showed no noticeable

absorption peak in the visible region, and both showed increasing absorption toward the ultraviolet region. This result, thus, provided evidence that Pt and Pd did not have SPR property in the visible region as mentioned above. In addition, both the spectra show two small and broad absorption bands centered at 210 nm and 325 nm for Pd, as well as at 194 nm and 313 nm for Pt. The UV-Vis absorption data were also in agreement with those reported in the literature.^{62,63}

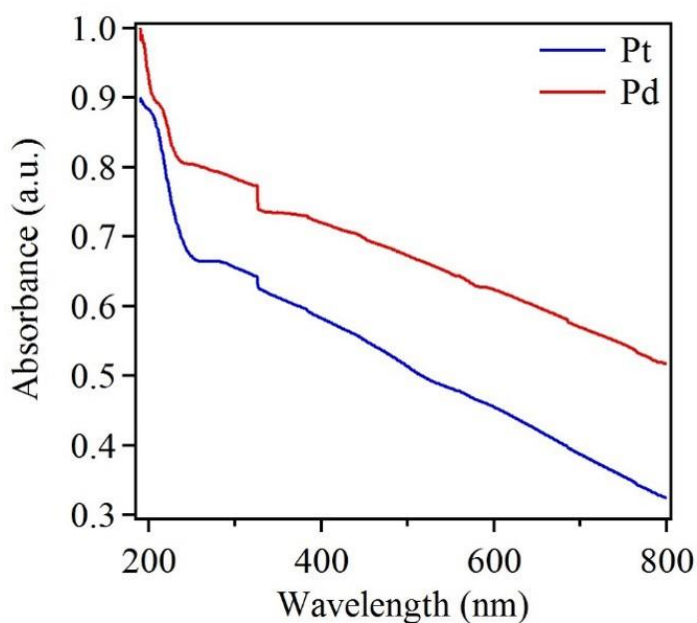


Figure 4.7 Normalized UV-Vis spectra of Pt and Pd nanostructures deposited on Si substrates after five deposition cycles, showing characteristic peaks and increasing absorption toward shorter wavelengths. The spectrum of Pt nanostructures was shifted downward for clarity

To evaluate the Pt and Pd nanostructures as possible platforms for SERS application, R6G was chosen as a probe molecule. R6G has been widely used for SERS due to their well-defined vibrational features. To obtain the best performance of SERS substrates, samples with a combination of high-density and large metallic nanostructures were used. These samples were achieved after ten deposition cycles (see Figure A 4.3 and Table A 4.1). Figure 4.8a shows Raman spectra of 10^{-5} M R6G dye, drop casted onto Pt and Pd nanostructures.

For comparison, the same amount of R6G was also drop cast onto bare Si substrate without metallic deposition. No noticeable Raman signal was detected using this bare Si substrate. On the other hand, several strong Raman modes were observed for the Pd nanostructure sample. Nearly all of these Raman modes were also visible for the Pt nanostructure sample. However, their intensities were significantly reduced.

In addition to R6G detection, paraoxon was used as a probe molecule. It is also important to note that paraoxon is a smaller molecule compared to R6G and thus is more challenging to detect via SERS. Here, Pt and Pd nanostructure platform was used to demonstrate their ability to detect small molecules as paraoxon. Paraoxon is an organophosphorus compound and is used to regulate pests in crops and plants. It is highly toxic, causing detrimental health problems if exposed to food and drinking water ⁶⁴. SERS can be used for rapid detection of such pesticides. Figure 4.8b shows Raman spectra of 10^{-2} M paraoxon drop casted on Pt and Pd nanostructures. The three strongest fingerprint peaks representing different vibrational modes of paraoxon molecule were clearly seen in these spectra ⁶⁵. Raman scattering was certainly enhanced by the metallic nanostructures because no other peaks, except that of Si, were observed when bare Si was used as SERS substrate. Table 4.1 provides detailed assignment for all the peaks in Figure 4.8 according to published data.

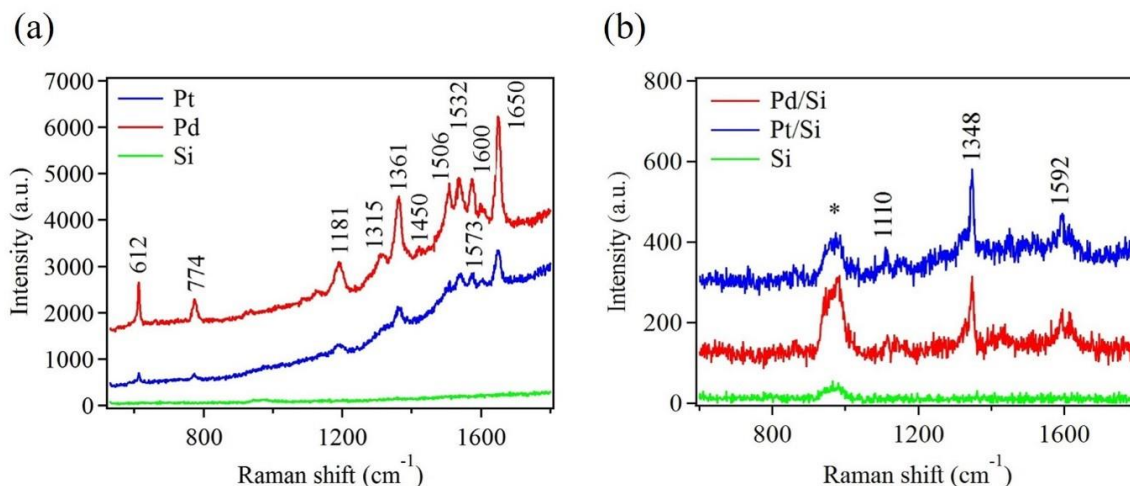


Figure 4.8 Raman spectra of (a) 10-5 M R6G and (b) 10-2 M paraoxon adsorbed on Pd and Pt nanostructures deposited on Si substrates after ten deposition cycles. Raman spectra of R6G and paraoxon adsorbed on bare Si substrates are shown for comparison. The (*) indicates Raman mode of Si

Table 4.1 Raman mode assignments for R6G and paraoxon, corresponding to Figure 4.8

Raman (cm ⁻¹)	Assignment for R6G	Reference
612	In-plane bending of C-C-C ring	66-68
774	C-H out-of-plane bending	66-69
1181	In-plane xanthen ring deformation, C-H bending, N-H bending	66-69
1315	Aromatic C-C stretching	66,67
1361, 1450	Aromatic C-C stretching, in-plane C-H bending	66-69
1506, 1532	Aromatic C-C and C-N stretching, C-H and N-H bending	66,67,69
1573, 1600	Aromatic C-C stretching, in-plane N-H bending	66,67,69
1650	Aromatic C-C stretching, in-plane C-H bending	66-69
Raman (cm ⁻¹)	Assignment for paraoxon	
1110	C-H band (in plane)/NO ₂ asymmetric stretching	65,70
1348	Symmetry stretching NO ₂	65,70
1592	Phenyl ring vibration	65,70

The enhancement factor (EF) was determined to quantitatively evaluate the effectiveness of SERS substrate. The most widely used definition of the EF is described as

$$EF = \frac{I_{SERS}/c_{SERS}}{I_{RS}/c_{RS}}$$

where I_{SERS} and I_{RS} are Raman intensities of SERS and non-SERS substrates, respectively, while c_{SERS} and c_{RS} are analyte concentrations used for SERS and non-SERS substrates, respectively⁷¹. In the present study, same analyte concentrations were used for both substrates. Thus, EF was simply a ratio of I_{SERS} and I_{RS} . However, since Raman signal obtained from bare Si substrate (I_{RS}) was too weak to be detected by our instrument, it was not possible to obtain absolute values for EF. Instead, we only roughly estimated EFs in a manner similar to those reported by Yamamoto et al.⁶⁹ Thus, EF value for R6G on Pd was $\sim 10^2$, which was ~ 3 times higher than that for Pt. Similarly, EF values for paraoxon on Pd and Pt both were ~ 10 .

The Raman enhancement can be attributed to the local electromagnetic enhancement^{72,73}. For nanostructures of noble metals, the extent of electromagnetic enhancement depends not only on their material but also on their morphology, size, and density. It has been reported that large electromagnetic enhancement occurs at the sharp features or high curvature sites due to the lightning-rod effect^{50,72,74}. Thus, the Pd nanostructures would amplify the electromagnetic field surrounding them, and would be a promising SERS substrate. Tian et al. used 3D finite difference time domain method to predict that the maximum enhancement would occur at the tip's apex of the Pd nanostructure's branch⁷⁴. In addition, large field enhancement would also occur at the gaps between adjacent branches, called as hot spots, due to the coupling effects between the branches. This morphological advantage was the key factor that increased the SERS

performance of Pd nanostructures for R6G over that of Pt nanospheres. Furthermore, overall, Pd nanostructures were larger than Pt nanostructures (see the Supporting Information), and larger size in the case of transition metals might lead to stronger enhancement⁷⁵. Also, larger Pd nanostructures would likely adsorb a greater number of the probe molecules, and thus were more sensitive and effective than Pt. Further improvement in SERS detection can be achieved from the Pd-deposited substrate by increasing the density of Pd nanostructures making very small gaps between the nanostructures to generate hot spots⁷⁶. Additionally, the surface roughness of the underlying Si substrate would also contribute to the enhanced Raman signal during the detection event. Further, similar explanation will also hold for Pt nanostructures.

Conclusion

In summary, we report a modification of the galvanic displacement method in which Pt and Pd nanostructures were deposited on n-type Si substrate with limited exposure to HF. By performing multiple cycles of the metallic deposition steps, large dendritic Pd and Pt nanostructures with high density and small size distribution were obtained. When SDS and CTAB surfactants were utilized, an increase in anisotropic growth of the dendritic Pd nanostructures was observed. A higher density of Pt nanostructures was observed when CTAB was utilized. Further, the Pd and Pt nanostructures were successfully used as SERS platforms for detecting low concentrations of organic analytes.

References

1. Carraro, C.; Maboudian, R.; Magagnin, L. *Surface Science Reports* **2007**, *62* (12), 499-525.
2. Ali, H. O.; Christie, I. R. A. *Gold Bull.* **1984**, *17* (4), 118-127.

3. Magagnin, L.; Maboudian, R.; Carraro, C. *Journal of Physical Chemistry B* **2002**, *106* (2), 401-407.
4. Cerruti, M.; Doerk, G.; Hernandez, G.; Carraro, C.; Maboudian, R. *Langmuir* **2010**, *26* (1), 432-437.
5. Lee, Y.; Tsai, M.; Hu, T.; Dai, B.; Feng, M. *Electrochemical and Solid State Letters* **2001**, *4* (7), C47-C49.
6. Zhang, X.; Qiao, Y.; Xu, L.; Buriak, L. *Acs Nano* **2011**, *5* (6), 5015-5024.
7. Fabre, B.; Hennous, L.; Ababou-Girard, S.; Meriadec, C. *Acs Applied Materials & Interfaces* **2013**, *5* (2), 338-343.
8. Porter, L.; Choi, H.; Schmeltzer, J.; Ribbe, A.; Elliott, L.; Buriak, J. *Nano Letters* **2002**, *2* (12), 1369-1372.
9. Liu, F.; Green, M. *Journal of Materials Chemistry* **2004**, *14* (10), 1526-1532.
10. Lahiri, A.; Wen, R.; Kuimalee, S.; Kobayashi, S.; Park, H. *Crystengcomm* **2012**, *14* (4), 1241-1246.

11. Kawasaki, H.; Yao, T.; Suganuma, T.; Okumura, K.; Iwaki, Y.; Yonezawa, T.; Kikuchi, T.; Arakawa, R. *Chemistry-a European Journal* **2010**, *16* (35), 10832-10843.
12. Yang, X.; Zhong, H.; Zhu, Y.; Shen, J.; Li, C. *Dalton Transactions* **2013**, *42* (39), 14324-14330.
13. Huang, J.; Chen, F.; Zhang, Q.; Zhan, Y.; Ma, D.; Xu, K.; Zhao, Y. *Acs Applied Materials & Interfaces* **2015**, *7* (10), 5725-5735.
14. Sayed, S.; Wang, F.; Malac, M.; Li, P.; Wang, D.; Buriak, J. *Crystengcomm* **2012**, *14* (16), 5230-5234.
15. Yae, S.; Nasu, N.; Matsumoto, K.; Hagihara, T.; Fukumuro, N.; Matsuda, H. *Electrochimica Acta* **2007**, *53* (1), 35-41.
16. Peng, K.; Zhu, J. *Electrochimica Acta* **2004**, *49* (16), 2563-2568.
17. Sayed, S.; Wang, F.; Mallac, M.; Meldrum, A.; Egerton, R.; Buriak, J. *Acs Nano* **2009**, *3* (9), 2809-2817.
18. Warren, S.; Reitzle, A.; Kazimirov, A.; Ziegler, J.; Bunk, O.; Cao, L.; Renner, F.; Kolb, D.; Bedzyk, M.; Zegenhagen, J. *Surface Science* **2002**, *496* (3), 287-298.

19. Gutes, A.; Carraro, C.; Maboudian, R. *Acs Applied Materials & Interfaces* **2011**, *3* (5), 1581-1584.
20. Aizawa, M.; Buriak, J. *Journal of the American Chemical Society* **2006**, *128* (17), 5877-5886.
21. Rossiter, C.; Suni, I. *Surface Science* **1999**, *430* (1-3), L553-L557.
22. Hochbaum, A.; Chen, R.; Delgado, R.; Liang, W.; Garnett, E.; Najarian, M.; Majumdar, A.; Yang, P. *Nature* **2008**, *451* (7175), 163-U5.
23. Gorostiza, P.; Allongue, P.; Diaz, R.; Morante, J.; Sanz, F. *Journal of Physical Chemistry B* **2003**, *107* (26), 6454-6461.
24. Cho, J. S. H.; Kang, H. K.; Wong, S. S.; Shachamdiamand, Y. *Mrs Bulletin* **1993**, *18* (6), 31-38.
25. Darosa, C.; Iglesia, E.; Maboudian, R. *Journal of the Electrochemical Society* **2008**, *155* (3), D244-D250.
26. Zhang, Y.; Ang, S.; Tay, A.; Xu, D.; Kang, E.; Neoh, K.; Chong, L.; Huan, A. *Langmuir* **2003**, *19* (17), 6802-6806.

27. Scheck, C.; Liu, Y.; Evans, P.; Schad, R.; Bowers, A.; Zangari, G.; Williams, J.; Issacs-Smith, T. *Journal of Vacuum Science & Technology a* **2004**, *22* (4), 1842-1846.
28. Lim, S.; Mo, R.; Pianetta, P.; Chidsey, C. *Journal of the Electrochemical Society* **2001**, *148* (1), C16-C20.
29. Ye, S.; Ichihara, T.; Uosaki, K. *Journal of the Electrochemical Society* **2001**, *148* (6), C421-C426.
30. Dhingra, S.; Sharma, R.; George, P. *Solid-State Electronics* **1999**, *43* (12), 2231-2234.
31. Nagahara, L. A.; Ohmori, T.; Hashimoto, K.; Fujishima, A. *Journal of Electroanalytical Chemistry* **1992**, *333* (1-2), 363-369.
32. Zhai, D.; Liu, B.; Shi, Y.; Pan, L.; Wang, Y.; Li, W.; Zhang, R.; Yu, G. *Acs Nano* **2013**, *7* (4), 3540-3546.
33. Guo, S.; Wen, D.; Zhai, Y.; Dong, S.; Wang, E. *Acs Nano* **2010**, *4* (7), 3959-3968.
34. Gutes, A.; Laboriante, I.; Carraro, C.; Maboudian, R. *Sensors and Actuators B-Chemical* **2010**, *147* (2), 681-686.

35. Fabre, B.; Li, G.; Gouttefangeas, F.; Joanny, L.; Loget, G. *Langmuir* **2016**, *32* (45), 11728-11735.
36. Lombardi, I.; Marchionna, S.; Zangari, G.; Pizzini, S. *Langmuir* **2007**, *23* (24), 12413-12420.
37. Ye, W.; Liu, J.; Liu, Q.; Zhou, F.; Liu, W. *Electrochimica Acta* **2010**, *55* (28), 8649-8654.
38. Zhang, H.; Jiang, F.; Zhou, R.; Du, Y.; Yang, P.; Wang, C.; Xu, J. *International Journal of Hydrogen Energy* **2011**, *36* (23), 15052-15059.
39. Bai, J.; Shen, L.; Sun, D.; Tang, Y.; Lu, T. *Crystengcomm* **2014**, *16* (45), 10445-10450.
40. Kannan, P.; Dolinska, J.; Maiyalagan, T.; Opallo, M. *Nanoscale* **2014**, *6* (19), 11169-11176.
41. Cichoszewski, J.; Reuter, M.; Schwerdt, F.; Werner, J. *Electrochimica Acta* **2013**, *109*, 333-339.

42. Tian, Z.; Ren, B.; Wu, D. *Journal of Physical Chemistry B* **2002**, *106* (37), 9463-9483.
43. Stiles, P.; Dieringer, J.; Shah, N.; Van Duyne, R. *Annual Review of Analytical Chemistry* **2008**, *1*, 601-626.
44. Abdelsalam, M.; Mahajan, S.; Bartlett, P.; Baumberg, J.; Russell, A. *Journal of the American Chemical Society* **2007**, *129* (23), 7399-7406.
45. Tian, Z.; Ren, B.; Li, J.; Yang, Z. *Chemical Communications* **2007**, (34), 3514-3534.
46. Cai, W.; Ren, B.; Li, X.; She, C.; Liu, F.; Cai, X.; Tian, Z. *Surface Science* **1998**, *406* (1-3), 9-22.
47. Liu, Z.; Yang, Z.; Cui, L.; Ren, B.; Tian, Z. *Journal of Physical Chemistry C* **2007**, *111* (4), 1770-1775.
48. Tian, Z.; Ren, B.; Mao, B. *Journal of Physical Chemistry B* **1997**, *101* (8), 1338-1346.
49. Chen, L.; Liu, Y. *Crystengcomm* **2011**, *13* (21), 6481-6487.

50. Li, Y.; Lu, G.; Wu, X.; Shi, G. *Journal of Physical Chemistry B* **2006**, *110* (48), 24585-24592.
51. Tian, N.; Zhou, Z.; Sun, S.; Cui, L.; Ren, B.; Tian, Z. *Chemical Communications* **2006**, (39), 4090-4092.
52. Chen, H.; Wei, G.; Ispas, A.; Hickey, S.; Eychmuller, A. *Journal of Physical Chemistry C* **2010**, *114* (50), 21976-21981.
53. Tharmaraj, V.; Yang, J. *Crystengcomm* **2016**, *18* (48), 9275-9280.
54. Bisson, L.; Boissiere, C.; Nicole, L.; Grosso, D.; Jolivet, J.; Thomazeau, C.; Uzio, D.; Berhault, G.; Sanchez, C. *Chemistry of Materials* **2009**, *21* (13), 2668-2678.
55. Gorostiza, P.; Diaz, R.; Servat, J.; Sanz, F.; Morante, J. *Journal of the Electrochemical Society* **1997**, *144* (3), 909-914.
56. Gorostiza, P.; Diaz, R.; Sanz, F.; Morante, J. *Journal of the Electrochemical Society* **1997**, *144* (12), 4119-4122.
57. Chen, Y.; Yeh, C. *Colloids and Surfaces a-Physicochemical and Engineering Aspects* **2002**, *197* (1-3), 133-139.

58. Grzelczak, M.; Perez-Juste, J.; Mulvaney, P.; Liz-Marzan, L. *Chemical Society Reviews* **2008**, *37* (9), 1783-1791.
59. Chen, J.; Xiong, Y.; Yin, Y.; Xia, Y. *Small* **2006**, *2* (11), 1340-1343.
60. Lin, Z.; Lin, M.; Chang, H. *Chemistry-a European Journal* **2009**, *15* (18), 4656-4662.
61. Al-Thabaiti, S.; Obaid, A.; Hussain, S.; Khan, Z. *Arabian Journal of Chemistry* **2015**, *8* (4), 538-544.
62. McLellan, J.; Xiong, Y.; Hu, M.; Xia, Y. *Chemical Physics Letters* **2006**, *417* (1-3), 230-234.
63. Nguyen, V.; Nguyen, D.; Hayakawa, T.; Hirata, H.; Lakshminarayana, G.; Nogami, M. *Nanotechnology* **2010**, *21* (3).
64. Aragay, G.; Pino, F.; Merkoci, A. *Chemical Reviews* **2012**, *112* (10), 5317-5338.
65. Wang, B.; Zhang, L.; Zhou, X. *Spectrochimica Acta Part a-Molecular and Biomolecular Spectroscopy* **2014**, *121*, 63-69.

66. He, X.; Gao, Y.; Mahjouri-Samani, M.; Black, P.; Allen, J.; Mitchell, M.; Xiong, W.; Zhou, Y.; Jiang, L.; Lu, Y. *Nanotechnology* **2012**, *23* (20).
67. Hildebrandt, P.; Stockburger, M. *Journal of Physical Chemistry* **1984**, *88* (24), 5935-5944.
68. Zhang, Y.; Zheng, J.; Gao, G.; Kong, Y.; Zhi, X.; Wang, K.; Zhang, X.; Cui, D. *International Journal of Nanomedicine* **2011**, *6*, 2899-2906.
69. Yamamoto, Y.; Hasegawa, K.; Hasegawa, Y.; Takahashi, N.; Kitahama, Y.; Fukuoka, S.; Murase, N.; Baba, Y.; Ozaki, Y.; Itoh, T. *Physical Chemistry Chemical Physics* **2013**, *15* (35), 14611-14615.
70. Li, P.; Dong, R.; Wu, Y.; Liu, H.; Kong, L.; Yang, L. *Talanta* **2014**, *127*, 269-275.
71. Le Ru, E.; Blackie, E.; Meyer, M.; Etchegoin, P. *Journal of Physical Chemistry C* **2007**, *111* (37), 13794-13803.
72. Sharma, B.; Frontiera, R.; Henry, A.; Ringe, E.; Van Duyne, R. *Materials Today* **2012**, *15* (1-2), 16-25.
73. Doering, W.; Nie, S. *Journal of Physical Chemistry B* **2002**, *106* (2), 311-317.

74. Tian, Z.; Yang, Z.; Ren, B.; Wu, D. *Surface-Enhanced Raman Scattering: Physics and Applications*. Springer: Germany, 2006; Vol. 103.

75. Lin, X.; Cui, Y.; Xu, Y.; Ren, B.; Tian, Z. *Analytical and Bioanalytical Chemistry* **2009**, 394 (7), 1729-1745.

76. Tong, L.; Xu, H.; Kall, M. *Mrs Bulletin* **2014**, 39 (2), 163-168.

Appendix

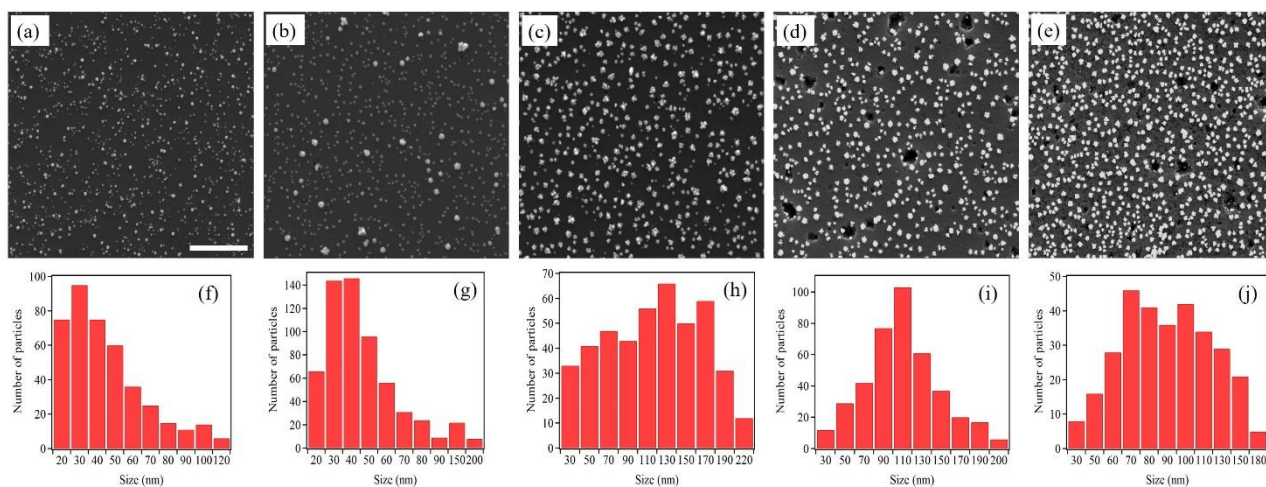


Figure A 4.1 SEM images of Pd nanostructures deposited on Si substrate after (a) first, (b) third, (c) fifth, (d) eighth, and (e) tenth deposition cycle. The scale bar is 2 μm . (f-j) Size distributions of the corresponding Pd nanostructures.

Table A 4.1 Average sizes of Pd and Pt nanostructures after multiple deposition cycles

	One cycle	Three cycles	Five cycles	Eight cycles	Ten cycles
Pd	40 ± 22 nm	43 ± 27 nm	108 ± 51 nm	101 ± 39 nm	86 ± 29 nm
Pt	52 ± 29 nm	46 ± 27 nm	62 ± 30 nm	62 ± 22 nm	68 ± 21 nm

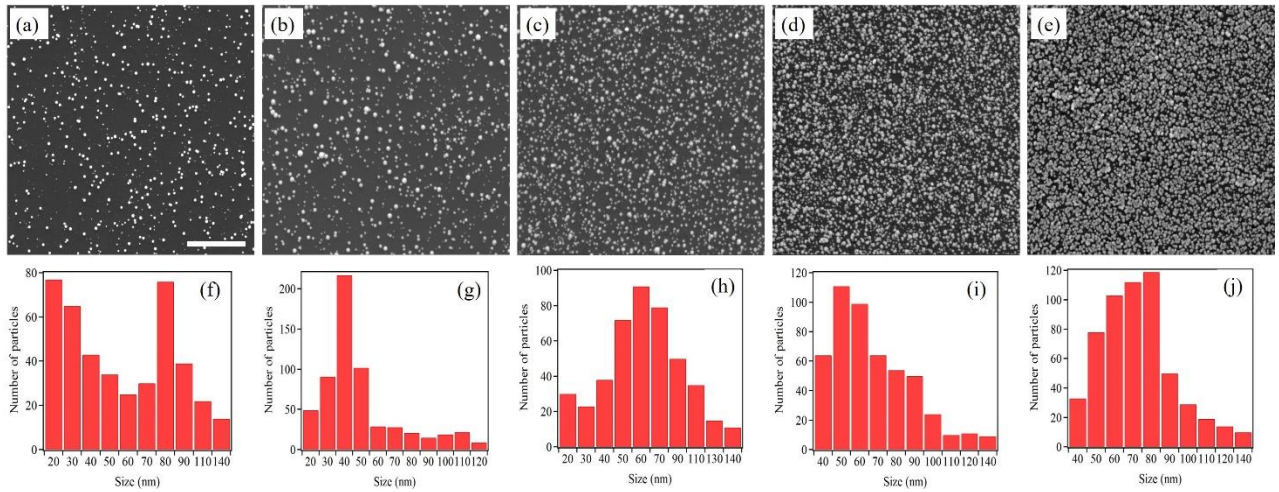


Figure A 4.2 SEM images of Pt nanostructures deposited on Si substrate after (a) first, (b) third, (c) fifth, (d) eighth, and (e) tenth deposition cycle. The scale bar is 2 μm . (f-j) Size distributions of the corresponding Pt nanostructures.

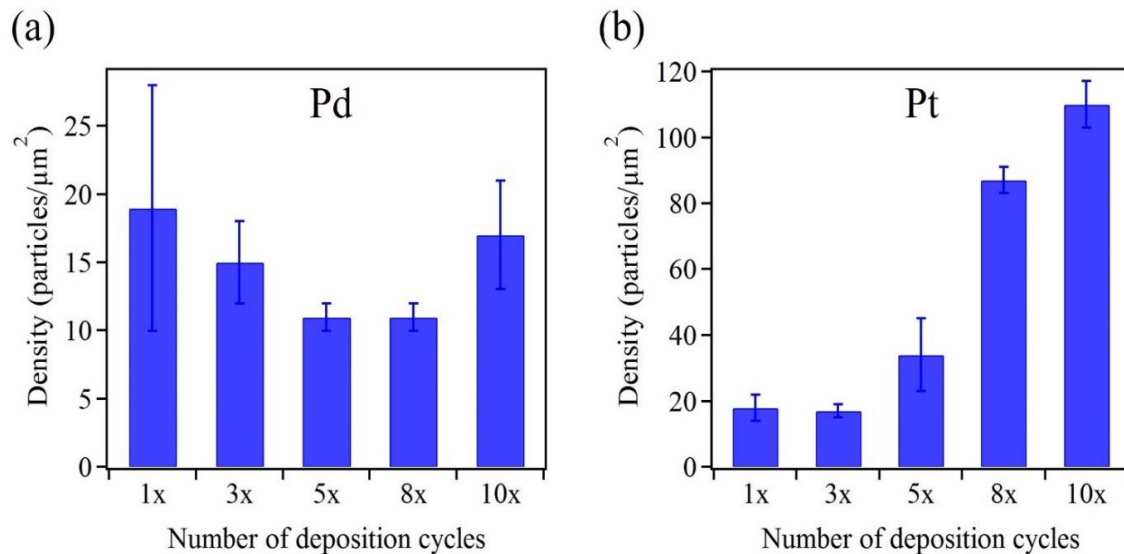


Figure A 4.3 Number densities of (a) Pd and (b) Pt nanostructures after multiple deposition cycles. 1x-10x denote one to ten deposition cycles, respectively.

CHAPTER 5. PREPARATION AND CHARACTERIZATION OF COBALT AND NICKEL NANOSTRUCTURES ON SILICON SUBSTRATES FOR HYDROGEN GENERATION

Minh Tran¹, Tian Lan¹ and Sonal Padalkar^{1,2*}

1. Department of Mechanical Engineering, Iowa State University, Ames, IA 50011, USA

2. Microelectronics Research Center, Iowa State University, Ames, IA 50011, USA

* Correspondence: padalkar@iastate.edu; Tel.: +1-51529-46066

Abstract

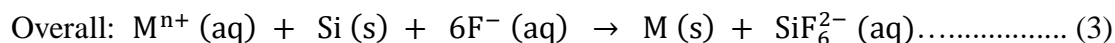
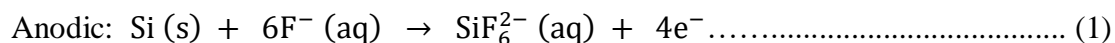
This paper describes the deposition of Co and Ni on n-type Si substrate at elevated temperature in an aqueous basic solution by galvanic displacement. Our results showed that small Co and Ni nanoparticles, with desired sizes and densities, were successfully synthesized by simple modification of the conventional method. Heat treatment of the samples after deposition and the use of surfactants as additives were also performed to investigate their effects on the deposited metallic nanostructures as well as the overall surface morphology.

Introduction

Galvanic displacement is one of the electrochemical methods used to fabricate metals on semiconductor surfaces. In this method, metallic precursors are reduced by semiconductor substrates instead of reductants or external current source.^{1,2} As a result, galvanic displacement is simple and inexpensive. Galvanic displacement is also substrate selective because metals are only deposited on substrate surfaces, where electron exchange occurs. This selectivity also leads to conformity of the coating by galvanic displacement regardless of the geometric complexity of the substrates.^{3,4} Additionally, in galvanic displacement,

metallic deposition can stop by itself when coating reaches its full surface coverage because electron supply from the substrate is blocked,¹ thus making mass production easier. With those advantages, there has been an increase in the use of galvanic displacement for nanofabrication in which metals, having distinct morphologies, were distributed randomly or with defined patterns on Si substrates.⁵⁻¹¹ Likewise, galvanic displacement was also used to deposit metals on 1D Si nanostructures.¹²⁻¹⁴ Then, the growth and interface characteristics of metals on underlying semiconductor substrates by galvanic displacement have served as important topics for fundamental studies.¹⁴⁻¹⁸ So far, a variety of metals has been deposited by galvanic displacement on Si and Ge substrates, including noble metals such as Au/Si,^{3,6,7,10,12,14-21} Au/Ge,^{3,8} Ag/Si,^{9,13,15,16,20,22} platinum-group metals such as Pt/Si,^{7,11,15,23} Pt/Ge,⁸ Pd/Ge,^{8,15} Pd/Si,¹⁵ Rh/Si,¹⁵ base metals such as Cu/Si,^{5,15,24-31} Ni/Si,²⁶ and several metals on III-V semiconductor substrates.¹

In galvanic displacement, the semiconductor substrate acts as an electron source via its surface oxidation. Likewise, metal ions in solution, taking up electrons supplied by the substrate, are reduced to metal atoms. Thus, the overall displacement process occurs when metals are deposited on the semiconductor substrate and the surface oxide is dissolved, as described by the following chemical equations:^{1,3}



where M denotes any metal whose standard redox potential is higher than that of hydrogen. The role of hydrofluoric acid (HF) is to maintain electron supply by dissolving the surface oxide. However, galvanic displacements of Nickel (Ni) and Cobalt (Co) do not occur at room

temperature and at the inherent pH of the precursor solutions because of their negative standard redox potentials. Thus, hydrogen evolution would dominate instead of the metallic deposition.³ In this work, we investigated the morphology and density of Ni and Co deposited on Silicon (Si) substrate by galvanic displacement at 80°C and pH 8 with respect to multiple deposition cycles. In addition, we also performed Ni and Co depositions with sodium dodecyl sulfate (SDS) and cetyltrimethylammonium bromide (CTAB) as additives to observe their effects on the deposited nanostructures. Non-precious metals have been used as electrocatalysts for oxygen evolution.^{27,28} Therefore, our samples were then tested for their performance in photoelectrochemical hydrogen generation. A variety of characterization methods was employed to assist our investigation. Scanning electron microscopy was used to determine morphology and density of the nanostructures. Information on the compositions of the deposits was obtained by energy dispersive x-ray spectroscopy. Finally, optical property of the nanostructures was recorded by UV-Vis spectroscopy.

Experimental Details

The chemicals used for metallic deposition included nickel(II) sulfate hexahydrate ($\text{NiSO}_4 \cdot 6\text{H}_2\text{O}$, $\geq 98\%$), cobalt(II) chloride hexahydrate ($\text{CoCl}_2 \cdot 6\text{H}_2\text{O}$, 98%), and cetyltrimethylammonium bromide ($\text{C}_{19}\text{H}_{42}\text{BrN}$, $\geq 99.9\%$) purchased from Sigma Aldrich (Milwaukee, WI, USA), and sodium dodecyl sulfate ($\text{C}_{12}\text{H}_{25}\text{NaO}_4\text{S}$, $\geq 99\%$) from Fisher Scientific (Pittsburgh, PA, USA), which were used as received. Ammonium hydroxide (NH_4OH , 28-30%), purchased from Fisher Scientific, was used to adjust the pH. Hydrofluoric acid (HF, 48-51%) was purchased from Thermal Fisher Scientific (Waltham, MA, USA). All solutions were prepared using deionized (DI) water. HF was contained in a polypropylene beaker for experimental use. The substrate was Si (100) wafer (4", single-crystalline, n-type, $\rho = 3\text{-}9 \text{ }\Omega\text{cm}$) purchased from El-Cat Inc. (Ridgefield Park, NJ, USA).

Before the deposition, Si wafer was cleaved into squared 1 cm x 1 cm² pieces. The chemicals used for cleaning Si substrate were acetone and ethanol (100%, 200 proof).

The deposition of Co and Ni on Si substrate followed a modified galvanic displacement method. Typically, Si substrate was first cleaned with acetone, followed by ethanol, then deionized water, each of which for 10 minutes, in an ultrasonic bath to degrease and de-contaminate the substrate. After that, the clean Si substrate was gently dried by Kimwipes. The deposition started by immersing Si substrate in a 10% (w/w) HF solution for 2 minutes to eliminate surface oxide and activate the surface. The Si substrate was instantly immersed for 5 minutes in 0.10 M NiSO₄ or CoCl₂, adjusted to pH 8 by addition of NH₄OH, for Ni and Co deposition, respectively. Prior to immersing Si substrate, the metallic solution was heated to 80°C and maintained at this temperature using an oil bath placed on a hot plate. After that, the sample was rinsed thoroughly with deionized water. For multi-cycle depositions, each cycle of HF etching, metallic deposition, and rinsing was repeated multiple times. For experiments with surfactants, the metallic solution was composed of 0.03 M sodium dodecyl sulfate or cetyltrimethylammonium bromide mixed with 0.10 M NiSO₄ or CoCl₂, which was also adjusted to pH 8 by NH₄OH. Finally, Co- or Ni-deposited Si sample was gently dried by Kimwipes and stored in a square polystyrene box for further characterization.

The size and morphology of the nanostructures were studied by scanning electron microscopy (SEM) using a FEI Quanta-250 SEM instrument at 10 kV accelerating voltage. The SEM instrument was equipped with an Oxford Aztec energy dispersive x-ray (EDX) analysis system, which was used to conduct elemental analyses of the deposited nanostructures. UV-Vis absorption spectroscopy was recorded by a Perkin Elmer Lambda 25

spectrophotometer. To prepare samples for UV-Vis measurements, each sample was immersed in 1 mL DI water and sonicated at the highest power for 1-3 minutes to detach the metallic nanostructures from Si substrate and disperse them in DI water.

Results and Discussion

Figure 5.1 and Figure 5.2 show that Ni and Co appeared as small particles with increasing density as the number of deposition cycles increased. On the other hand, SDS and CTAB hindered particle growth. An exception occurred when CTAB was used as additive in the galvanic displacement of Co in which Co appeared as large and elongated nanostructures at low density. Chemical compositions of the as-synthesized samples were also determined by EDX. The Ni or Co peaks were observed for each respective metal-deposited sample, indicating the formation of Ni and CO via galvanic displacement technique purity. A very strong Si peak was obtained from the substrate. The C and Cl peaks were detected due to

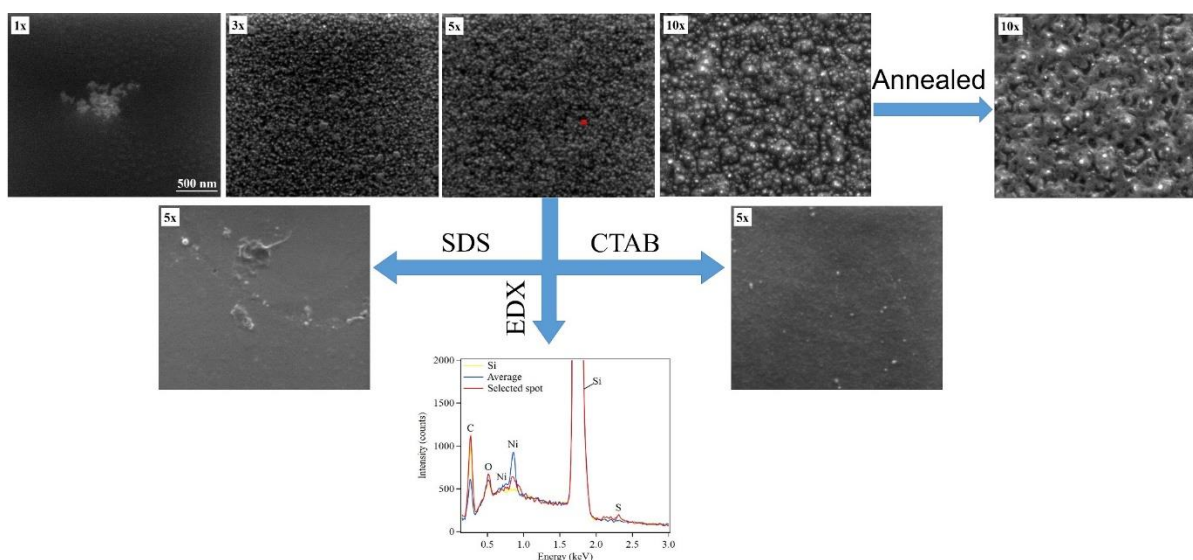


Figure 5.1 SEM images showing the morphology and density of Ni nanostructures deposited on Si substrate by galvanic displacement after multiple deposition cycles (1x - 10x), after being annealed at 100°C for 30 minutes, and after the use of additives. The EDX spectrum showing the elemental composition of the sample surface.

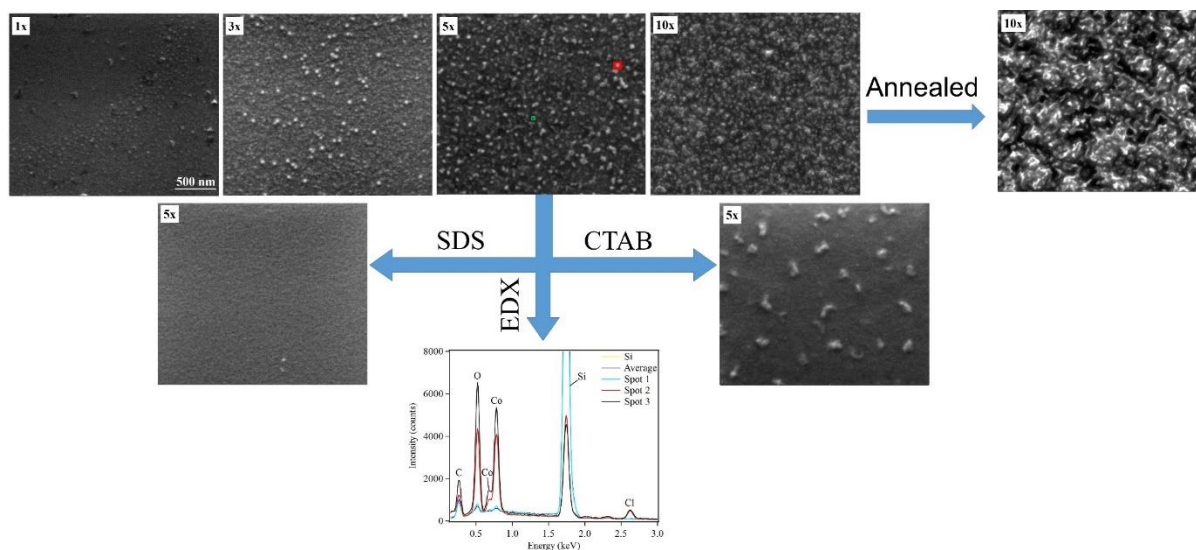


Figure 5.2 SEM images showing the morphology and density of Co nanostructures deposited on Si substrate by galvanic displacement after multiple deposition cycles (1x - 10x), after being annealed at 100oC for 30 minutes, and after the use of additives. The EDX spectrum showing the elemental composition of the sample surface.

possible organic contaminants due to the SEM vacuum chamber and the ligand from the metallic precursor, while O peak could be a result of the oxidation of the surface.

To obtain data on optical property of Ni and Co nanostructures, UV-Vis absorption spectrum was recorded for each metal and shown in Figure 5.3. No noticeable absorption band was identified in the visible region for both Co and Ni nanostructures, whereas two weak and broad absorption bands were observed for both metals in the ultraviolet region at ~200 and ~320 nm. These absorption bands indicated the presence of Ni and Co nanostructures.²⁹⁻³¹

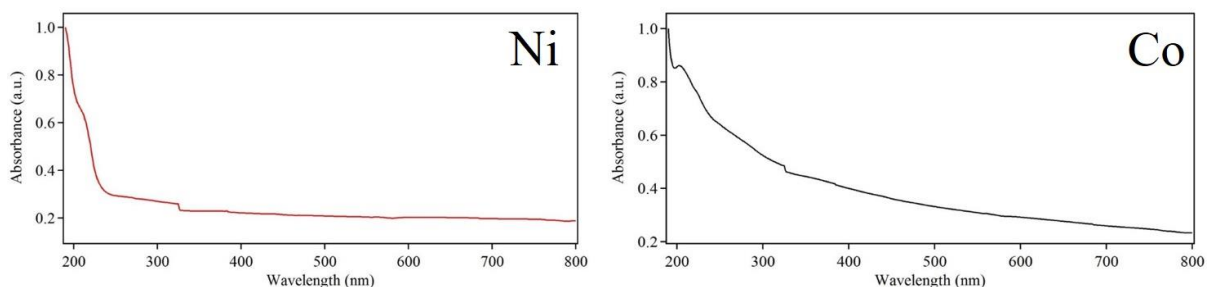


Figure 5.3 Normalized UV-Vis spectra of Ni and Co showing characteristic peaks and increasing absorption toward shorter wavelengths

Conclusion

In summary, this work described the deposition of Co and Ni on n-type Si substrate using galvanic displacement method at 80°C and pH 8. To gain control of the growth and density of the metallic nanostructures, certain numbers of cyclic depositions were performed with limited use of HF etchant. Then, the resulting samples were characterized and analyzed. An increase in density and size of the metallic nanostructures as well as an increase in surface roughness of the Si substrate were observed for both Co and Ni when the number of deposition cycles increased. Upon annealing, surface morphology of the samples underwent transformation whereas the presence of additives hindered deposition. Some selected Co and Ni samples were used to investigate their applicability for photoelectrochemical production of hydrogen and results will be published elsewhere.

References

1. Carraro, C.; Maboudian, R.; Magagnin, L. *Surface Science Reports* **2007**, *62* (12), 499-525.
2. Ali, H. O.; Christie, I. R. A. *Gold Bull.* **1984**, *17* (4), 118-127.

3. Magagnin, L.; Maboudian, R.; Carraro, C. *Journal of Physical Chemistry B* **2002**, *106* (2), 401-407.
4. Cerruti, M.; Doerk, G.; Hernandez, G.; Carraro, C.; Maboudian, R. *Langmuir* **2010**, *26* (1), 432-437.
5. Lee, Y.; Tsai, M.; Hu, T.; Dai, B.; Feng, M. *Electrochemical and Solid State Letters* **2001**, *4* (7), C47-C49.
6. Zhang, X.; Qiao, Y.; Xu, L.; Buriak, L. *Acs Nano* **2011**, *5* (6), 5015-5024.
7. Fabre, B.; Hennous, L.; Ababou-Girard, S.; Meriadec, C. *Acs Applied Materials & Interfaces* **2013**, *5* (2), 338-343.
8. Porter, L.; Choi, H.; Schmeltzer, J.; Ribbe, A.; Elliott, L.; Buriak, J. *Nano Letters* **2002**, *2* (12), 1369-1372.
9. Liu, F.; Green, M. *Journal of Materials Chemistry* **2004**, *14* (10), 1526-1532.
10. Lahiri, A.; Wen, R.; Kuimalee, S.; Kobayashi, S.; Park, H. *Crystengcomm* **2012**, *14* (4), 1241-1246.

11. Kawasaki, H.; Yao, T.; Suganuma, T.; Okumura, K.; Iwaki, Y.; Yonezawa, T.; Kikuchi, T.; Arakawa, R. *Chemistry-a European Journal* **2010**, *16* (35), 10832-10843.
12. Yang, X.; Zhong, H.; Zhu, Y.; Shen, J.; Li, C. *Dalton Transactions* **2013**, *42* (39), 14324-14330.
13. Huang, J.; Chen, F.; Zhang, Q.; Zhan, Y.; Ma, D.; Xu, K.; Zhao, Y. *Acs Applied Materials & Interfaces* **2015**, *7* (10), 5725-5735.
14. Sayed, S.; Wang, F.; Malac, M.; Li, P.; Wang, D.; Buriak, J. *Crystengcomm* **2012**, *14* (16), 5230-5234.
15. Yae, S.; Nasu, N.; Matsumoto, K.; Hagihara, T.; Fukumuro, N.; Matsuda, H. *Electrochimica Acta* **2007**, *53* (1), 35-41.
16. Peng, K.; Zhu, J. *Electrochimica Acta* **2004**, *49* (16), 2563-2568.
17. Sayed, S.; Wang, F.; Mallac, M.; Meldrum, A.; Egerton, R.; Buriak, J. *Acs Nano* **2009**, *3* (9), 2809-2817.
18. Warren, S.; Reitzle, A.; Kazimirov, A.; Ziegler, J.; Bunk, O.; Cao, L.; Renner, F.; Kolb, D.; Bedzyk, M.; Zegenhagen, J. *Surface Science* **2002**, *496* (3), 287-298.

19. Gutes, A.; Carraro, C.; Maboudian, R. *Acs Applied Materials & Interfaces* **2011**, *3* (5), 1581-1584.
20. Aizawa, M.; Buriak, J. *Journal of the American Chemical Society* **2006**, *128* (17), 5877-5886.
21. Rossiter, C.; Suni, I. *Surface Science* **1999**, *430* (1-3), L553-L557.
22. Hochbaum, A.; Chen, R.; Delgado, R.; Liang, W.; Garnett, E.; Najarian, M.; Majumdar, A.; Yang, P. *Nature* **2008**, *451* (7175), 163-U5.
23. Gorostiza, P.; Allongue, P.; Diaz, R.; Morante, J.; Sanz, F. *Journal of Physical Chemistry B* **2003**, *107* (26), 6454-6461.
24. Cho, J. S. H.; Kang, H. K.; Wong, S. S.; Shachamdiamand, Y. *Mrs Bulletin* **1993**, *18* (6), 31-38.
25. Darosa, C.; Iglesia, E.; Maboudian, R. *Journal of the Electrochemical Society* **2008**, *155* (3), D244-D250.
26. Zhang, Y.; Ang, S.; Tay, A.; Xu, D.; Kang, E.; Neoh, K.; Chong, L.; Huan, A. *Langmuir* **2003**, *19* (17), 6802-6806.

27. Yang, J.; Walczak, K.; Anzenberg, E.; Toma, F.; Yuan, G.; Beeman, J.; Schwartzberg, A.; Lin, Y.; Hettick, M.; Javey, A.; Ager, J.; Yano, J.; Frei, H.; Sharp, I. *Journal of the American Chemical Society* **2014**, *136* (17), 6191-619428.
28. Kenney, M.; Gong, M.; Li, Y.; Wu, J.; Feng, J.; Lanza, M.; Dai, H. *Science* **2013**, *342* (6160), 836-840.
29. Athar, T.; Hakeem, A.; Topnani, N.; Hashmi, A. *International Scholarly Research Network Materials Science* **2012**, *5*.
30. Mohan, S.; Srivastava, P.; Maheshwari, S.; Sundar, S.; Prakash, R. *Analyst* **2011**, *136* (13), 2845-2851.
31. Wang, J.; Wei, L.; Zhang, L.; Jiang, C.; Kong, E.; Zhang, Y. *Journal of Materials Chemistry* **2012**, *22* (17), 8327-8335.

CHAPTER 6. ELECTRODEPOSITION OF GOLD NANOSTRUCTURES HAVING CONTROL MORPHOLOGY

Minh Tran¹, Colton Mundt², Tian Lan¹, and Sonal Padalkar,^{1, 3*}

1. Department of Mechanical Engineering, Iowa State University, Ames, IA 50011,
USA

2. Department of Aerospace Engineering, Iowa State University, Ames, IA 50011,
USA

3. Microelectronics Research Center, Iowa State University, Ames, IA 50011, USA

* Corresponding author Email: padalkar@iastate.edu

Abstract

Gold (Au) nanostructures exhibit several unique electronic, optoelectronic and plasmonic properties. This makes them potential candidates for applications in areas including biosensing, catalysis, optics, and electronics. These unique properties are governed by the precise control over their morphologies and size. The present work investigates the electrodeposition process of Au nanostructures. Additionally, the influence of applied potential, electrolyte pH and presence of L-cysteine on the morphology, size, distribution and density of Au nanostructured was studied. The observations elucidated the relationship between the process parameters and the formation mechanism of the Au nanostructures. The morphology and composition of these Au nanostructures were characterized by scanning electron microscopy and X-ray diffraction respectively.

Introduction

Gold (Au) nanostructures have attracted much attention in the past decade due to their unique physical, chemical, electronic, optoelectronic, catalytic and plasmonic properties compared to its bulk counterpart. The Au nanostructures also exhibit excellent conductivity

and electrochemical activity. The reduction in the size of the material to the nanometer range improves the aforementioned properties. Thus making the Au nanostructures potential candidates for diverse applications ranging from biosensing to catalysis [1-11].

The unique properties of Au nanostructures are strongly governed by their size and morphology. The surface plasmon properties of Au nanoparticles can be easily tuned over the entire visible spectrum by varying the size and morphology of the Au nanoparticles. Jain and co-workers have calculated absorption and scattering efficiencies and optical resonance wavelengths of Au nanoparticles [12]. A large variation in optical properties were demonstrated with the changes in the dimensions of the Au nanoparticles. It was concluded that the extinction cross-section increased and the ratio of scattering to extinction cross-section decreased with increase in the Au nanostructures. Further, Sakai and co-workers correlated the absorption and scattering properties of Au nanostructures to their morphologies [13]. These Au nanostructures were electrodeposited on indium doped tin oxide (ITO). Various Au nanostructures were analyzed in this study indicating a red shift in the absorption wavelength with increase in size. Additionally, with increase in size of the Au nanostructures the scattering contribution also increased. In another study, Kozanoglu and co-workers utilized Au nanostars to improve power conversion efficiency by 29% [14]. Furthermore, Rodríguez-Lorenzo et al demonstrated lowering of the detection limit in biosensors by using Au nanostars [15]. In this work a cancer biomarker was detected down to 4×10^{-20} M by the use of Au nanostars. Thus various Au nanostructures can find potential applications particularly in sensing and solar energy related areas.

In the last decade there have been a large number of publications based on Au nanostructure synthesis. Many of these synthesis techniques have been solution based [16-

18]. Synthesis methods of Turkevich and Brust-Schiffrin have been the most popular since a good control over the final particle size and distribution was possible by varying the processing conditions [18]. In the Turkevich method, Au precursor is mixed with citrate, which serves as reducing agent and a stabilizer. The reaction is carried out in water at a temperature of 100 °C. The citrate to gold precursor ratio plays an important role in governing the size of the Au nanoparticles [18]. The Brust-Schiffrin method uses an organic solvent. In this method the gold precursor is mixed with sodium borohydride and alkylthiol. This method produced Au nanoparticles that are cuboctahedral or icosahedral with size of 2 – 5 nm. In other solution based synthesis, surfactants including cetyltrimethylammonium bromide (CTAB) are often used [19]. Thus shape control synthesis is possible with the use of surfactants, which include the formation of nanoparticles, nanorods, nanocubes, nanostars etc. However, the solution based synthesis has some drawbacks including the precise control of synthesis temperature and long reaction times. These synthesis methods often suffer from poor dispersity of Au nanostructures. In some cases, the synthesis needs to be conducted in an inert environment. Moreover, the synthesized nanostructures have to be integrated with substrates for many application, which adds an extra step to the fabrication process.

Electrodeposition, in contrast to the solution based method, is a popular technique for the deposition of Au nanoparticles without the presence of any capping agents [13, 20-21]. The Au nanoparticles are directly deposited on a conducting or semiconducting substrate, which is advantageous over the solution based technique. Additionally, this deposition method provides easy attachment of the nanoparticles on to the substrate. The morphology and size of the depositing nanostructures can be controlled by varying the process parameters. Electrodeposition can also be utilized for the deposition of various materials

including metals and their oxides with desired size, morphology and crystallographic orientation. Furthermore, electrodeposition is a simple, inexpensive and scalable technique for the deposition of various nanostructures.

In this work, we investigate the changes in size, density and morphology of electrodeposited Au nanostructures as a function of applied potential, electrolytic pH and presence of chemical additives like L-cysteine in the electrolyte. The Au nanostructures were characterized by scanning electron microscopy (SEM) and X-ray diffraction (XRD). A relation between the process parameters and the resulting Au nanostructures was established.

Experimental Details

Gold (III) chloride trihydrate ($\text{HAuCl}_4 \cdot 3\text{H}_2\text{O}$, $\geq 99.9\%$) was purchased from Sigma-Aldrich (Milwaukee, WI, USA). L-Cysteine ($\text{C}_3\text{H}_7\text{NO}_2\text{S}$, $\geq 98\%$) was purchased from EMD Millipore (Billerica, MA, USA). The chemicals were used without further purification. Indium doped tin oxide (ITO)-coated glass substrate was purchased from University Wafer. The square ITO substrate (25 mm x 25 mm) had a resistivity of 7 ohm/sq. The electrodeposition was carried out using a CH Instruments, CHI601E electrochemical analyzer. The Au nanostructure morphologies were studied by scanning electron microscopy (SEM) using a FEI Quanta-250 SEM instrument operating at 10 kV accelerating voltage. To investigate the composition and crystallinity of the electrodeposited Au nanostructures, X-ray diffraction (XRD) technique was used, which was a Siemens D500 instrument.

A typical electrodeposition setup consists of an electrochemical cell (Figure 6.1a), consisting of a working, counter and reference electrode. In the present study, ITO coated glass substrate was the working electrode (Figure 6.1b). A 2 mm diameter platinum wire served as the counter electrode (Figure 6.1c), and an Ag/AgCl wire was the reference electrode (Figure 6.1d). Prior to electrodeposition, the ITO substrate was sonicated in a bath

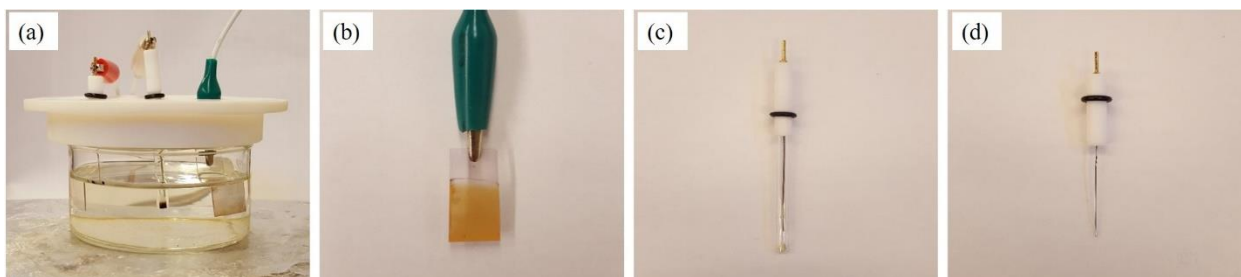


Figure 6.1 Photographs of an (a) electrodeposition setup, consisting of a (b) working, (c) reference, and (d) counter electrode.

of acetone for 10 minutes using a Branson 3800 ultrasonic cleaner. Further, the ITO substrate was cleaned using hydrochloric acid (HCl) and nitric acid (HNO₃) sequentially for 2 minutes. The ITO substrate was rinsed with pure distilled water between every cleaning step. The electrolyte solution was prepared in a 100 mL beaker by dissolving the Au precursor. The pH of the electrolyte was adjusted to either 3 or 8 by using HCl and sodium hydroxide (NaOH). L-cysteine was added after the final pH was achieved. All experiments were carried out at room temperature (25°C). The electrodeposition reaction time of 30 min was utilized for all Au nanostructure samples.

Results and Discussions

The Au nanostructures were electrodeposited at ambient conditions. The process parameters including applied potential, pH of the electrolyte and the L-cysteine concentration were varied and the outcomes were recorded. Table 6.1 gives detailed process parameter variations. Briefly, the applied potential is varied between -0.4 to -0.8V. The pH of the electrolyte was either 3 or 8. The concentration of L-cysteine was varied between 0 to 0.3 mM.

Table 6.1 *The process parameters varied in the present study for the electrodeposition Au nanostructures.*

Potential (V)	pH		L-Cysteine conc. (mM)		
-0.4	3	8	0	0.1	0.3
-0.6	3	8	0	0.1	0.3
-0.8	3	8	0	0.1	0.3

Influence of the applied potential on Au nanostructure morphology

It has been demonstrated, in literature, that electrodeposition of gold occurs by nucleation and growth of the deposited nuclei [13]. The applied external potential strongly influences the morphology of the deposited Au nanostructures. Figure 6.2 shows SEM images of Au nanostructures electrodeposited at varying applied potential of -0.4, -0.6 and -0.8 V. These Au nanostructures were deposited by keeping all other process parameters identical along with the electrolyte pH of 3. From the SEM images it is clear that the size of the deposited gold decreases with increase in the negative potential. The Au nanostructures appear elongated and faceted at an applied potential of -0.4 V. With increase in the negative potential they appear quasi-spherical, with some faceted nanostructures. Thus with change in potential from -0.4 V to -0.8 V, the morphology changed from being rough to smooth. Additionally, the number density of the Au nanostructures increased drastically from -0.4 V to -0.8 V. The sample with an applied potential of -0.8 V appeared very dense with further deposition of gold forming a sub-monolayer overlay. The inset of Figure 6.2 shows photographs of samples prepared at varying applied potential. The sample fabricated with an applied potential of -0.4 V was dark golden in color with a dull appearance. Whereas the

samples fabricated at -0.6 V and -0.8 V appeared bright golden in color and had a lustrous appearance. The variations in the appearance of these samples indicates changes in their absorption properties. Thus, from Figure 6.2 it is clear that variation in the applied potential can influence the size, number density and optical properties of the fabricated Au nanostructures.

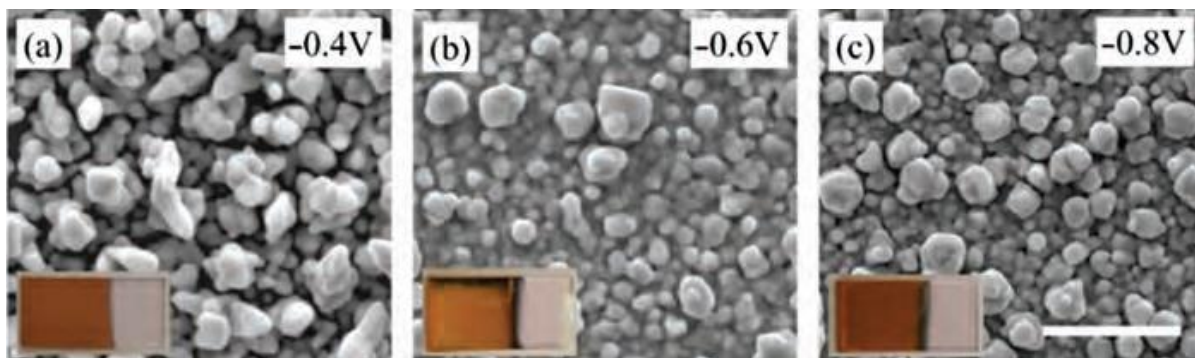


Figure 6.2 SEM images of Au nanostructures electrodeposited, with a pH of 3, at -0.4 V (a), -0.6 V (b) and -0.8 V (c). The scale bar is $1\text{ }\mu\text{m}$.

These variations in the deposited Au nanostructures can be explained with the help of the formation mechanism that is influenced by the applied potential. As mentioned above, the deposition occurs via nucleation and growth [13]. When the applied potential is lowered to a more negative value the subsequent current density for electrodeposition increases, leading to an increase in the number of nuclei formed in the initial stage of the deposition process [13, 22]. This initial number of nuclei govern the resulting size and density of the deposited nanostructures. The large number of initial nuclei cause the resulting nanostructure size to be small and thus denser. Additionally, the size and density changes affect the absorption properties. The large and rough Au nanostructures formed at -0.4 V result in a dull appearance due to scattering effects of the incident light from the rough Au nanostructures [13]. The other Au nanostructures formed at -0.6 V and -0.8 V appear bright and glossy due to the occurrence of less light scattering events, as the deposited nanostructures are dense and

smooth. Further in this investigation, the pH value of the electrolyte was varied from pH 3 to 8. The effects of electrolyte pH variation are discussed in the following section.

Influence of pH variation on the Au nanostructure morphology

From our investigation, it is observed that the pH value of the electrolyte significantly affects the morphology of the deposited Au nanostructures. Figure 6.3 shows the SEM

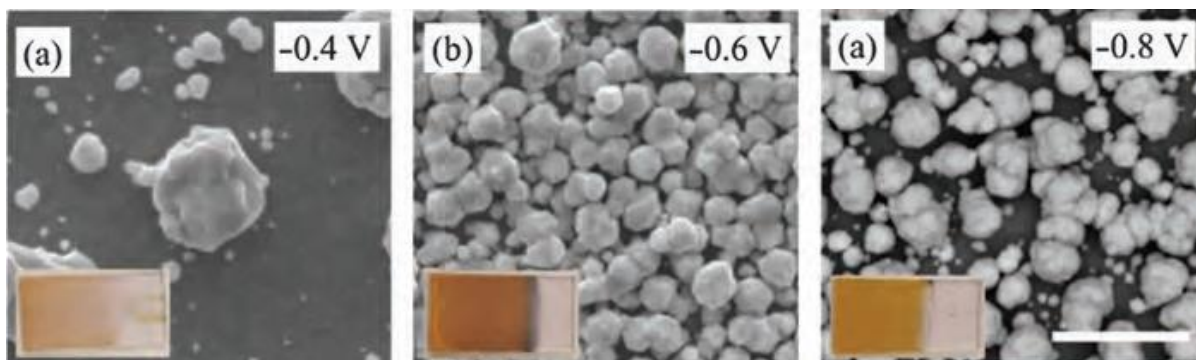


Figure 6.3 SEM images of Au nanostructures electrodeposited, with a pH of 8, at -0.4 V (a), -0.6 V (b) and -0.8 V (c). The scale bar is 1 μm .

images of Au nanostructures deposited at varying potentials of -0.4 V, -0.6 V and -0.8 V at an electrolyte pH of 8. These SEM images were compared with the corresponding images, having similar applied potentials, in Figure 6.2. From this comparison it is evident that for samples fabricated at -0.4 V at acidic and basic electrolyte pH, the nanostructure size, density and morphology considerably varied. At basic pH the Au nanostructures appeared more spherical in shape and comprised of facets. Additionally, the average particle size and the size distribution was large. The deposited nanostructures had sparse density, thus many areas of the substrate remained exposed. Furthermore, for Au nanostructures fabricated at -0.6 V and -0.8 V under basic conditions, showed similar trends as that of the sample fabricated at -0.4 V. The inset in Figure 6.2 shows photographs of the fabricated Au nanostructures. The sample prepared at -0.4 V with a basic electrolyte, shows a thin deposited layer indicating a

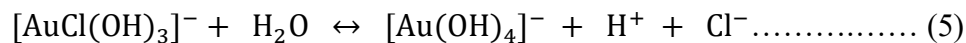
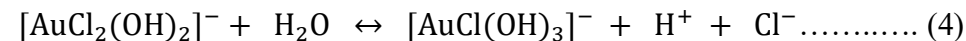
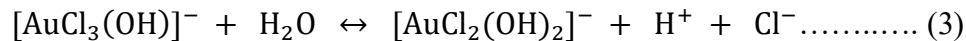
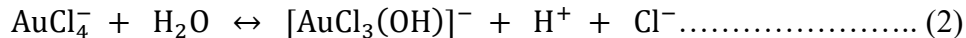
sparse deposition. Similarly, the samples prepared at -0.6 V and -0.8 V also showed thin deposited layers with light golden color.

These observations can be explained with the help of the gold complex formations, followed by their reactivity and stability. The gold precursor (HAuCl₄), when dissolved in water readily hydrolyzes. When the electrolytic pH was 3 the color of the electrolyte appeared yellow, while at basic pH of 8 the electrolyte became colorless. This change in electrolyte color was attributed to the varying degree of hydrolysis of AuCl₄⁻ complex [23-24]. It has been noted in literature that the electrolyte at pH 3 may contain different Au complexes including AuCl₄⁻, [AuCl₃(OH)]⁻, and [AuCl₂(OH)₂]⁻. The electrolyte at pH 8 may contain [AuCl(OH)₃]⁻ and [Au(OH)₄]⁻ complexes. The following chemical reactions describe the hydrolysis process.

Dissolution of HAuCl₄ in water:



Hydrolysis of AuCl₄⁻:



The reactivity of Au(III) complex is strongly influenced by the electronegativity of the ligand donor. The lower electronegativity of the ligand donor leads to a less reactive gold complex [23]. During hydrolysis, when Cl ligands were replaced by OH ligands, the resulting Au complex became less reactive. Thus, upon increasing the electrolytic pH to 8, the rate of Au deposition decreased due to the increased stability of Au(III) complexes. This led to the

decrease in the nucleation rate of Au, which resulted in a lower number of nuclei and sparse density of the Au nanostructures. Unlike the nucleation and growth process that occurred when the electrolyte was acidic, the lower deposition rate due to basic conditions led to the occurrence of nucleation throughout the deposition process, which resulted in polydispersed nanostructures [25-29]. Additionally, the reduction of AuCl_4^- would preferentially nucleate on the existing Au surfaces rather than the bare ITO substrate [13]. Thus a significant difference in the size, distribution, density and morphology of the Au nanostructures was observed between the acidic and basic electrolytic conditions. Further in this investigation, the effects of L-cysteine on Au nanostructure morphology was studied.

Influence of L-cysteine on the Au nanostructure morphology

The presence of L-cysteine in the electrolyte during electrodeposition has a significant influence on the morphology of the Au nanostructures. L-cysteine is commonly used in solution based synthesis of Au nanoparticles, as a stabilizer and a morphology modifying agent as it adsorbs on specific metal planes mainly by the thiol (-SH) group [13, 30-34]. The L-cysteine adsorbs on low index planes, including (110), (100) and (111), of Au nanostructures and can be selectively desorbed by the application of appropriate potential during electrodeposition [13, 21, 35].

The Au nanostructures deposited in the presence of 0.1 mM L-cysteine, at varying potentials and pH values of the electrolyte are shown in Figure 6.4. The SEM image in Figure 6.4 (a) clearly show dendritic structures of Au formed at potential -0.4 and pH of 3. The SEM images in 4 (b) and 4 (c) showed a decrease in particle size and increase in density of the Au nanostructures. The decrease in size appeared to be greater than the samples fabricated in the absence of L-cysteine. Additionally, no dendritic structures were observed

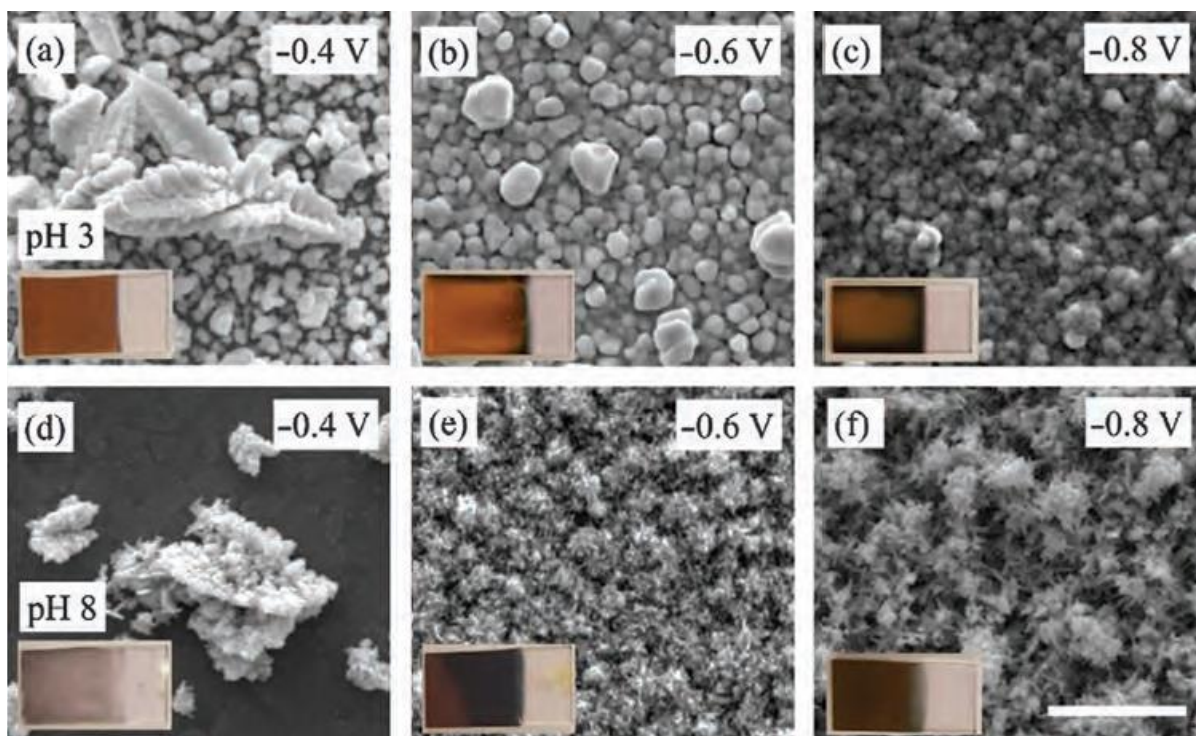


Figure 6.4 SEM images of Au nanostructures electrodeposited using 0.1 mM L-cysteine at varying potentials of -0.4 V, -0.6 V and -0.8 V at pH 3 (a-c) and at pH 8 (d-f). The scale in samples fabricated at -0.6 V and -0.8 V with 0.1 mM L-cysteine. However, when the electrolytic pH was increased to 8, nanoparticles with random shapes and sizes were formed having rough, need like nanostructures covering their entire surfaces as seen in Figure 6.4 (d), Figure 6.4 (e) and Figure 6.4 (f). The nanostructure size was large at the applied potential of -0.4 V. The samples fabricated at -0.6 V and -0.8 V appeared to have smaller average particle size and higher density when compared to the sample fabricated at -0.4 V. However, samples at pH 8 have lower density than the samples fabricated with an electrolytic pH of 3 as this is evident from the exposed substrates in all these samples. The insets in Figure 6.4 (a), Figure 6.4 (b) and Figure 6.4 (c) shows photographs of the fabricated samples. These photographs suggest a thick film indicating a high deposition rate. Further, the sample in Figure 6.4 (a) had a dull appearance, whereas samples in Figure 6.4 (b) and Figure 6.4 (c)

had a lustrous appearance. The photographs of samples deposited at a pH of 8 appeared thin and dark golden or even black in color.

The next step in this investigation was to increase the concentration of the L-cysteine to 0.3 mM in the electrolyte and observe any changes in size, density and morphology of the fabricated Au nanostructures. The SEM images in the Figure 6.5 shows Au nanostructures

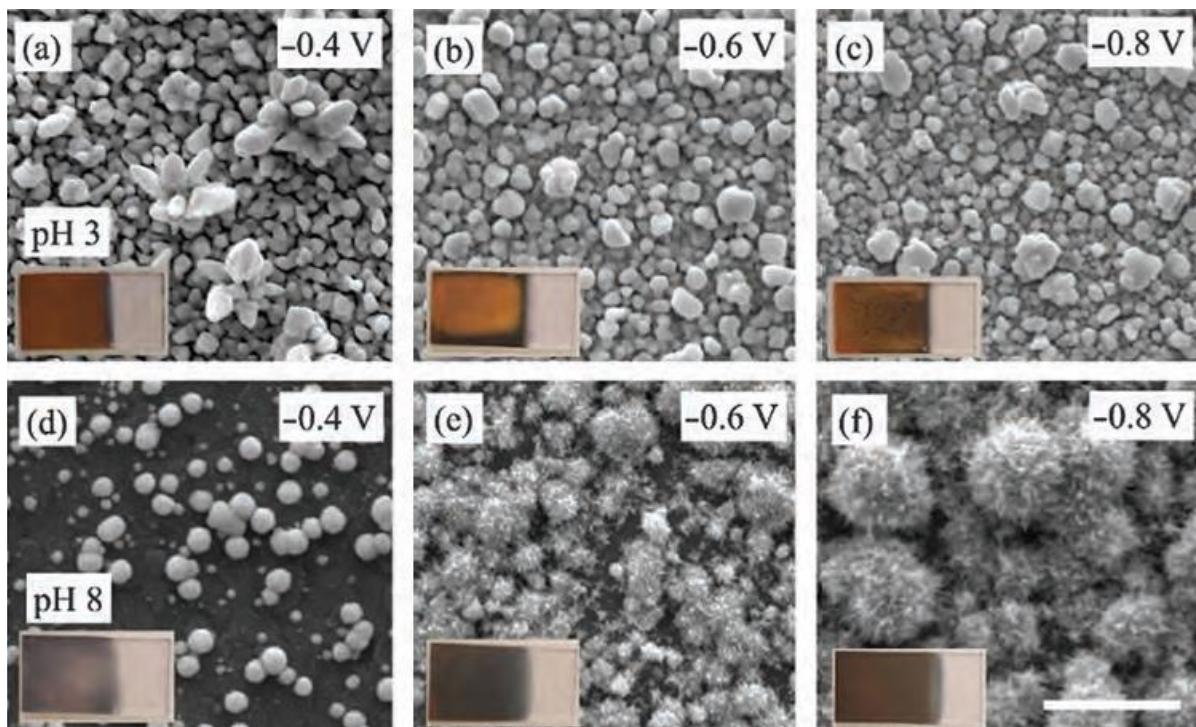


Figure 6.5 SEM images of Au nanostructures electrodeposited using 0.3 mM L-cysteine at varying potentials of -0.4 V, -0.6 V and -0.8 V at pH 3 (a-c) and at pH 8 (d-f). The scale bar is 1 μ m.

fabricated at varying applied potentials and pH values. The SEM image in Figure 6.5 (a) shows dendritic structures formed at a potential of -0.4 V with a pH of 3 and in the presence of 0.3 mM L-cysteine. These dendritic structures appear smaller in size compared to a similar sample with lower L-cysteine concentration (Figure 6.4 (a)). The other samples fabricated at pH 3 with applied potential of -0.6 V and -0.8 V showed smaller particle size, higher density and no dendritic structures. When the electrolytic pH was increased to 8, all samples

exhibited large particles size with rough, needlelike structures covering the surfaces.

Additionally, the particle size increased as the applied potential increased from -0.4 V to -0.8 V. The insets in Figure 6.5 (a), 5 (b) and 5 (c) shows photographs of the samples prepared at pH 3. These photographs show thick film indicating a high deposition rate. Additionally, the sample in Figure 6.5 (a) had a dull appearance, while the samples in Figure 6.5 (b) and Figure 6.5 (c) had a glossy appearance. The photographs of samples deposited at a pH 8 appeared thin and dark golden or black in color

The SEM images in Figure 6.4 and Figure 6.5 indicate a strong interplay between the process parameters including applied potential, pH of electrolyte and L-cysteine concentration. It is clear that the morphology of the Au nanostructures was significantly influenced by the presence of L-cysteine. It is also known from the literature the L-cysteine adsorbs on low index planes of gold and is sensitive to desorption at particular applied potentials during electrodeposition [13, 21, 35]. The dendritic structures in Figure 6.4 (a) and Figure 6.5 (a) are mainly due to the adsorption of L-cysteine on (100) and (110) planes of Au nanostructures, leading to the deposition of Au on (111) facets [13, 35]. With the increase in the applied potential at pH 3, the morphology appeared to be quasi-spherical and highly compact. This can be attributed to the very high deposition rate. When the pH of the electrolyte was increased to 8 the morphology of the Au nanostructures had a rough appearance with need like structures covering the entire Au surface. The formation of the needle like structures is attributed to the adsorption of L-cysteine on Au facets. Additionally, the very slow deposition process due to pH 8 has contributed to the needle like morphology of Au nanostructures, since the gold ions could reduce on a preferred Au facets in a timely manner.

Furthermore, the insets showing Au nanostructures fabricated with a pH 3 have dark golden color and thick layers. These appearances are due to the high deposition rate with very little change in the morphology of the Au nanostructures. On the contrary, the insets showing Au nanostructures fabricated at pH 8 have a black appearance with very thin layers. This has been attributed to the very low deposition rate that has resulted in significant morphology change. The dark color also indicates substantial changes in light absorption properties compared to the samples prepared in the acidic electrolyte. The size, density and morphology of the Au nanostructures is strongly dependent on the applied potential, electrolytic pH and L-cysteine concentration. It is challenging to deconvolve the individual effects of these process parameters. However, our future work will systematically study the individual effects of the process parameters on size, density and morphology.

The Au nanostructures were analyzed using X-ray diffraction. The XRD plots, shown in Figure 6.6, are typical plots obtained from samples fabricated at an applied potential of -

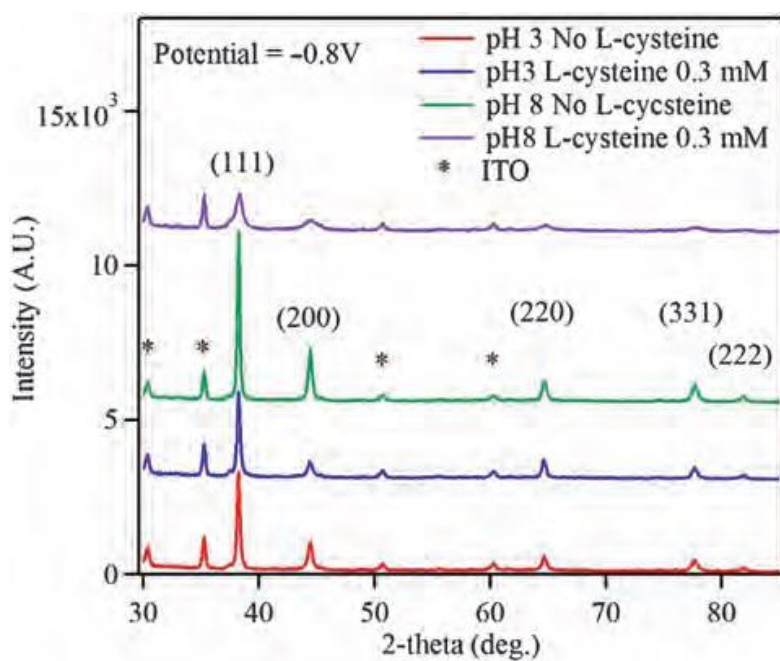


Figure 6.6 XRD plots of Au nanostructures fabricated at an applied potential of -0.8 V, with varying pH and L-cysteine concentrations

0.8 V, with varying electrolytic pH values and in the presence and absence of L-cysteine. The XRD plots indicate that the crystalline structures of the Au nanostructures are of face-centered cubic (fcc) Au [21]. The strong peak centered at $2\theta = 38.3^\circ$ is indexed to be Au (111) crystal plane [21]. From the XRD plots it is clear that the Au (111) crystal facet is dominant in all the electrodeposited samples.

Conclusion

In summary, successful electrodeposition of Au nanostructures was carried out under varying process conditions including applied potential, electrolytic pH and the presence of L-cysteine. From our investigation, it is clear that with increase in the applied potential the deposition rate increases leading to the reduction in the particle size and increase in density of the deposited Au nanostructures. It was also noticed that electrolytic pH played a dominant role in the fabrication of the Au nanostructures. With the increase in pH from 3 to 8 the deposition rate decreased leading to very thin deposited layers. Additionally, the deposited nanostructures were larger and less dense at pH 8. The presence of L-cysteine strongly influences the morphology of the deposited Au nanostructures, producing dendritic structures especially with an electrolytic pH of 8. An overlayer of Cu₂O was successfully electrodeposited on the Au nanostructures. The PEC measurements of the Cu₂O control photocathode and the Au-Cu₂O composite photocathodes were performed, which is presented in our publication.

References

1. S. Unser, I. Bruzas, J. He, and L. Sagle, *Sensors* 15, 7 (2015).

2. J. Cao, T. Sun, and K. T. V. Grattan, *Sensors and Actuators B-Chemical* 195, 332 (2014).
3. V. Biju, *Chemical Society Reviews* 43, 3 (2014).
4. G. Doria, J. Conde, B. Veigas, L. Giestas, C. Almeida, M. Assuncao, J. Rosa, and P. V. Baptista, *Sensors* 12, 2 (2012).
5. S. W. Zeng, K. T. Yong, I. Roy, X. Q. Dinh, X. Yu, and F. Luan, *Plasmonics* 6, 3 (2011).
6. S. Linic, U. Aslam, C. Boerigter, and M. Morabito, *Nature Materials* 14, 6 (2015).
7. N. Zhou, V. Lopez-Puente, Q. Wang, L. Polavarapu, I. Pastoriza-Santos, and Q. H. Xu, *Rsc Advances* 5, 37 (2015).
8. W. B. Hou, and S. B. Cronin, *Advanced Functional Materials* 23, 13 (2013).
9. X. M. Zhang, Y. L. Chen, R. S. Liu, and D. P. Tsai, *Reports on Progress in Physics* 76, 4 (2013).
10. S. Sarina, E. R. Waclawik, and H. Y. Zhu, *Green Chemistry* 15, 7 (2013).

11. H. S. N. (Editor), *Encyclopedia of Nanoscience and Nanotechnology*. American Scientific Publishers, : Los Angeles, CA, **2004**; Vol. 1-10.
12. P. Jain, K. Lee, I. El-Sayed, and M. El-Sayed, *Journal of Physical Chemistry B* 110, 14 (**2006**).
13. N. Sakai, Y. Fujiwara, M. Arai, K. Yu, and T. Tatsuma, *Journal of Electroanalytical Chemistry* 628, 1-2 (**2009**).
14. D. Kozanoglu, D. Apaydin, A. Cirpan, and E. Esenturk, *Organic Electronics* 14, 7 (**2013**).
15. L. Rodríguez-Lorenzo, R. De La Rica, R. A. Álvarez-Puebla, L. M. Liz-Marzán, and M. M. Stevens, *Nat Mater* 11, 7 (**2012**).
16. Y. Xia, Y. Xiong, B. Lim, and S. Skrabalak, *Angewandte Chemie-International Edition* 48, 1 (**2009**).
17. P. Zhao, N. Li, and D. Astruc, *Coordination Chemistry Reviews* 257, 3-4 (**2013**).
18. T. Minh, D. Rebekah, T. Madeline, and P. Sonal, *Materials Research Express* 3, 10 (**2016**).

19. N. Jana, L. Gearheart, and C. Murphy, *Journal of Physical Chemistry B* 105, 19 (2001).
20. L. Wu, X. Zhang, and J. Chen, *Journal of Electroanalytical Chemistry* 726, 112 (2014).
21. T. Lin, C. Lin, H. Liu, J. Sheu, and W. Hung, *Chemical Communications* 47, 7 (2011).
22. J.O'M. Bockris, And M. Gamboa-Aldeco, *Modern Electrochemistry: Ionics*. Kluwer Academic/Plenum Publishers, New York: **1998**.
23. S. Wang, K. Qian, X. Bi, and W. Huang, *Journal of Physical Chemistry C* 113, 16 (2009).
24. J. C. Yannopoulos, *The Extractive Metallurgy of Gold* *The Extractive Metallurgy of Gold*. Van Nostrand Reinhold: New York, **1991**.
25. L. Depestel, and K. Strubbe, *Journal of Electroanalytical Chemistry* 572, 1 (2004).
26. A. Dolati, I. Imanieh, F. Salehi, and M. Farahani, *Materials Science and Engineering B-Advanced Functional Solid-State Materials* 176, 16 (2011).

27. J. Feng, A. Li, Z. Lei, and A. Wang, *Acs Applied Materials & Interfaces* 4, 5 (2012).
28. W. Ye, J. Yan, Q. Ye, and F. Zhou, *Journal of Physical Chemistry C* 114, 37 (2010).
29. J. Fransaer, and R. Penner, *Journal of Physical Chemistry B* 103, 36 (1999).
30. J. Love, L. Estroff, J. Kriebel, R. Nuzzo, and G. Whitesides, *Chemical Reviews* 105, 4 (2005).
31. M. Grzelczak, J. Perez-Juste, P. Mulvaney, and L. Liz-Marzan, *Chemical Society Reviews* 37, 9 (2008).
32. K. Uvdal, P. Bodo, and B. Liedberg, *Journal of Colloid and Interface Science* 149, 1 (1992).
33. A. Ulman, *Chemical Reviews* 96, 4 (1996).
34. G. Hager, and A. Brolo, *Journal of Electroanalytical Chemistry* 550, 291 (2003).
35. F. Gao, M. El-Deab, T. Okajima, and T. Ohsaka, *Journal of the Electrochemical Society* 152, 6 (2005).

CHAPTER 7. UTILIZATION OF INEXPENSIVE CARBON-BASED SUBSTRATES AS A PLATFORM FOR SENSING

Minh Tran¹, Alison Whale², Ahmad Fallatah¹, and Sonal Padalkar^{1,3*}

1. Department of Mechanical Engineering, Iowa State University, Ames, IA 50011, USA

2. Department of Materials Science and Engineering, Iowa State University, Ames, IA 50011, USA

3. Microelectronics Research Center, Iowa State University, Ames, IA 50011, USA

* Corresponding author Email: padalkar@iastate.edu

Abstract

Gold (Au) has been widely used as substrate material for Surface Enhanced Raman Spectroscopy (SERS) due to its stability, biocompatibility, and most importantly, its surface plasmon resonance property. Conventionally, Au has been deposited on a rigid substrate, such as glass or silicon, for SERS applications. That method, however, limits sample collection efficiency as well as portability. In this paper, we introduced carbon cloth and carbon paper as flexible substrates, coated with Au layer by electrodeposition. We showed that these flexible substrates were applicable for SERS by performing experiments with Rhodamine 6G (R6G) and paraoxon as probe molecules. Our results showed that an enhancement factor up to 8×10^3 was achieved using these substrates. Furthermore, we extended the use of these substrates to the detection of paraoxon on real fruit, which confirmed the sensitivity of our materials.

Introduction

Sensitive detection of low-concentration biological analytes and hazardous chemicals in the environment,^{1,2} anti-terrorism,^{3,4} biomedical diagnostics,⁵ forensic science,⁶ food² are important to prevent serious and costly human health problems as well as to provide public safety. Several analytical techniques have been utilized for the ultrasensitive detection of these analytes, some of which included high-performance liquid chromatography (HPLC) and GC/MS,² capillary electrochromatography (CE),⁷ enzyme cycling assays,⁸ photoluminescence,⁹ and ion mobility spectrometry.¹⁰ However, these techniques are time-consuming and require expensive equipment. They also require complicated sample pre-treatments, which may only be handled by trained personnel. On the other hand, surface enhanced Raman spectroscopy (SERS), a surface-sensitive Raman spectroscopy method, has become increasingly attractive as an alternative technique due to its combined advantages of simplicity, rapidity, and low-cost with excellent sensitivity. Since its discovery in 1974,¹¹ SERS has grown into an active area of research, including both experimental and theoretical works,¹² and evolving from fundamental understanding to promising applications.¹³

One type of SERS substrate was the use of colloidal metallic nanoparticles or their colloidal aggregates in solution.^{14,15} While the preparation of this type of substrate was simple, the colloidal particles or aggregates were not stable. SERS performance from these substrates was not reproducible and may not be suitable for non-aqueous applications.^{16,17} Another type of SERS substrate was made by the roughening of the substrate surface,¹⁸ by forming metallic nanoholes¹⁹, double-hole indentation structure with concentric rings,²⁰ nanogaps,²¹ nanoparticle arrays,²² nanodisk arrays²³ or by employing porous membrane,²⁴ latex microspheres,²⁵ polystyrene colloidal particles,²⁵ These SERS substrates, however, still possessed problems with non-reproducibility, complicated fabrication, or costly lithography

techniques. An alternative SERS substrate type was the use of a 2D substrate, on which metallic nanostructures were deposited. This type of substrate was easy to fabricate, and thus had potential for large-scale manufacturing. In addition, the performance of these SERS substrates was excellent, able to reach to the single-molecule detection.

The most popular 2D substrates for the third type of SERS materials mentioned above were rigid and smooth, including glass,²⁶⁻²⁸ silicon,^{29,30} and glass capillary,³¹ However, these SERS substrates were expensive and brittle, which made them inefficient when used for non-flat surfaces. To improve the usability of SERS substrates, a new wave of flexible substrate materials have been explored, including filter paper,^{16,17,32-37} adhesive tape,³⁸ cotton,^{4,39} carbon cloth,⁴⁰ polymer nanofibers,⁴¹ polymer nanotubes,⁴² and electrospun poly(vinyl alcohol) nanofibers.^{33,43} Regarding the fabrication techniques that were used to prepare flexible SERS substrates, some notable methods included ink-jet printing,^{32,37} dip coating,^{17,33} templating,¹⁶ drop casting,³⁸ and electroless deposition.^{36,40} Although some of these methods were simple, they required long preparation time or dry time (12 – 48 hours), large material use, and complicated requirements.

In this work, we fabricated flexible SERS substrates by electrodeposition of Au nanostructures onto carbon paper and carbon cloth. The resulting substrates were then used for SERS detection of R6G and paraoxon and achieved an enhancement factor of 10. Our fabrication of the SERS substrates was simple, inexpensive, and time-saving, which had potential to scale up. Furthermore, thick Au coating film conformed well to the substrate, making the substrate reliable and reproducible for SERS. A variety of characterization methods was employed to assist our investigation. Scanning electron microscopy was used to investigate the morphology of the Au coating and visual quality of the fabrication.

Information on the compositions of the deposits was obtained by energy dispersive x-ray spectroscopy. UV-Vis spectroscopy was used for determining optical property of the coating. Finally, SERS performance of the substrates was measured by Raman spectroscopy.

Experimental Details

The chemicals used for the electrodeposition of Au nanostructures were gold (III) chloride trihydrate ($\text{HAuCl}_4 \cdot 3\text{H}_2\text{O}$, $\geq 99.9\%$) and potassium hydroxide (KOH , $\geq 85.8\%$). These chemicals were purchased from Sigma Aldrich (St. Louis, MO, USA) and Fisher Scientific (Hanover park, IL, USA), respectively. The substrates used for electrodeposition of the Au nanostructures were carbon cloth (AvCarb Material Solutions, 1071 HCB) and wet-proofed carbon paper (Toray, 060) purchased from Fuel Cell Store (College Station, TX, USA). The chemicals used for cleaning the substrates were acetone, hydrochloric acid (HCl , 36.5-38.0%), and nitric acid (HNO_3 , 68.0-70.0%), purchased from Fisher Scientific. For SERS experiments, Rhodamine 6G dye (R6G, 99%) and paraoxon-ethyl ($\text{C}_{10}\text{H}_{14}\text{NO}_6\text{P}$, $\geq 90\%$) were purchased from Sigma Aldrich. All solutions were prepared using deionized (DI) water.

The electrodeposition was performed in an electrochemical cell of three electrodes (Figure 7.1a). For the electrodeposition of Au nanostructures, Ag/AgCl was used as the reference electrode (Figure 7.1b). A platinum wire (2 mm diameter) was used as counter electrode (Figure 7.1c). Carbon paper and carbon cloth were used as working electrodes (Figure 7.1d). The carbon paper substrate was cleaned prior to the deposition, using ultrasonic cleaner, in acetone bath for 10 minutes, followed by 2 minutes cleaning with hydrochloric acid and nitric acid (1 minute each). The carbon cloth was dipped in acetone for 1 h, then boiled in deionized water for 10 minutes, followed by cleaning in ultrasonic bath

using acetone for 10 minutes.⁴⁴ Both substrates were rinsed with deionized water after each cleaning step.

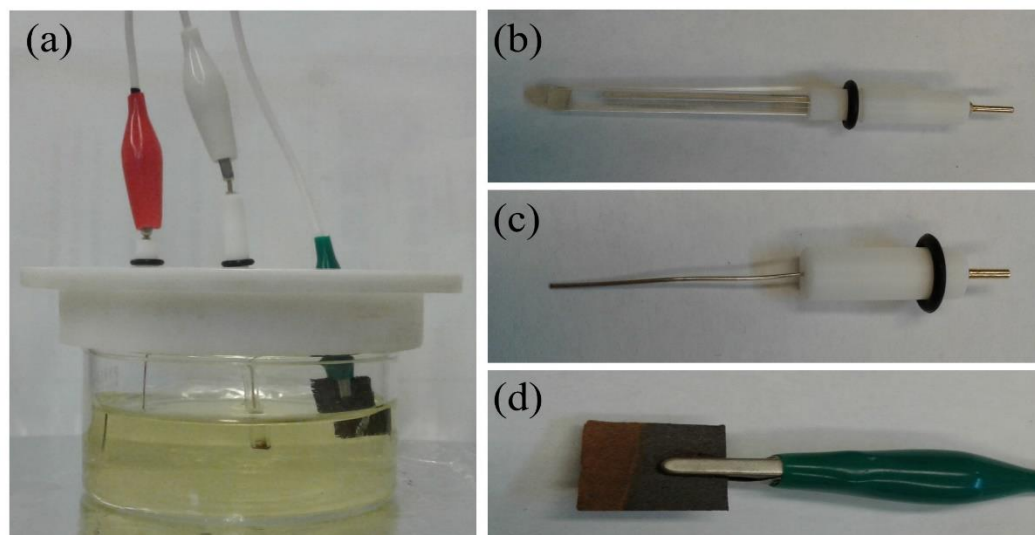


Figure 7.1 Photographs of the experimental setup (a), and individual electrodes, including reference (b), counter (c), and working (d) electrodes.

For the electrodeposition of Au nanostructures, the electrolyte solution was prepared by dissolving HAuCl_4 in deionized water to obtain a concentration of 3 mM. The pH of the electrolyte was adjusted to 3 using KOH. The electrodeposition was carried out at room temperature for 70 minutes and at an applied potential of -0.8 V.

To prepare the dye solution, 0.8 mg of R6G was dissolved in 5 mL of deionized water, and used as stock solution. Similarly, paraoxon stock solution was prepared by mixing 30 μL of oily concentrated paraoxon with 0.98 mL deionized water. To prepare sample for SERS experiments, a small volume of the stock solution was diluted to the desired concentration. Then, 300 μL of the diluted solution was drop cast onto the sample, and was left to dry under ambient condition. To improve wetting, prior to drop casting, the sample was treated with ambient air plasma for 1 minute under medium radio frequency power level (11 W) by a plasma cleaner (PDC-001, Harrick Plasma, Ithaca, NY).

The morphology of the nanostructures was studied by scanning electron microscopy (SEM) using a FEI Quanta-250 SEM instrument at 10 kV accelerating voltage. The SEM instrument was equipped with an Oxford Aztec energy dispersive x-ray (EDX) analysis system, which was used to conduct surface elemental analyses of the samples. SERS measurements were performed at room temperature on a Renishaw Dispersive Raman Spectrometer with Ar-ion laser running at 488 nm, using 50x objective lens, with incident power of 5 mW for 4 accumulations, each of which for 30 s. SERS spectra were collected from several random spots on each sample to confirm reproducibility.

Results and Discussions

Figure 7.2 shows digital photographs of the as-prepared carbon cloth and carbon paper electrodeposited with Au nanostructures. For each sample, a dark yellow layer

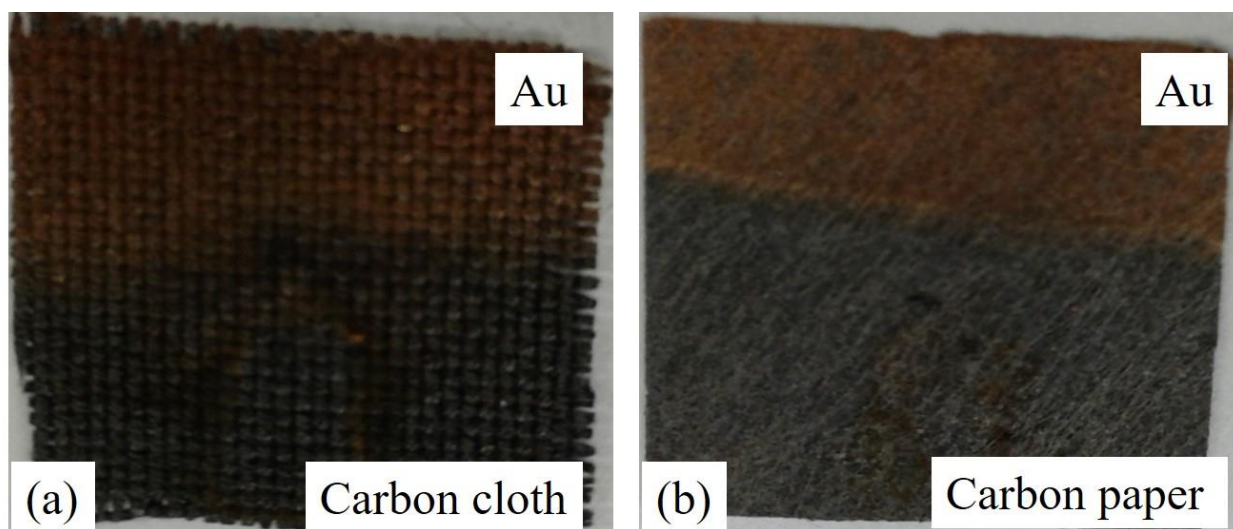


Figure 7.2 Photographs showing carbon cloth (a) and carbon paper (b) after electrodeposition with Au nanostructures.

completely covering the area of the substrate that was exposed to the electrolyte (Figure 7.1a), as compared with the black plain substrate, indicated that Au had been successfully deposited onto the substrate. The electrodeposition conditions followed by this paper were

reported elsewhere by our group.⁴⁵ As shown in both Figure 7.3 and Figure 7.4, a compact layer of Au nanostructures was observed, completely covering the surface of the fiber. The

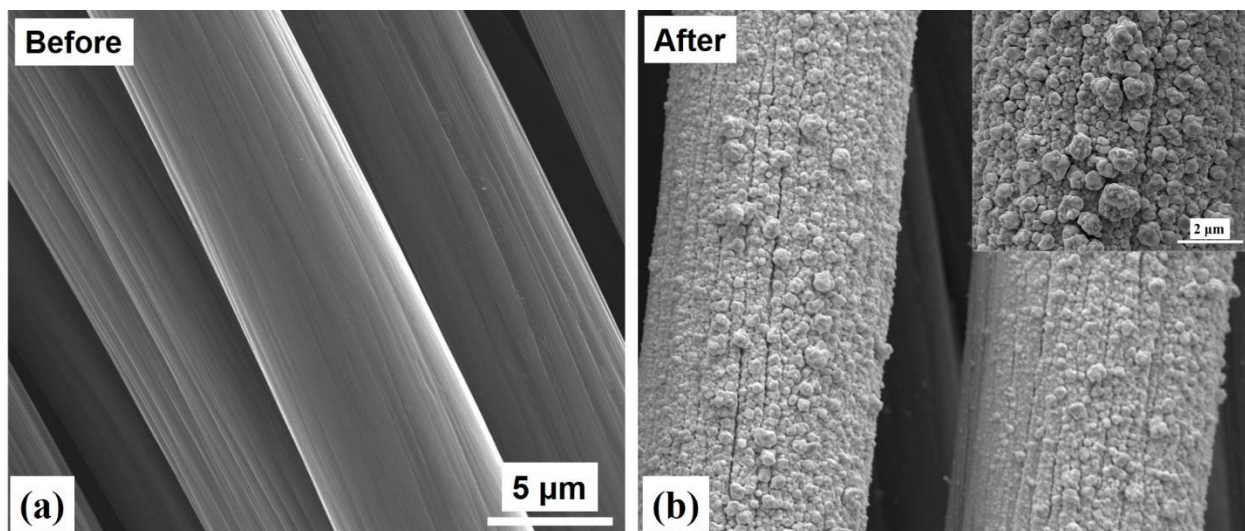


Figure 7.3 SEM images of carbon cloth (a) before and (b) after electrodeposition of Au nanostructures. The inset shows Au-electrodeposited carbon cloth at higher magnification.

surface of the layer was rough as a result of the coalescence of Au nanostructures. Above this compact layer, a sub-monolayer of Au nanostructures was observed. Also, Au nanostructures of the overlay were larger than those underneath (insets of Figure 7.3b and Figure 7.4b). We

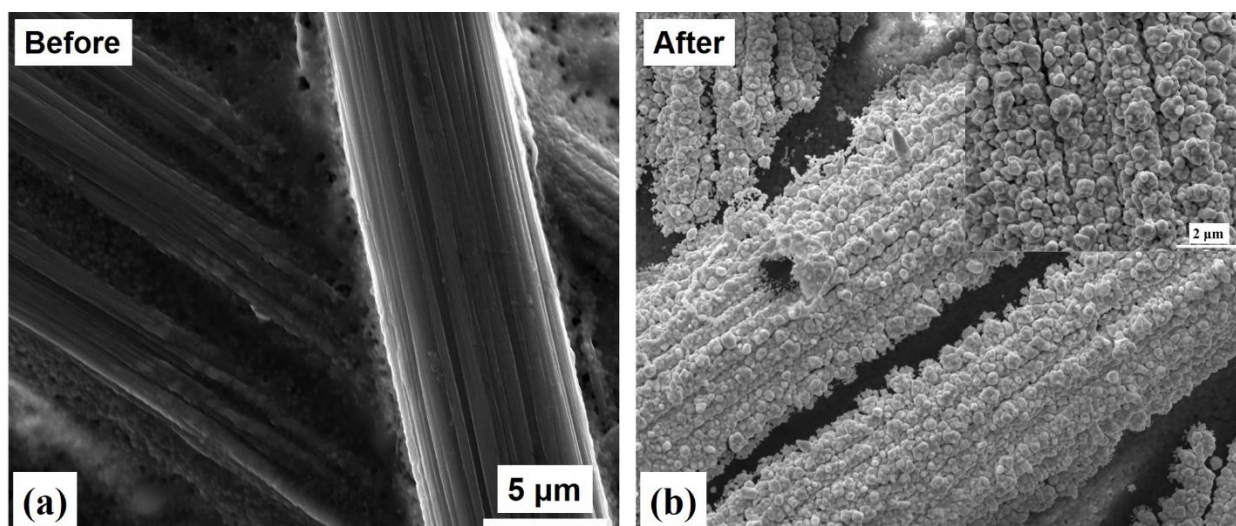


Figure 7.4 SEM images of carbon paper (a) before and (b) after electrodeposition of Au nanostructures. The inset shows Au-electrodeposited carbon paper at higher magnification.

speculated that the overgrown occurred when the reduction rate decreased. Under this condition, the new Au atoms would preferably adsorb on existing Au nanostructures rather than forming new nuclei. As a result, the overgrown Au nanostructures grew faster and became very large. We estimated, by taking the differences in diameters of the fibers before and after electrodeposition in several SEM images, that the thicknesses of the Au coatings on carbon cloth and carbon paper were $\sim 1 - \sim 1.3 \mu\text{m}$ and $\sim 0.2 - 0.3 \mu\text{m}$, respectively. Chemical compositions of the as-synthesized samples were determined by EDX (Figure 7.5). Au were

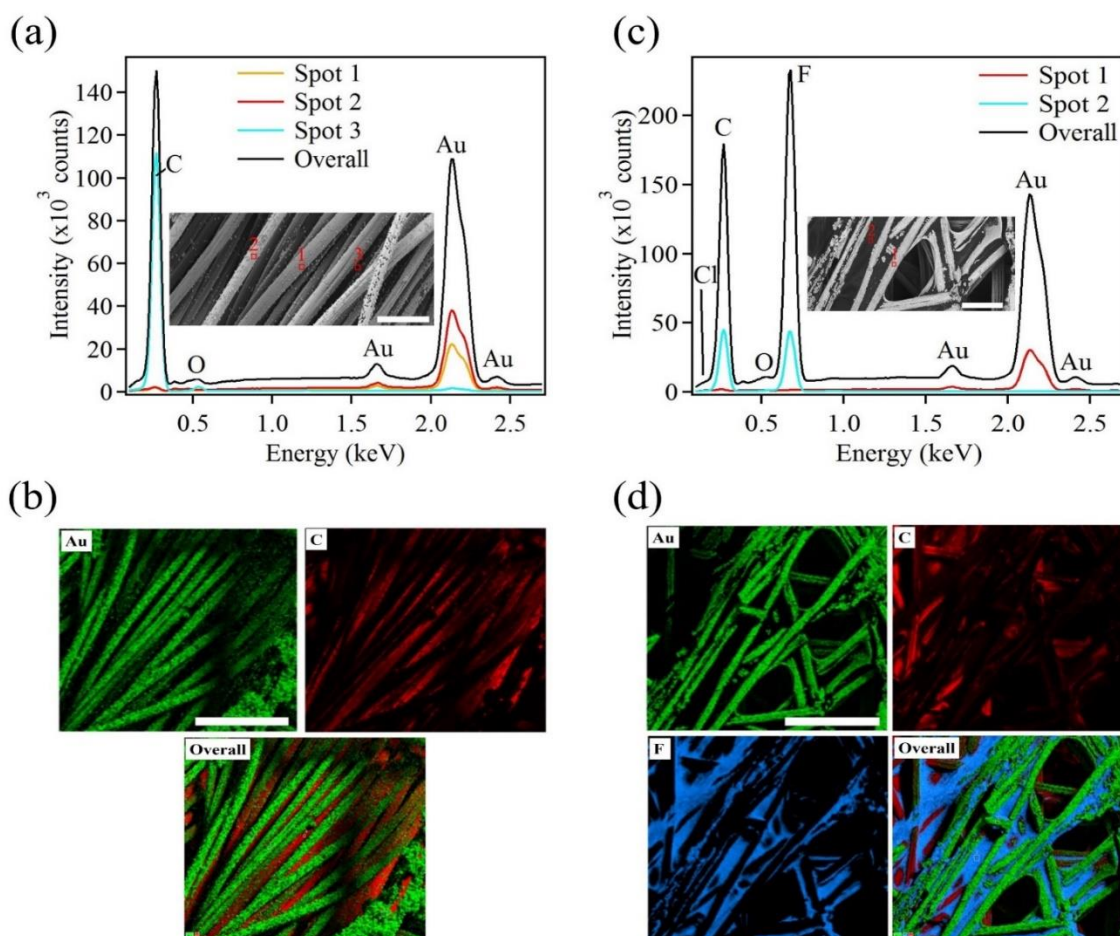


Figure 7.5 EDX patterns and mapping analysis of Au nanostructures electrodeposited on (a,b) carbon cloth, and (c,d) carbon paper, respectively. The insets show the different spots where EDX patterns were taken. The scale bars on the insets and the EDX mapping are 550 μm and 100 μm , respectively.

the only metal peaks observed, indicating the purity of the samples obtained. The EDX also indicated that while the fibers near the surface was completely covered by Au, the fibers underneath appeared to be uncoated or showed much less coating (see different spots shown in Figure 7.5a and c). Future effort would be devoted to obtain a more complete coating. A very strong C peak was observed, obviously from the fiber substrate. O and Cl peaks could be the results of the slight oxidation of the surface and the ligand left over from HAuCl_4 precursor, respectively while F peak could be from the adhesive resin.⁴⁴ Table 7.1 shows mass fraction analyses of the chemical elements obtained by EDX.

Table 7.1 *Mass fraction analysis of chemical elements obtained by EDX*

Element	C	O	F	Cl	Au	Total
Au/carbon cloth	2.86	0.20	N/A	0.03	96.91	100.00
Au/carbon paper	2.56	0.37	0.37	0.07	96.62	100.00

Figure 7.6 shows UV-Vis spectra of Au electrodeposited on carbon cloth and carbon paper. Both spectra show characteristic peaks of Au. These peaks red-shifted beyond 550 nm, indicating that the sizes of Au nanostructures were large. In addition, the peak widths were also large, indicating that Au nanostructures had large size distributions.⁴⁶ Thus, the plasmon resonance absorption characterization agreed well with Au nanostructures observed in the SEM images.

To evaluate our samples for SERS application, we first chose Rhodamine 6G (R6G) as probe molecule. R6G has been widely used for SERS by many researchers due to their well-defined vibrational features. Figure 7.7a shows Raman spectra of 10^{-5} M R6G dye upon drop casting onto Au-electrodeposited carbon cloth and carbon paper. For comparison, the

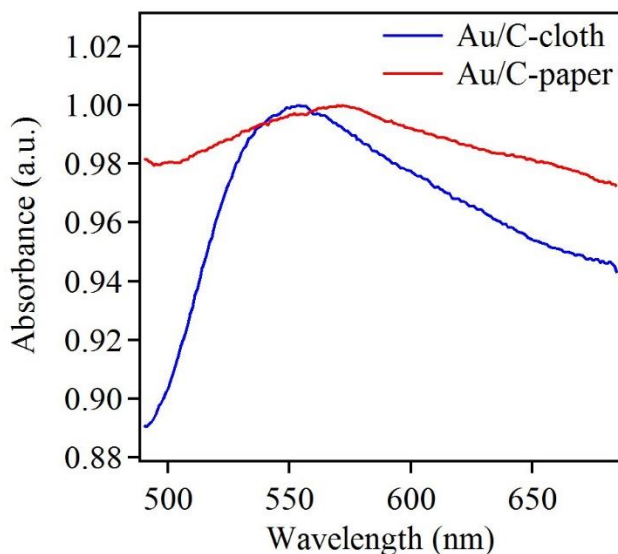


Figure 7.6 *Normalized UV-Vis spectra of Au electrodeposited carbon cloth and carbon paper*

same amount of R6G was also drop cast onto carbon cloth and paper without Au deposition. No noticeable Raman signal was detected using these blank substrates. On the other hand, several strong Raman peaks were observed when Au was electrodeposited on carbon paper. All these peaks were also observed with carbon cloth but their intensities were weaker even at higher R6G concentration. In the next set of SERS experiments, paraoxon was used as probe molecule. Paraoxon is an organophosphorous compound and one of the most hazardous pesticides. Thus, only a trace amount of this compound in the environment can cause serious health problem.² Figure 7.7b shows Raman spectra of 10^{-2} M paraoxon adsorbing on Au-electrodeposited carbon cloth and paper substrates. Several fingerprint peaks representing different vibrational modes of paraoxon molecules were clearly seen in these spectra.⁴⁷ Raman scattering was certainly enhanced by the Au nanostructures because no Raman peak of R6G dye and much weaker peaks of paraoxon were observed when blank carbon cloth and paper were used as SERS substrates. Also, it is noteworthy that for both probe molecules, Raman signals were obtained with much higher intensities for carbon paper

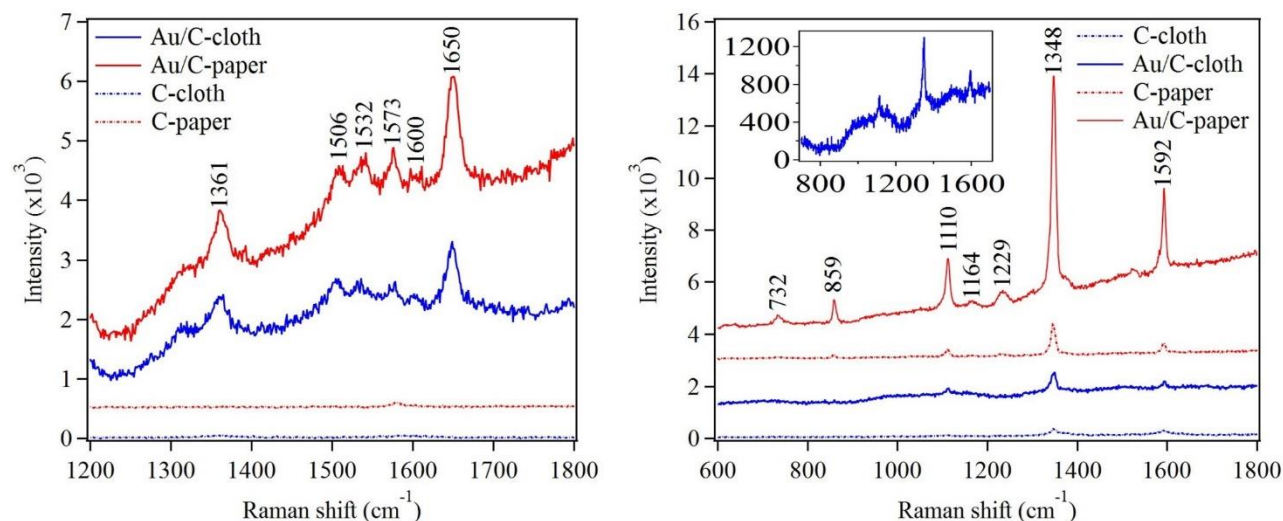


Figure 7.7 Raman spectra of (a) 10^{-5} M and 10^{-6} M R6G, and (b) 10^{-2} M paraoxon adsorbed on Au nanostructures electrodeposited on carbon cloth and carbon paper, respectively. Raman spectra of R6G and paraoxon adsorbed on blank carbon cloth and paper without Au coating are shown for comparison. The inset shows a close-up view for carbon cloth.

than for carbon cloth. Table 7.2 provides detailed assignment for all the peaks in Figure 7.6 according to published data.

One way to quantitatively determine the effectiveness of SERS substrate is to calculate the enhancement factor (EF). The most widely used definition of the EF is described as

$$EF = \frac{I_{SERS}/c_{SERS}}{I_{RS}/c_{RS}}$$

where I_{SERS} and I_{RS} are Raman intensities of SERS and non-SERS substrates, respectively, while c_{SERS} and c_{RS} are analyte concentrations used for SERS and non-SERS substrates, respectively.⁵³ In our case, we used the same analyte concentrations for both substrates.

Thus, EF was simply a ratio of I_{SERS} and I_{RS} . For paraoxon, the EF values were ~ 14 and $\sim 8 \times 10^3$ times. For R6G, since Raman signals obtained from blank substrates (I_{RS}) were too weak to be detected by our instrument, it was not possible to obtain absolute values for EF. Instead,

Table 7.2 Raman peak assignments for R6G dye and paraoxon pesticide corresponding to Figure 7.7

Raman peak (cm ⁻¹)	Assignment for R6G	Reference
1361	Aromatic C-C stretching, in-plane C-H bending	48-51
1506	Aromatic C-C stretching, C-N stretching, C-H bending, N-H bending	48-50
1532		50
1573	Aromatic C-C stretching, in-plane N-H bending	48-50
1600		48-50
1650	Aromatic C-C stretching, in-plane C-H bending	48-51
Raman peak (cm ⁻¹)	Assignment for paraoxon	Reference
732	NO ₂ scissor, C-C bending	3,52
859	NO ₂ scissor (Aromatic-NO ₂)	3,52
1110	C-H band (in plane)/NO ₂ asymmetric stretching	3,52
1348	Symmetry stretching NO ₂	3,52
1592	Phenyl ring vibration	3,52

we only roughly estimated EFs in a manner similar to those reported by Yamamoto et al.⁴⁹

Thus, EF values for R6G adsorbed on Au-electrodeposited carbon cloth and paper were 0.9×10^3 (for 10^{-5} M R6G) and 1.5×10^3 (for 10^{-5} M R6G), respectively. Currently, there are two proposed mechanisms that may explain the Raman scattering enhancement observed above. One is the chemical enhancement mechanism that occurred when charges were transferred between the adsorbed probe molecules and the Au substrates. However, chemical enhancement only accounted for a tiny portion of the total enhancement effect. The rest was

contributed by local electromagnetic enhancement.^{54,55} It has been well known that roughened metallic surface resulted in enhanced Raman signal, compared with polished surface.¹⁸ Thus, we believed that rough Au surface upon electrodeposition, whose numerous crevices concentrated light, was the major factor leading to SERS observed in both substrates. In addition, the high surface area resulted from rough surface would adsorb more probe molecules, thus increasing efficiency as well as causing SERS.

In the last set of experiments, we extended the application of Au electrodeposited carbon cloth and paper to SERS detection of paraoxon on real fruit. Specifically, 10^{-1} M paraoxon was dropped onto a small area on the skin of an apple. After leaving the area to dry in air, we wet the SERS substrate by immersing it in deionized water. Then, we wiped the paraoxon-infected area on the apple with the wet substrate five times (Figure 7.8). We also used the substrates to wipe non-infected area for comparison. The results are shown in Figure 7.9. Clearly, our substrates were sensitive enough to detect the presence of paraoxon on real fruit, thus indicating their potential as quick and economical substrates for real-life applications.



Figure 7.8 *Wiping the contaminated area on an apple's skin by carbon cloth electrodeposited with Au for SERS detection of paraoxon*

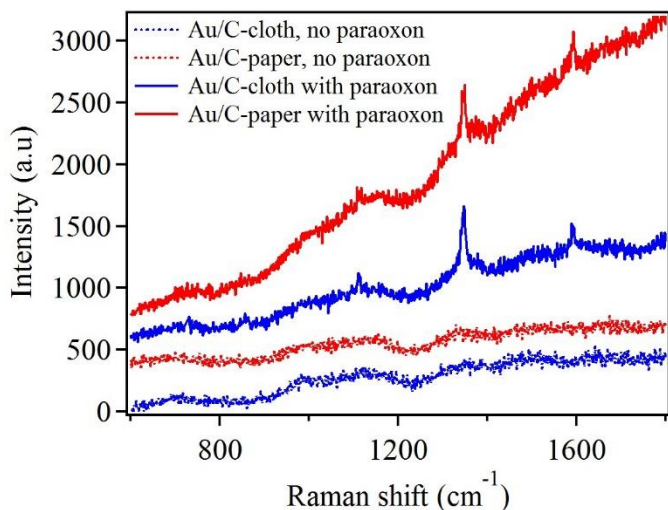


Figure 7.9 *SERS detection of paraoxon on apple using carbon cloth and paper electrodeposited with Au as substrates. The results show that the substrates were sensitive to the presence of paraoxon.*

Conclusion

In summary, we report the use of carbon cloth and carbon paper as flexible materials for SERS applications. Au was chosen as the metallic substrate due to its stability, biocompatibility, and surface plasmon resonance property, known to enhance Raman signal. We prepared SERS substrates by coating carbon cloth and carbon paper with Au by electrodeposition. A variety of characterization methods, including SEM, EDX, and UV-Vis, had been employed to confirm the successful deposition of Au. Then, the substrates were used to detect R6G and paraoxon and achieved an enhancement factor up to 8×10^3 . We believed that the rough Au surface, whose crevices concentrated light, after electrodeposition would be the reason for the enhancement of Raman signal. We further investigated the performance of our substrates for real fruit, and the results confirmed the sensitivity of our materials.

References

1. Halvorson, R.; Vikesland, P. *Environmental Science & Technology* **2010**, *44* (20), 7749-7755.
2. Aragay, G.; Pino, F.; Merkoci, A. *Chemical Reviews* **2012**, *112* (10), 5317-5338.
3. Zhang, C.; Wang, K.; Han, D.; Pang, Q. *Spectrochimica Acta Part a-Molecular and Biomolecular Spectroscopy* **2014**, *122*, 387-391.
4. Gong, Z.; Du, H.; Cheng, F.; Wang, C.; Wang, C.; Fan, M. *Acs Applied Materials & Interfaces* **2014**, *6* (24), 21931-21937.
5. Tripp, R.; Dluhy, R.; Zhao, Y. *Nano Today* **2008**, *3* (3-4), 31-37.
6. Muehlethaler, C.; Leona, M.; Lombardi, J. *Analytical Chemistry* **2016**, *88* (1), 152-169.
7. Xie, W.; Xu, A.; Yeung, E. *Analytical Chemistry* **2009**, *81* (3), 1280-1284.
8. Reisch, A.; Elpeleg, O.; Pon, L.; Schon, E. *Mitochondria, 2nd Edition* **2007**, *80*, 199-222.

9. Patra, D.; Mishra, A. *Sensors and Actuators B-Chemical* **2001**, *80* (3), 278-282.
10. Hill, H.; Simpson, G. *Field Analytical Chemistry and Technology* **1997**, *1* (3), 119-134.
11. Fleischmann, M.; Hendra, P.; Mcquillan, A. *Chemical Physics Letters* **1974**, *26* (2), 163-166.
12. Lin, X.; Cui, Y.; Xu, Y.; Ren, B.; Tian, Z. *Analytical and Bioanalytical Chemistry* **2009**, *394* (7), 1729-1745.
13. Fan, M.; Andrade, G.; Brolo, A. *Analytica Chimica Acta* **2011**, *693* (1-2), 7-25.
14. Cao, Y.; Jin, R.; Mirkin, C. *Science* **2002**, *297* (5586), 1536-1540.
15. Kneipp, K.; Haka, A.; Kneipp, H.; Badizadegan, K.; Yoshizawa, N.; Boone, C.; Shafer-Peltier, K.; Motz, J.; Dasari, R.; Feld, M. *Applied Spectroscopy* **2002**, *56* (2), 150-154.
16. Villa, J.; dos Santos, D.; Poppi, R. *Microchimica Acta* **2016**, *183* (10), 2745-2752.

17. Lee, C.; Hankus, M.; Tian, L.; Pellegrino, P.; Singamaneni, S. *Analytical Chemistry* **2011**, *83* (23), 8953-8958.
18. Cai, W.; Ren, B.; Li, X.; She, C.; Liu, F.; Cai, X.; Tian, Z. *Surface Science* **1998**, *406* (1-3), 9-22.
19. Brolo, A.; Arctander, E.; Gordon, R.; Leathem, B.; Kavanagh, K. *Nano Letters* **2004**, *4* (10), 2015-2018.
20. Min, Q.; Santos, M.; Girotto, E.; Brolo, A.; Gordon, R. *Journal of Physical Chemistry C* **2008**, *112* (39), 15098-15101.
21. Im, H.; Bantz, K.; Lindquist, N.; Haynes, C.; Oh, S. *Nano Letters* **2010**, *10* (6), 2231-2236.
22. McFarland, A.; Young, M.; Dieringer, J.; Van Duyne, R. *Journal of Physical Chemistry B* **2005**, *109* (22), 11279-11285.
23. Abu Hatab, N.; Oran, J.; Sepaniak, M. *Acs Nano* **2008**, *2* (2), 377-385.
24. Ko, H.; Chang, S.; Tsukruk, V. *Acs Nano* **2009**, *3* (1), 181-188.

25. Tessier, P.; Velev, O.; Kalambur, A.; Lenhoff, A.; Rabolt, J.; Kaler, E. *Advanced Materials* **2001**, *13* (6), 396-400.
26. Jiang, X.; Qin, X.; Yin, D.; Gong, M.; Yang, L.; Zhao, B.; Ruan, W. *Spectrochimica Acta Part a-Molecular and Biomolecular Spectroscopy* **2015**, *140*, 474-478.
27. Li, Y.; Lu, G.; Wu, X.; Shi, G. *Journal of Physical Chemistry B* **2006**, *110* (48), 24585-24592.
28. Kannan, P.; Dolinska, J.; Maiyalagan, T.; Opallo, M. *Nanoscale* **2014**, *6* (19), 11169-11176.
29. Li, H.; Chong, X.; Chen, Y.; Yang, L.; Luo, L.; Zhao, B.; Tian, Y. *Colloids and Surfaces a-Physicochemical and Engineering Aspects* **2016**, *493*, 52-58.
30. Ye, W.; Liu, J.; Liu, Q.; Zhou, F.; Liu, W. *Electrochimica Acta* **2010**, *55* (28), 8649-8654.
31. Liu, J.; Wang, J.; Huang, W.; Yu, L.; Ren, X.; Wen, W.; Yu, S. *Scientific Reports* **2012**, *2*.
32. Yu, W.; White, I. *Analyst* **2013**, *138* (4), 1020-1025.

33. Lee, C.; Tian, L.; Singamaneni, S. *Acs Applied Materials & Interfaces* **2010**, *2* (12), 3429-3435.
34. Wei, W.; Huang, Q. *Spectrochimica Acta Part a-Molecular and Biomolecular Spectroscopy* **2017**, *179*, 211-215.
35. Ngo, Y.; Li, D.; Simon, G.; Garnier, G. *Langmuir* **2012**, *28* (23), 8782-8790.
36. Zhu, Y.; Li, M.; Yu, D.; Yang, L. *Talanta* **2014**, *128*, 117-124.
37. Yu, W.; White, I. *Analytical Chemistry* **2010**, *82* (23), 9626-9630.
38. Chen, J.; Huang, Y.; Kannan, P.; Zhang, L.; Lin, Z.; Zhang, J.; Chen, T.; Guo, L. *Analytical Chemistry* **2016**, *88* (4), 2149-2155.
39. Qu, L.; Geng, Y.; Bao, Z.; Riaz, S.; Li, H. *Microchimica Acta* **2016**, *183* (4), 1307-1313.
40. Zhao, W.; Xu, Z.; Sun, T.; Liu, S.; Wu, X.; Ma, Z.; He, J.; Chen, C. *Journal of Alloys and Compounds* **2014**, *584*, 635-639.
41. Wang, P.; Zhang, L.; Xia, Y.; Tong, L.; Xu, X.; Ying, Y. *Nano Letters* **2012**, *12* (6), 3145-3150.

42. Huang, L.; Zhou, Y.; Han, S.; Yan, Y.; Zhou, L.; Chen, W.; Zhou, P.; Chen, X.; Roy, V. *Small* **2014**, *10* (22), 4645-4650.
43. He, D.; Hu, B.; Yao, Q.; Wang, K.; Yu, S. *Acs Nano* **2009**, *3* (12), 3993-4002.
44. Zhang, Z.; Su, F.; Wang, K.; Jiang, W.; Men, X.; Liu, W. *Materials Science and Engineering a-Structural Materials Properties Microstructure and Processing* **2005**, *404* (1-2), 251-258.
45. Tran, M.; Mundt, C.; Lan, T.; Padalkar, S. *J. Nanosci. Nanotechnol.* **2018**, *18*, 3492-3498.
46. Tran, M.; DePenning, R.; Turner, M.; Padalkar, S. *Mater. Res. Express* **2016**, *3* (10).
47. Wang, B.; Zhang, L.; Zhou, X. *Spectrochimica Acta Part a-Molecular and Biomolecular Spectroscopy* **2014**, *121*, 63-69.
48. He, X.; Gao, Y.; Mahjouri-Samani, M.; Black, P.; Allen, J.; Mitchell, M.; Xiong, W.; Zhou, Y.; Jiang, L.; Lu, Y. *Nanotechnology* **2012**, *23* (20).

49. Yamamoto, Y.; Hasegawa, K.; Hasegawa, Y.; Takahashi, N.; Kitahama, Y.; Fukuoka, S.; Murase, N.; Baba, Y.; Ozaki, Y.; Itoh, T. *Physical Chemistry Chemical Physics* **2013**, *15* (35), 14611-14615.
50. Hildebrandt, P.; Stockburger, M. *Journal of Physical Chemistry* **1984**, *88* (24), 5935-5944.
51. Zhang, Y.; Zheng, J.; Gao, G.; Kong, Y.; Zhi, X.; Wang, K.; Zhang, X.; Cui, D. *International Journal of Nanomedicine* **2011**, *6*, 2899-2906.
52. Fathi, F.; Lagugne-Labarthe, F.; Pedersen, D.; Kraatz, H. *Analyst* **2012**, *137* (19), 4448-4453.
53. Le Ru, E.; Blackie, E.; Meyer, M.; Etchegoin, P. *Journal of Physical Chemistry C* **2007**, *111* (37), 13794-13803.
54. Sharma, B.; Frontiera, R.; Henry, A.; Ringe, E.; Van Duyne, R. *Materials Today* **2012**, *15* (1-2), 16-25.
55. Doering, W.; Nie, S. *Journal of Physical Chemistry B* **2002**, *106* (2), 311-317.

CHAPTER 8. CONCLUSION

In conclusion, this work has shown that various metallic nanostructures, including Au, Cu, Pt, Pd, Ni, and Co, have been successfully synthesized by the modified galvanic displacement method, electrodeposition, and as colloidal suspension by citrate reduction. A range of characterization methods have been employed to investigate the composition, nanostructure, morphology, size, and density of the materials. In the synthesis of Au nanoparticles by citrate reduction (Turkevich's method), we were able to evaluate the effects of temperature and $\text{Na}_3\text{Ct}/\text{HAuCl}_4$ ratio on the morphology and size of the resulting Au nanoparticles. While different temperatures only slightly changed those nanostructural characteristics, the $\text{Na}_3\text{Ct}/\text{HAuCl}_4$ ratio appeared to dictate the outcome of Au nanoparticles, in which monodisperse, small, and spherical particles were observed with high ratios whereas polydisperse, large and elongated particles were observed with low ratios. In the modified galvanic displacement method, we overcame the lack of control in size, shape, and density of the deposited metallic nanostructures in the conventional method by drastically reducing HF exposure of the Si substrate, by utilizing additives such as L-cysteine, CTAB, and SDS, and by using cyclic deposition technique. The modified galvanic displacement method proved to be universal as indicated by successful deposition of different metals and transition metals on Si substrate. In addition, the results obtained by the modified method were reproducible. The limited use of HF also made waste treatment manageable and reduced environmental risks. In the electrodeposition method, we showed that both the applied potential and the electrolyte pH had direct influence on the size and density of Au nanostructures. On the other hand, the presence of L-cysteine as additive gave Au nanostructures increasingly dendritic morphologies. The electrodeposition method was also carried out to fabricate flexible SERS

substrates made up of Au-coated carbon cloth and carbon paper. The synthesized materials were then tested for their performance in SERS and photoelectrochemical hydrogen production. SERS substrates from the materials synthesized by our methods were equally effective in detecting trace analytes as other reported SERS substrates as shown in my work for detecting R6G and paraoxon. Additionally, transition metal nanostructures like Pt and Pd have also shown promise as SERS substrates. Regarding photoelectrochemical hydrogen production, we showed that Au nanostructures grown by electrodeposition on ITO can increase the performance of Cu₂O photocathode by 81% when they were used as an underlayer.¹ Low-cost and abundant catalysts like Ni and Co deposited on Si substrate by our modified galvanic displacement also showed enhanced performance toward hydrogen production, which will be presented in an upcoming publication.

References

1. Lan, T.; Mundt, C.; Tran, M.; Padalkar, S. *Journal of Materials Research* 2017, 32 (9), 1656-1664.